DISCOVERING THE ELECTRONIC PROPERTIES OF METAL HYDRIDES, METAL OXIDES AND ORGANIC MOLECULES USING ANION PHOTOELECTRON SPECTROSCOPY

by
Allyson M. Buytendyk

A dissertation submitted to Johns Hopkins University in conformity with the requirements for the degree of Doctor of Philosophy

Baltimore, Maryland

September, 2015

ABSTRACT

Negatively charged molecular ions were studied in the gas phase using anion photoelectron spectroscopy. By coupling theory with the experimentally measured electronic structure, the geometries of the neutral and anion complexes could be predicted. The experiments were conducted using a one-of-a-kind time-of-flight mass spectrometer coupled with a pulsed negative ion photoelectron spectrometer. The molecules studied include metal oxides, metal hydrides, aromatic heterocylic organic compounds, and proton-coupled organic acids.

Metal oxides serve as catalysts in reactions from many scientific fields and understanding the catalysis process at the molecular level could help improve reaction efficiencies (**Chapter 1**). The experimental investigation of the super-alkali anions, Li_3O^- and Na_3O^-, revealed both photodetachment and photoionization occur due to the low ionization potential of both neutral molecules. Additionally, HfO^- and ZrO^- were studied, and although both Hf and Zr have very similar atomic properties, their oxides differ greatly where ZrO^- has a much lower electron affinity than HfO^-.

In the pursuit of using hydrogen as an environmentally friendly fuel alternative, a practical method for storing hydrogen is necessary and metal hydrides are thought to be the answer (**Chapter 2**). Studies yielding structural and electronic information about the hydrogen bonding/interacting in the complex, such as in MgH^- and AlH_4^-, are vital to constructing a practical hydrogen storage device.

Chapter 3 presents the negative ion photoelectron spectra of aromatic heterocylic organic compounds, tetraphenylporphine$^-$ anions, with the metal center (Fe, Ni, or Mn), and the stable closed-shell quinoline$^-$ anion. Both of these systems can be viewed as components of metal-organic-frameworks (MOFs), which are used to sequester greenhouse gases such as CO_2.

By measuring the hydrogen bond strength between proton-coupled bicarboxylates and other molecules found in the enzyme-substrate complex in the gas phase, provides an upper limit for the forces available to the enzyme (**Chapter 4**). The intermolecular hydrogen bond strength for formate-formic acid, acetate-acetic acid, imidazolide-imidazole, and phenolate-phenol were experimentally determined to be quite strong (1.0-1.4 eV).

Advisor:	Dr. Kit Bowen
Readers:	Dr. Mark Pederson
	Dr. John Toscano

ACKNOWLEDGMENTS

I would like to first, and foremost, thank my advisor Dr. Kit Bowen, for giving me the opportunity to work in his lab over the last 6 years. I have grown in so many ways and acquired a vast amount of knowledge about chemical physics, as well as on how to become a critically thinking scientist which, I will be forever grateful for.

The Bowen Lab is a pretty unique cast of characters but I wouldn't trade working with each one of them, past and present, for anything.

Thank you Jacob Graham for being a fantastic lab partner. We encountered countless problems and challenges yet, made numerous achievements. Although we each have our own ways of approaching a task, we made a pretty good team. I wish you all the best in your post-doc and in everything your scientific career holds.

It has been exciting to see both Gaoxiang Liu and Sandy Ciborowski take over and excel at running the instrument. I have no doubt that great success will come to them both. Go Team PSA!

Evan is an unstoppable force and there isn't an obstacle in lab he can't overcome. He is the hardest working person I know and his 'can do' attitude will take him far. Thank you for your friendship and unquestionable enthusiasm to help, in any situation, both in- and outside of lab.

I appreciate Xinxing Zhang's willingness to provide data and advice on pulsed-instruments and sources to Team PSA. Xin Tang has a remarkable knack for ingenuity that never ceases to amaze me and is an undeniable asset to the lab. Yi Wang is one of the nicest and understanding people I’ve met and always enjoyable to work beside. I respect Zachary Hicks’ appreciation for good scientific conversations and coffee, two very important aspects of graduate school. I hope our newest lab member Nic Blando embraces the Bowen Lab to the fullest and achieves many scientific discoveries. I have immensely enjoyed working, albeit a short time, with Sara Marquez. Her determination is remarkable and I have no doubt she will be very successful in the group.

Our lab has had an influx of flourishing talent, from my high school mentee, Theresa Hwang, to undergraduates including Alane Lim and Ryan Wood. I would like to thank them all for their help and efforts.

To my predecessors: Dr. Di Wang, thank you for your patience in teaching me the ropes, as well as passing along your meticulous attention to detail. I have to thank Dr. Yeon Jae Ko for reminding me to always be true to myself and never be afraid of taking a fashion risk. Thank you Dr. Jing Chen for showing me there’s no reason not to approach every obstacle with a smile. And, Dr. Angela Buonaugurio, thank you for encouraging me to join the Bowen group. Little did I know 6 years ago, I would find lifelong friend and be adopted into a wonderful home-away-from home.

Lastly, I will be forever grateful for the love and support from my parents. You have unconditionally encouraged me in every step in my educational journey which means everything to me. Thank you Mom and Dad!

TABLE OF CONTENTS

LIST OF TABLES

LIST OF FIGURES

Chapter I: Introduction

Anion photoelectron spectroscopy (PES) is conducted by crossing a mass-selected ion beam with a fixed frequency laser and energy analyzing the resultant photodetached electrons. Photodetachment is governed by the following energy conservation relationship

$$h\nu = EBE + EKE \tag{1}$$

where hν is the photon energy, EBE is the electron binding energy, and EKE is the measured electron kinetic energy. The resulting EBE spectrum, from the subtraction of the experimentally measured EKE from the photon energy, provides anion-to-neutral transition energies corresponding to occupied levels in the negative ion to an energetically accessible level in the resultant neutral. Applying this technique to small negative ion molecules or clusters provides insightful information pertaining to both the ion and the neutral, such as vibrational frequencies, geometrical structure, and the electron affinity of the neutral.

Pulsed negative ion photoelectron spectroscopy is one method employed in the Bowen lab in which the light source is a pulsed laser. The instrument used to conduct these experiments is a one-of-a-kind, home built, apparatus comprised of three main components: 1) the ion source, producing the cluster or molecular anion 2) a time-of-mass spectrometer, used to mass select a specific anion of interest, and 3) a photoelectron spectrometer, to energy analyzing the resulting photodetached electrons. A schematic overview of the instrument is shown in Figure I.1.

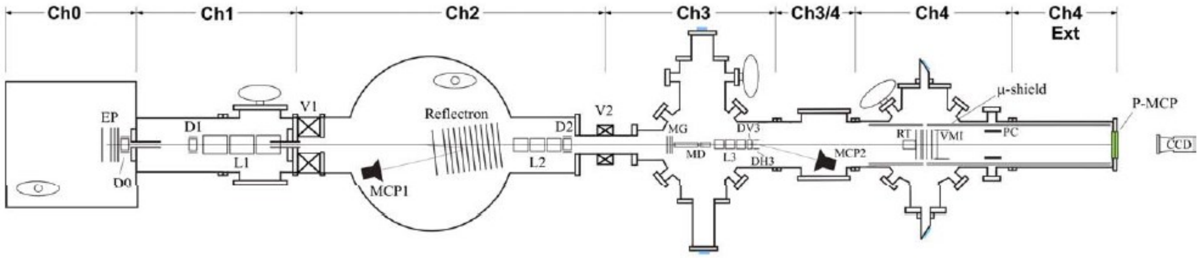

Figure I.1: Schematic diagram of the pulsed photoelectron spectrometer.

(**EP**– Wiley-McLaren type Extraction Plates, **D** – Deflector Sets (**H** –horizontal, **V** – vertical), **L** – Lens, **V** – Valve, **MCP** – Microchannel Plate Detector, **MG** – Mass Gate, **MD** – Momentum Decelerator, **RT**– Rereferencing Tube, **VMI** – Velocity Map Imaging Stack, **PC** – Pulsed Collar, **P-MCP** – imaging MCP with phosphor screen, **CCD** – camera.)[1]

I.1. ION SOURCES

Ion sources allow a particular cluster or molecular system of interest to be created in the gas phase. The first stage in planning any experiment is deciding the best method for synthesizing a particular species in the gas phase because each source is optimized to generate a specific type of system. The most routine source for producing molecular anions is a laser photoemission/vaporization rod source and for producing metal cluster anions is the pulsed arc cluster ionization source (PACIS). Each of these is described in more detail in this section.

I.1.1. Laser Photoemission/Vaporization Source

Negative ions are generated by entraining the vapor of a molecule of interest in helium (typically, between 15-150 psia) and pulsed from a general purpose valve (at 10 Hz). A liquid sample can be placed directly in the pulsed value, while a solid sample can be heated in a small oven attached to the front of the valve. Helium (containing the vapor of the neutral molecule) is supersonically expanded over a metal rod (Cu, 0.25 inches), that is simultaneously rotating and translating, where a pulsed Nd:YAG laser (532 nm photons, 10 Hz) is properly timed to strike the metal, creating electrons, from photoemission. Negative ions are formed by electron attachment, from the collisions in the helium jet expansion, between the electrons produced from photoemission and the neutral molecules (Figure I.2).

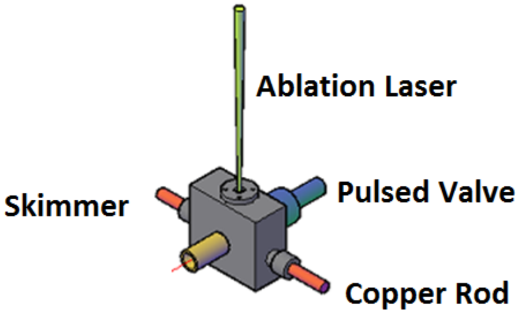

Figure I.2: Schematic diagram of the photoemission/laser ablation source

I.1.2. Pulsed Arc Cluster Ionization Source (PACIS)

Metallic clusters and metal hydrides are created when ~30 μs long 100 V pulse initiates a discharge between a copper anode and the grounded, metallic sample cathode, as helium (or hydrogen) gas from a pulsed valve expands over the discharge region (Figure I.3). The plasma created, containing the evaporated material, is cooled in the gas expansion down the extender tube, generating clusters as the jet condenses. This source has the ability to dissociate diatomic molecules (including hydrogen, nitrogen, oxygen, and chlorine), however, is limited to conductive samples (i.e. metals).

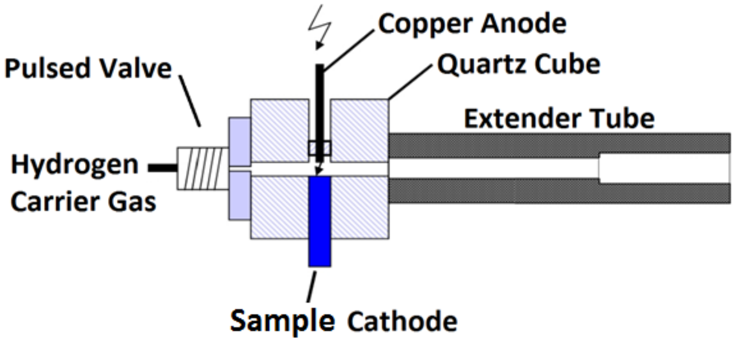

Figure I.3: Schematic diagram of the pulsed arc cluster ionization source (PACIS).

I.2. MASS SPECTROMETER (TIME-OF-FLIGHT)

Ions created in the source travel into a Wiley-Mclaren type pulsed extraction region, defined by two parallel grids, where kinetic energy (KE, -1400 eV) is imparted to the ions by an electrostatic field that accelerates the ions into a field-free drift tube perpendicularly from their birth trajectory (Figure I.1).[2,3] The KE imparted to the ions is proportional to the charge of the ion (q), the distance traveled by the ions within the extraction region (d), and the magnitude of the electric field (E), where

$$KE = qdE \tag{1}$$

From the familiar classical mechanics definition of kinetic energy of a point object

$$KE = \tfrac{1}{2}mv^2 \tag{2}$$

ions of equal charge, but different mass (m) accelerate to different velocities (v). By relating the two KE equations, the velocity of the ion is inversely proportional to the square of its mass, and thus, the flight time of the ion is mass dependent.

$$v = \sqrt{\frac{2qdE}{m}} \tag{3}$$

Since the ions of different mass require different times to reach the detector, which is positioned at the end of the drift tube (distance, D), a mass spectrum can be produced by converting the recorded ion signal versus time (t).

$$t = \frac{D}{\sqrt{2qdE}} * \sqrt{m} \tag{4}$$

Ions are mass selected using a mass gate composed of a grid held at an opposing potential (-1700 V), only allowing the ions of interest through when a well-timed pulse lowers the grid potential to ground.[4]

I.3. PHOTOELECTRON SPECTROMETER

I.3.1. Magnetic Bottle Energy Analyzer

The selected mass-packet then enters a momentum decelerator region where the longer floated element is pulsed to a voltage greater than the magnitude of the ion KE (V_{MD}=-V_{ION}), just as the ions enter the tube.[5] The ions experience a strong decelerating field in the gap between the floated and the grounded (second) element because to the ions in the tube, the ground has been elevated to –V_{MD} (i.e. V_{ION}). The KE of the ion packet is reduced and the ions are focused to a point in the grounded element, known as the interaction region. In the interaction region a photon, from either Nd:YAG (532 nm, 355 nm, or 266nm) or Excimer laser (193nm or 157 nm), crosses the ions. The resulting photodetached electrons are energy analyzed via a magnetic bottle.[6] A strong magnetic field, created by permanent magnet (NdFeB) just below the interaction region and a weak field generated by a solenoid wrapped above the interaction region along the drift tube (~7 feet) to the microchannel plate (MCP) detector, creates an inhomogeneous magnetic field which resembles a bottle. The photodetached electrons follow the Lorentz force, in a spiraling path, along the magnetic field lines from the high field to low field.[7] The arrival time of the electrons traveling from the interaction region to the MCP detector is measured. Since all electrons have the same mass, the flight time of the detected electrons is a result of the differences in electron kinetic energies. The spectra obtained are calibrated against the well-known transitions of atomic copper anion to which the resolution (FHWM) of the magnetic bottle analyzer is ~50meV.

I.3.2. Velocity Map Imaging (VMI) Energy Analyzer

Velocity map imaging (VMI) can be used instead of the magnetic bottle to energy analyze photodetached electrons. After the mass gate, the mass selected ion-packet, is guided into the aperture of the VMI stack using an electrostatic deflector and lens set. The ions continue into a rereferencing tube where a potential is quickly pulsed on to the voltage of the repeller electrode of the VMI stack, once the ions are inside the tube. When the ions reach the interaction region, between the repeller and 1st (first) extractor electrode of the VMI stack, a photon from a Nd:YAG (1064, 532, or 266 nm) crosses the ion beam. The resulting photodetached electrons are mapped onto the pulsed imaging detector (P-MCP), co-linear to the ion beam. A pulsed collar (PC) element is used to prevent ions from hitting the imaging detector, by applying a pulsed negative voltage just nanoseconds after the electrons reach the P-MCP. Refer to Andrej Grubisic's and Jacob Graham's theses for additional information.

REFERENCES

1. Grubisic, A. PhD. Dissertation, Johns Hopkins University, 2009.

2. Wiley, W. C.; McLaren, I. H. *Rev. Sci. Instrum.* **1955**, *26*, 1150.

3. de Heer, W. A.; Milani, P. *Rev. Sci. Instrum.* **1991**, *62*, 670.

4. Wang, L.-S.; Ding, C.-F.; Wang, X.-B.; Barlow, S. E. *Rev. Sci. Instrum*. **1999**, *70*, 1957.

5. Markovich, G.; Giniger, R.; Levin, M.; Cheshnovsky, O. *J. Chem. Phys*. **1991**, *95*, 9416.

6. Kruit, P.; Read, F. H. *J. Phys. E Sci. Instrum*. **1983**, *16*, 313.

7. Cheshnovsky, O.; Yang, S. H.; Pettiette, C. L.; Craycraft, M. J.; Liu, Y.; Smalley, R. E. *Chem. Phys. Lett.* **1987**, *138*, (2-3), 119.

8. Graham, J. PhD. Dissertation, Johns Hopkins University, 2015.

Chapter II: Metal Oxide Cluster Anions

Metal oxides are ionic solids that serve many roles across scientific disciplines including chemistry, physics, and material science. Most notably, metal oxides are important in catalysis. The acid-base redox properties vary depending on the metal atom in the metallic oxide cluster and thus, can be tailored for a desired reaction. The chemical properties of some metal oxides differ from their atomic metal component which is attributed to the difference in electronic structure between the atom and the cluster. What is even more fascinating is that the electronic structure of some metal oxide clusters is very similar to the atomic structure of a transition metal on the period table. Here, the electronic structure of the super-alkalis, Li_3O and Na_3O, as well as ZrO and HfO, were determined using anion photoelectron spectroscopy.

II.1. Photoelectron Spectroscopy of the Molecular Anions, Li_3O^- & Na_3O^-

Di Wang, Jacob D. Graham, Allyson M. Buytendyk, and Kit H. Bowen, Jr.

Department of Chemistry, Johns Hopkins University, Baltimore, Maryland 21218, USA

ABSTRACT

The molecular anions, Li_3O^- and Na_3O^- were produced by laser vaporization and studied via anion photoelectron spectroscopy. Li_3O^- and Na_3O^- are the negative ions of the super-alkali neutral molecules, Li_3O and Na_3O. A two-photon process involving the photodetachment of electrons from the Li_3O^- and Na_3O^- anions and the photoionization of electrons from the resulting Li_3O and Na_3O neutral states was observed. The assignment of the Li_3O^- photoelectron spectrum was based on computational results provided by Zein and Ortiz (see the companion paper).

II.1.1. INTRODUCTION

A super-alkali is a molecule or cluster with an ionization potential (IP) that is less than that of the cesium atom, which is 3.9 eV.[1] The alkali sub-oxides, Li_3O and Na_3O, both satisfy this condition, these molecules being respectively described as Li_3O^+ and Na_3O^+ closed shell cations, each with a hydrogenic electron.[2] Modern theoretical work on the structures of neutral Li_3O and Na_3O and on cationic Li_3O^+ and Na_3O^+ find them all to exhibit D_{3h} symmetries.[3-8] Moreover, the bond lengths of the neutral molecules and their cations are similar in both cases. The ionization potentials of Li_3O and Na_3O have been studied both experimentally and theoretically,[1-5,8-16] with a recent value of 3.55 eV[11,12] being measured for Li_3O (3.69 eV[13] is the most recent value for Na_3O). The excited neutral states of Na_3O and Li_3O have been mapped by the experiments of Hampe *et al.*[13] and Neukermans *et al.*[7], respectively.

The anion, Li_3O^-, together with the ground and excited states of its Li_3O neutral counterpart have been studied theoretically by Simons and Gutowski[4] and recently by Zein and Ortiz.[22] Simons and Gutowski showed the Li_3O^- anion to have two bound states, a $^1A_1'$ state with D_{3h} symmetry and a pseudo-rotating $^3E'$ state. Zein and Ortiz also found two bound states for the Li_3O^- anion, a singlet $^1A_1'$ state with D_{3h} symmetry and a triplet $^3A_1$ state with C_{2V} symmetry. Simons and Gutowski reported the vertical detachment energy (VDE) of Li_3O^- to be 0.656 eV, while Zein and Ortiz found the VDE values of the anions' singlet and triplet states to be 0.65 eV and 0.45 eV, respectively. Both groups found the VDE values to be essentially the same as their electron affinity (EA) values.

Here, we present an anion photoelectron spectroscopic study of Li_3O^- and its isoelectronic analog, Na_3O^-. As alkali-like molecules, Li_3O and Na_3O are expected to have both low ionization potential and low electron affinity (EA) values. (The EA values of alkali atoms lie in the range, 0.4 – 0.6 eV.) Thus, with ~3.5 eV photons, one should be able to photodetach electrons from Li_3O^- and Na_3O^- anions and then with another photon to photoionize electrons from resulting Li_3O and Na_3O neutral states, thereby producing electrons from both photodetachment and photoionization in the same photoelectron spectrum. As a result of this two photon process, Li_3O^- anions, Li_3O neutral ground and excited states, Li_3O^+ cations, and free electrons all exist together in the anion-photon interaction region at essentially the same time. An analogous situation occurs for the tri-sodium mono-oxide case.

II.1.2. EXPERIMETAL

Anion photoelectron spectroscopy is conducted by crossing a mass-selected beam of negative ions with a fixed-frequency photon beam and energy-analyzing the resultant photodetached electrons. This technique is governed by the energy-conserving relationship, $h\nu = \text{EBE} + \text{EKE}$, where $h\nu$ is the photon energy, EBE is the electron binding energy, and EKE is the measured electron kinetic energy. Our apparatus consists of a laser vaporization anion source, a linear time-of-flight mass spectrometer for mass analysis and mass selection, a momentum decelerator, a magnetic bottle electron energy analyzer, and a Nd:YAG laser. The magnetic bottle has a resolution of ~50 meV at EKE = 1 eV. In these experiments photoelectron spectra were recorded with 355 nm (3.49 eV) photons, i.e., the 3rd harmonic of a Nd:YAG laser. The photoelectron spectra were calibrated against the well known transitions of atomic Cu^-.

In this work Li_3O^- anions were prepared by laser-ablating a translating, rotating, 12.7 mm rod of 99.9% lithium metal with 532 nm (2.33 eV) photons, i.e., 2nd harmonic of another Nd:YAG laser. To promote the formation of Li_3O^- anions, water vapor was entrained in 110 psi of helium carrier gas and expanded over the ablation region. Na_3O^- anions were produced in a similar manner with pieces of 99.9% sodium pressed into the shape of a ~6 mm rod, which was then ablated.

II.1.3. RESULTS

The photoelectron spectra of Li_3O^- and Na_3O^- are presented in Figure II.1. In the photoelectron spectrum of Li_3O^-, transitions are observed which are centered at EBE = 0.6, 1.1, 1.8, 1.9, 2.3, 3.0, and 3.5 eV. The peaks at EBE = 1.8, 1.9, and 3.5 eV are much more intense than the others, and the feature at EBE = 2.3 eV shows evidence of additional sub-structure.

An almost identical set of peaks appears in the isoelectronic Na_3O^- spectrum, although, most peaks are shifted by ~0.05 eV toward higher electron binding energies. However, the two strongest peaks (at EBE = 1.75 and 1.85 eV) are exceptions; they are shifted ~0.05 eV toward lower electron binding energies than the analogous Li_3O^- peaks. There are also other differences. The peak near EBE = 3.5 eV is less intense in the Na_3O^- spectrum than in the Li_3O^- spectrum, and two distinct peaks are present at EBE = 2.3 and 2.5 eV in the Na_3O^- spectrum, compared to the less defined feature at EBE = 2.3 eV in the Li_3O^- spectrum.

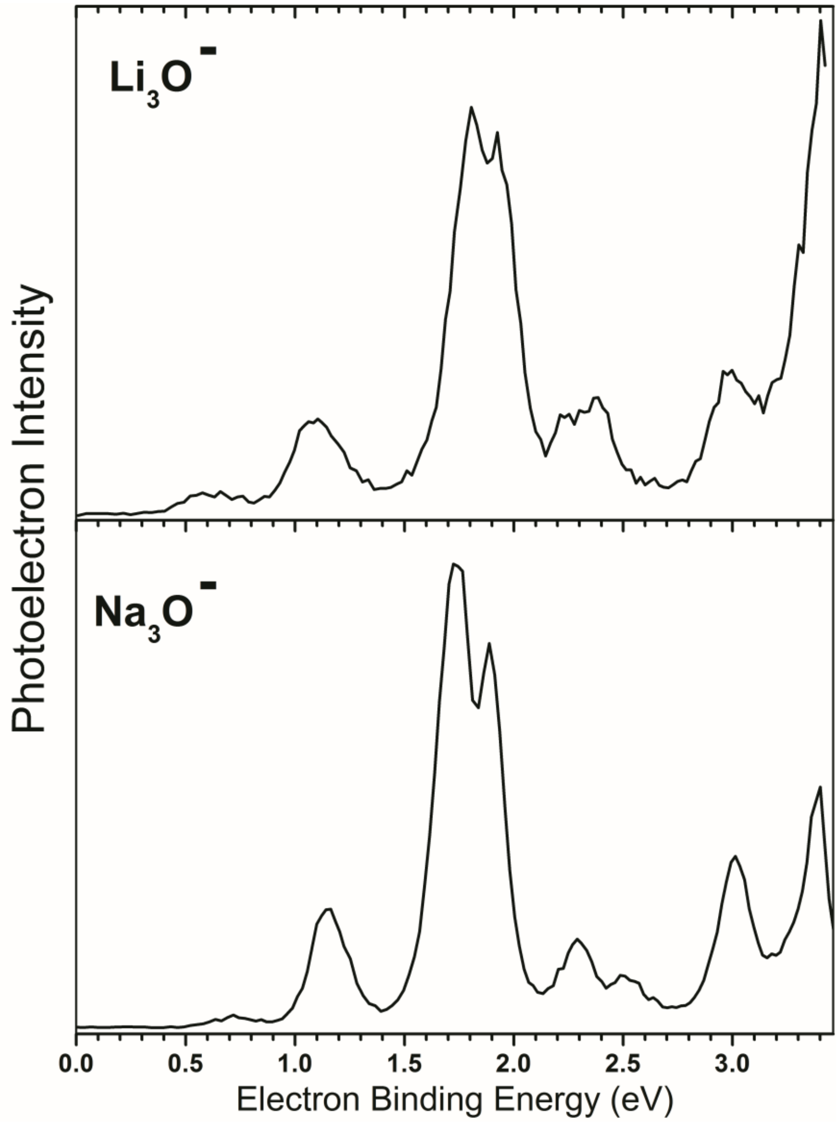

Figure II.1: Photoelectron spectra of Li$_3$O$^-$ (top) and Na$_3$O$^-$ (bottom) each recorded with 3.49 eV photons.

In both Li$_3$O$^-$ and Na$_3$O$^-$ photoelectron spectra the observed transitions are due to both photodetachment and photoionization. As described above, the energetics for such a two photon process are feasible for these two anions. In addition, most pulsed lasers easily have enough power for two photon processes. Another two photon process that can sometimes compete with photodetachment is photodissociation. There, the mass-selected anion is decomposed into neutral and anion fragments, with the latter in turn undergoing photodetachment. We see no evidence for this process having contributed electrons to the photoelectron spectra of Li_3O^- and Na_3O^-. Anionic products of photodissociation would likely include the atomic anions, Li^-, Na^-, and/or O^-. All of these would have sharp peaks that would likely protrude out of the observed bands at well known EBE values, and none do. Moreover, all possible neutral photodissociation products have ionization potentials that are significantly greater than the 3.49 eV photon energy used in these experiments.

II.1.4. DISCUSSION

In order to assign the transitions in the photoelectron spectrum of Li_3O^-, we have relied on the calculations of Zein and Ortiz for support.[22] While analogous calculations are not available for the tri-sodium mono-oxide case, the spectral similarity between the photoelectron spectra of Na_3O^- and Li_3O^- suggests that a very similar set of computational results would be found if such calculations were to be conducted. Thus, our assignments herein focus only on the Li_3O^- spectrum. Anticipating both photodetachment and photoionization transitions in the photoelectron spectrum of Li_3O^-, Zein and Ortiz calculated the vertical detachment energies (VDE) from the anions' singlet and triplet states to the ground state of neutral Li_3O at the CCSD(T) level of theory (0.65 eV and 0.45 eV, respectively) and the ionization potentials of the ground and excited states of neutral Li_3O, in both D_{3h} and C_{2v} symmetries, at the BD-T1 level of theory.

Utilizing their computational results, we constructed an energy level diagram on which the energies of the ground state ($^1A_1'$) Li_3O^- anion, the ground and excited states of the D_{3h} Li_3O neutral, and the ground state of the Li_3O^+ cation were quantitatively placed relative to one another (see Figure II.2). In constructing this energy level diagram, the energies of the ground and excited neutral Li_3O states were plotted relative to the ground state of the Li_3O^+ cation based on their IP values as calculated at the BD-TI level of theory. The energy of the anion's singlet ground state was located on this diagram by placing it below the BD-T1 ionization energy of the neutral Li_3O ground state by an energy equal to its CCSD(T) VDE value.

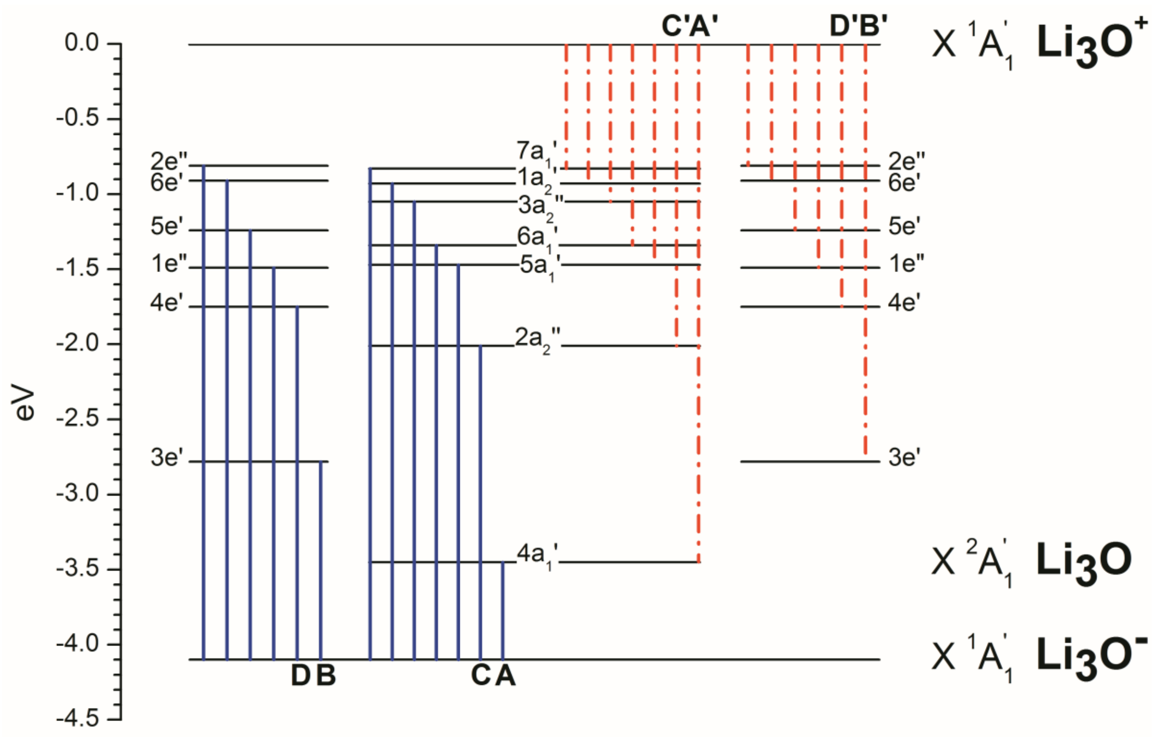

Figure II.2: Energy level diagram on which the energies of the ground state ($^1A_1$') Li_3O^- anion, the ground and excited states of the D_{3h} Li_3O neutral, and the ground state of the Li_3O^+ cation are quantitatively placed relative to one another. Vertical solid lines denote the anion-to-neutral transitions, while vertical dashed lines denote the neutral-to-cation transitions.

We did not include the $^3A_1$ Li_3O^- anion on this diagram for two reasons; there was little indication for a separate peak at EBE = 0.45 eV, the VDE predicted for anion's triplet state, and with an energy separation of 0.22 eV between the anions' singlet and triplet states, an anion temperature of ~1,100 K would have been required to achieve a 10% population of the excited triplet state. Thus, it is expected that the Li_3O^- anion's triplet played only a minor role in the Li_3O^- photoelectron spectrum, and that the majority of the observed photodetachment transitions originated from the $^1A_1'$ singlet, ground state of the Li_3O^- anion.

Since every photoionization transition originated from a neutral Li_3O state that had itself been formed by the photodetachment of a Li_3O^- anion, all neutral state-to-cation transitions are paired with singlet anion-to-neutral state transitions (see corresponding primed and unprimed capital letters in Figure II.2). Using these transition energies, we now present the spectral assignment of the Li_3O^- photoelectron spectrum. These are marked with same lettering scheme of the Li_3O^- photoelectron spectrum in Figure II.3. The band centered at EBE = 0.6 eV is attributed to the photodetachment transition from the singlet, ground state, anion to the doublet, ground state, neutral species with a $4a_1'$ electronic configuration; it contains the spectrum's origin transition and corresponds to the transition labeled, **A** in Figures II.2 and II.3. Thus, the VDE value of Li_3O^- is determined to be 0.6 eV. However, since this band is not vibrationally resolved, we cannot precisely determine the EA value of Li_3O from it. Nevertheless, our measured VDE value and the EA value implied by our result are consistent with the VDE and EA values reported by both Gutowski and Ortiz. The peaks at EBE = 1.1, 2.3, and 2.4 eV are transitions from the anion to excited neutral states with electronic configurations 3e', $2a_2''$, and 4e', respectively, and these correspond to transitions labeled, **B**, **C**, and **D**. The peak at EBE = 3.45 eV is the photoionization transition from the HOMO of the ground neutral ($4a_1$') to the cation and is labeled, **A'**. Transitions to the cation originating from the HOMO+1 and HOMO+2 (3e') of the neutral are labeled, **B'** and correspond to the observed peak at EBE = 3.0 eV. The peaks at EBE = 1.8 and 1.7 eV are from the HOMO+3 ($2a_2$'') as well as from HOMO+4 and HOMO+5 (4e') of the neutral, and they are labeled **C'** and **D'**, respectively. Additionally, the EBE = 1.1 eV peak could contain photoionization transitions originating from higher (hydrogenic) neutral states. This assignment is in accord with that made by Zein and Ortiz in their companion paper.[22]

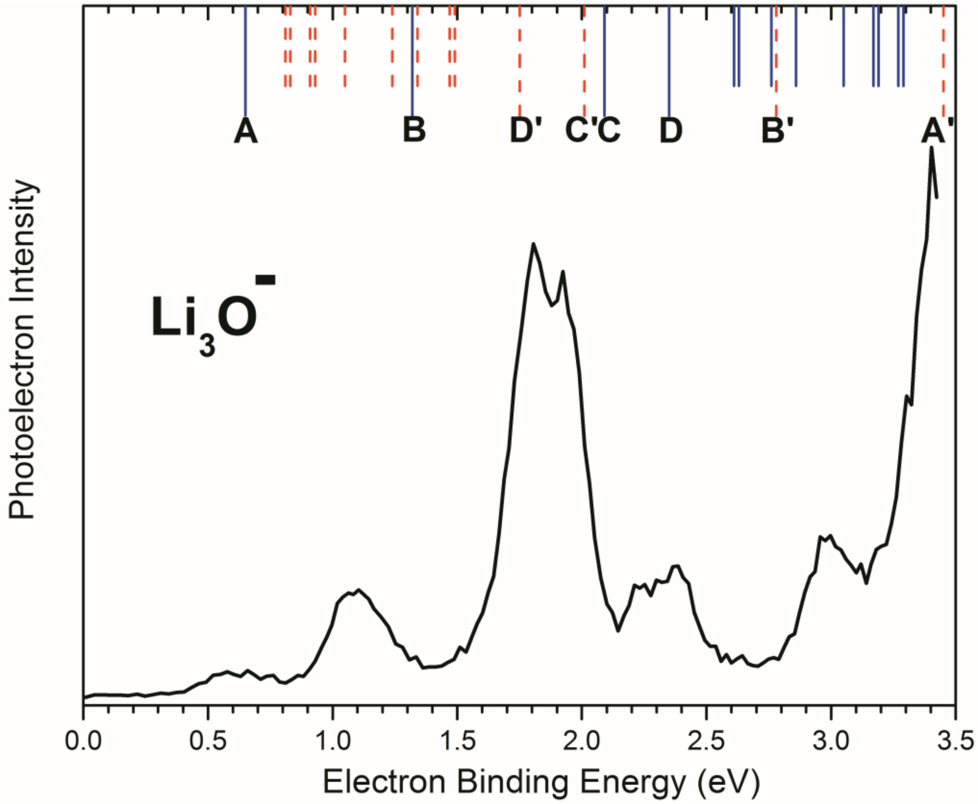

Figure II.3: Spectral assignments for the photoelectron spectrum of Li_3O^-. The vertical solid sticks depict photodetachment transitions, while vertical dashed sticks depict photoionization transitions. Specific photodetachment transitions in Figure 2 are labeled **A**, **B**, **C**, and **D**, while specific photoionization transitions in Figure 2 are labeled **A'**, **B'**, **C'**, and **D'**.

Among the reasons for interest in Li_3O^- is the fact that it is isoelectronic with the elusive, double Rydberg anion, H_3O^-, and studying one might shed light on the other.[4,17,18] The double Rydberg anion, H_3O^- would consist of the closed shell, C_{3v} symmetry, H_3O^+ cation core and two Rydberg-like electrons. While the $H^-(H_2O)$ and $OH^-(H_2)$ complexes have been observed experimentally,[19,20] the double-Rydberg H_3O^- has not. Because there would be little structural change upon removing an excess electron, the photoelectron spectrum of H_3O^- would be expected to be dominated by a single, narrow peak at EBE ~ 0.5 eV, just as was seen in the photoelectron spectrum of the double Rydberg anion, NH_4^-.[21] The photoelectron spectra of the Li_3O^- and Na_3O^- anions lack this spectral signature. Moreover, the symmetry of the ground state Li_3O^- anion is D_{3h} and not C_{3v}, as it would be in the case of H_3O^-. It is clear that Li_3O^- is not analogous to the H_3O^- double Rydberg anion.

ACKNOWLEDGEMENT

This material is based upon work supported by the National Science Foundation under Grant No. CHE-0809258. We also thank S. Zein and V. Ortiz for stimulating discussions.

REFERENCES

1. G. L. Gutsev, and A. I. Boldyrev, Chem. Phys. Lett., **92**, 262 (1982).

2. V. G. Zakrzewski, W. Vonniessen, A. I. Boldyrev, and P. V. Schleyer, Chem. Phys. Lett., **197**, 195 (1992).

3. E. Rehm, A. I. Boldyrev, and P. v. R. Schleyer, Inorg. Chem., **31**, 4834 (1992).

4. M. Gutowski, and J. Simons, J. Phys. Chem., **98**, 8326 (1994).

5. S. D. Elliott, and R. Ahlrichs, J. Chem. Phys., **109**, 4267 (1998).

6. E. U. Wurthwein, P. V. Schleyer, and J. A. Pople, J. Am. Chem. Soc., **106**, 6973 (1984).

7. S. Neukermans, E. Janssens, H. Tanaka, R. E. Silverans, P. Lievens, K. Yokoyama, and H. Kudo, J. Chem. Phys., **119**, 7206 (2003).

8. K. Yokoyama, H. Tanaka, and H. Kudo, J. Phys. Chem. A, **105**, 4312 (2001).

9. H. Kudo, C. H. Wu, and H. R. Ihle, J. Nucl. Mater., **78**, 380 (1978).

10. C. H. Wu, H. Kudo, and H. R. Ihle, J. Chem. Phys., **70**, 1815 (1979).

11. P. Lievens, P. Thoen, S. Bouckaert, W. Bouwen, F. Vanhoutte, H. Weidele, R. E. Silverans, A. Navarro-Vazquez, and P. V. Schleyer, J. Chem. Phys., **110**, 10316 (1999).

12. J. Viallon, M. A. Lebeault, F. Lepine, J. Chevaleyre, C. Jonin, A. R. Allouche, and M. Aubert-Frecon, Eur. Phys. J. D, **33**, 405 (2005).

13. O. Hampe, G. M. Koretsky, M. Gegenheimer, C. Huber, M. M. Kappes, and J. Gauss, J. Chem. Phys., **107**, 7085 (1997).

14. S. D. Elliott, and R. Ahlrichs, Phys. Chem. Chem. Phys., **2**, 313 (2000).

15. P. D. Dao, K. I. Peterson, and A. W. Castleman, J. Chem. Phys., **80**, 563 (1984).

16. D. T. Vituccio, R. F. W. Herrmann, O. Golonzka, and W. E. Ernst, J. Chem. Phys., **106**, 3865 (1997).

17. J. Simons, and M. Gutowski, Chem. Rev., **91**, 669 (1991).

18. J. Melin, and J. V. Ortiz, J. Chem. Phys., **127**, 014307 (2007).

19. E. Debeer, E. H. Kim, D. M. Neumark, R. F. Gunion, and W. C. Lineberger, J. Phys. Chem., **99**, 13627 (1995).

20. T. M. Miller, A. A. Viggiano, A. E. S. Miller, R. A. Morris, M. Henchman, J. F. Paulson, and J. M. Vandoren, J. Chem. Phys., **100**, 5706 (1994).

21. S.-J. Xu, J. M. Nilles, J. H. Hendricks, S. A. Lyapustina, and K. H. Bowen, J. Chem. Phys. **117**, 5742 (2002).

22. S. Zein, and J. V. Ortiz, J. Chem. Phys. **135**, 164307, (2011), companion paper.

II.2. Photoelectron Spectroscopy of the Molecular Anions: ZrO^-, HfO^-, $HfHO^-$, and HfO_2H^-

Xiang Li, Weijun Zheng, Angela Buonaugurio, Allyson Buytendyk, and Kit Bowen*

Departments of Chemistry and Materials Science, Johns Hopkins University, Baltimore, MD 21218

Krishnan Balasubramanian

College of Science, California State University, East Bay, Hayward, CA 94542
Chemistry and Material Science Directorate Lawrence Livermore National Laboratory Livermore, California 94550
Lawrence Berkeley National Laboratory, Berkeley, California 94720

ABSTRACT

Negative ion photoelectron spectra of ZrO^-, HfO^-, $HfHO^-$, and HfO_2H^- are reported. Even though zirconium- and hafnium-containing molecules typically exhibit similar chemistries, the negative ion photoelectron spectral profiles of ZrO^- and HfO^- are dramatically different from one another. By comparing these data with relevant theoretical and experimental studies, as well as by using insights drawn from atomic spectra, spin-orbit interactions, and relativistic effects, the photodetachment transitions in the spectra of ZrO^- and HfO^- were assigned. As a result, the electron affinities of ZrO and HfO were determined to be 1.26 ± 0.05 eV and 0.6 ± 0.05 eV, respectively. The anion photoelectron spectra of $HfHO^-$ and HfO_2H^- are similar to one another and their structural connectivities are likely to be $(H\text{-}Hf\text{-}O)^-$ and $(O\text{-}Hf\text{-}OH)^-$, respectively. The electron affinities of HfHO and HfO_2H are 1.70 ± 0.05 eV and 1.73 ± 0.05 eV, respectively.

II.2.1. INTRODUCTION

Transition metal oxides are technologically important because of the roles they play in catalytic processes and in high temperature chemistry. While zirconium and hafnium are generally thought to have similar chemical properties, some of their oxides show dissimilarities. In particular, ZrO_2 and HfO_2 show significant differences,[1,2] which our previous work had attributed to subtle differences in their electronic structures.[3]

In the present work, we focus on the molecules, ZrO, HfO, HfHO, and HfO_2H and their anions. ZrO has been the subject of many spectroscopic investigations.[4-12] Based on both experiments and theoretical calculations,[13,14] the ground state of ZrO is generally thought to be $^1\Sigma^+$, although some calculations[15] found it to be $^3\Delta$. Kaledin *et al.*[5] have provided copious information on the electronic states of ZrO via wavelength-resolved fluorescence excitation studies. In addition, thermochemical and thermodynamic properties of ZrO have also been reported.[16,17] Furthermore, there have been two previous anion photoelectron studies of ZrO^-, with the more recent one suggesting that ZrO may mimic the chemistry of palladium.[18-20]

HfO has also been the subject of both spectroscopic and theoretical studies, these as in the case of ZrO also suggesting that its ground state is $^1\Sigma^+$.[6,11,21-23] Again, Kaledin *et al.*[21] measured the term energies of its electronic states. In addition, the thermodynamic properties of HfO,[16] as well as the lifetimes[24] and dipole moments[25] of some HfO excited states have also been studied.

Here, we report the anion photoelectron spectra of ZrO^-, HfO^-, $HfHO^-$, and HfO_2H^-. The photoelectron spectra of ZrO^- and HfO^- are quite different from each other, suggesting significantly different electronic structures between these two, same-group transition metal monoxides. Information on the neutral electronic states of ZrO[5] and HfO[21] was used to make assignments of our anion photoelectron spectra, and the electron affinities (EA) of ZrO and HfO were extracted from their respective anion photoelecron spectra. The anion photoelectron spectra of $HfHO^-$ and HfO_2H^- show a strong similarity to one another. Electron affinity values for HfHO and HfO_2H, along with structural insights, are reported.

II.2.2. EXPERIMENTAL

Negative ion photoelectron spectroscopy is conducted by crossing a mass-selected beam of negative ions with a fixed-frequency laser beam and energy-analyzing the resultant photodetached electrons. This technique is governed by the energy-conserving relationship, $h\nu$ = EBE + EKE, where $h\nu$ is the photon energy, EKE is the measured electron kinetic energy, and EBE is the electron binding energy, i.e., the anion-to-neutral transition energy. These experiment were conducted on an apparatus consisting of a Nd:YAG laser vaporization source, a linear time-of-flight mass spectrometer, a mass gate, a momentum decelerator, a second Nd:YAG laser (for photodetachment), and a magnetic bottle electron energy analyzer. The resolution of our magnetic bottle electron energy analyzer was ~35 meV at an EKE of ~1 eV. The apparatus has been described in the detail elsewhere.[26]

The anions, ZrO^- and HfO^-, were generated in a laser vaporization source by focusing the pulsed (10 Hz), second harmonic (532 nm) beam of a Nd:YAG laser onto a continuously rotating, translating zirconium or hafnium rod. The carrier gas used in the laser vaporization source was highly purified helium, which issued through a pulsed valve with a backing pressure of ~4 atm. The oxides on the surfaces of the zirconium and hafnium rods were found to be adequate for generating the metal oxide anions of interest without the addition of oxygen.

II.2.3. RESULTS

The anion photoelectron spectra of ZrO^- and HfO^- are shown in Figure II.4, and those of $HfHO^-$ and HfO_2H^- are presented in Figure II.5. All of these spectra were recorded with 3.49 eV photons. In all cases, the principal peaks in these spectra are labeled with capital letters; the EBE values of their centers are tabulated in Tables II.1-3 (with uncertainties of ±0.05eV). The spectra of ZrO^- and HfO^- each exhibit three main groupings of peaks, with peak (**B**) at EBE = 1.39 eV dominating the spectrum of ZrO^-, and with peaks (**D**, **E**, **G**) at EBE = 1.78, 1.89, and 2.71 eV dominating the spectrum of HfO^-. The spectra of $HfHO^-$ and HfO_2H^- show similar spectral profiles to one another, where in each case strong, relatively sharp peaks (labeled **A** in both cases) located at EBE = 1.70 and 1.73 eV, respectively dominate their spectra.

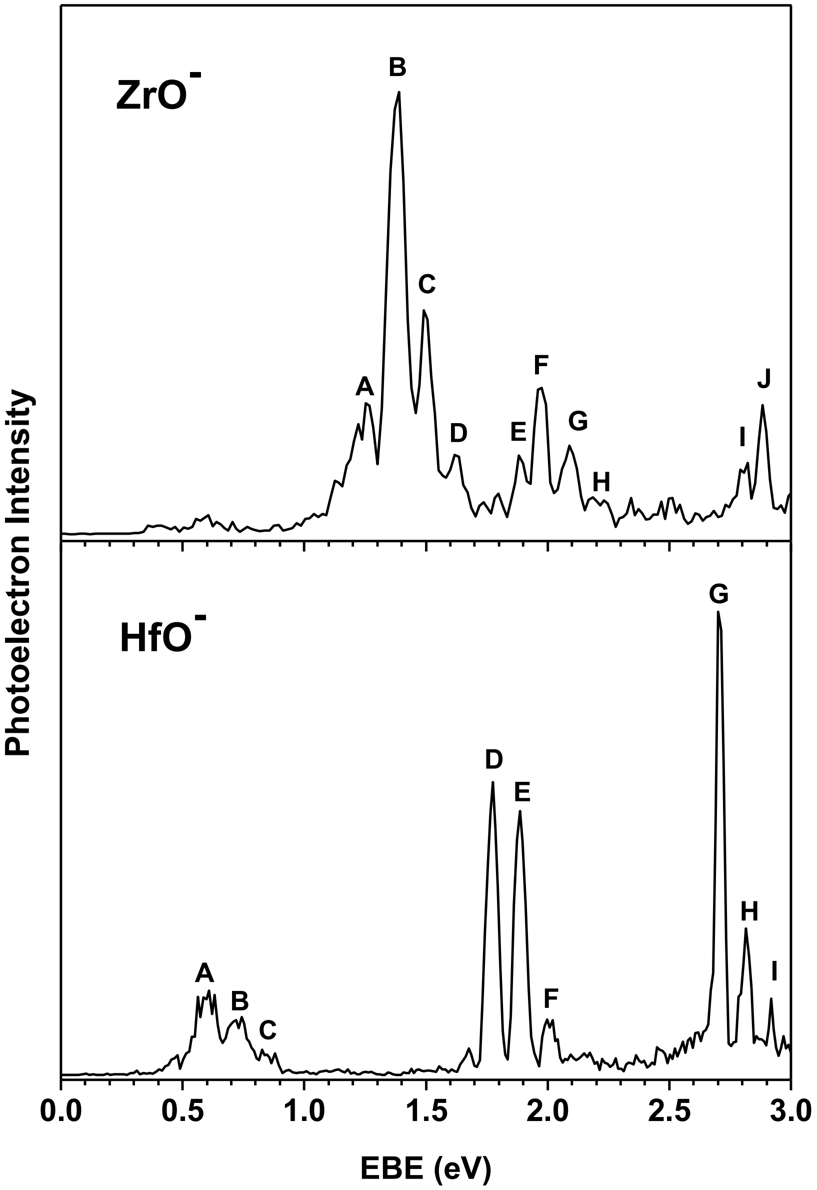

Figure II.4: Anion photoelectron spectra of ZrO$^-$ and HfO$^-$ recorded with 3.493 eV (355nm) photons.

Table II.1: Transition assignments for the photoelectron spectrum of ZrO^-. T_e is the term energy in eV. (Uncertainty of EBE is ±0.05 eV)

Peaks	EBE(eV)	T_e (eV)	Peak assignment: $^2\Delta \rightarrow$	ω_e (cm^{-1})
A	1.26	0	$X^1\Sigma^+$ (v'=0, 5s^2, $\sigma\delta^2$)	---
B	1.39	0.13	$a^3\Delta_1$ (v'=0, 4d^{1}5s^1, $\sigma^2\delta$) and $X^1\Sigma^+$ (v'=1)	890
C	1.50	0.24	$a^3\Delta_1$ (v'=1) and $^3\Delta_2$ (4d^{1}5s^1, $\sigma^2\delta$)	
D	1.62	0.36	$a^3\Delta_1$ (v'=2) and $^3\Delta_3$ (4d^{1}5s^1, $\sigma^2\delta$)	
E	1.88	0.62	($^2\Sigma^- \rightarrow {}^1\Delta_2$)[a] (4d^{1}5s^1, $\sigma^2\delta$)	---
F	1.98	0.72	$A^1\Delta_2$ (v'=0, $\sigma^2\delta$)	880
G	2.09	0.83	$A^1\Delta_2$(v'=1) and $^3\Phi_2$ (4d^2, $\sigma^2\delta$)	
H	2.20	0.94	$A^1\Delta_2$ (v'=2) and $^3\Phi_3$ (4d^2, $\sigma^2\delta$)	
I	2.80	1.54	$b^3\Pi_0$ (4d^2, $\sigma^2\pi$)	---
J	2.88	1.62	$b^3\Pi_1$ (4d^2, $\sigma^2\pi$)	---

[a] Assigned to a transition from an excited state of the anion to the neutral.

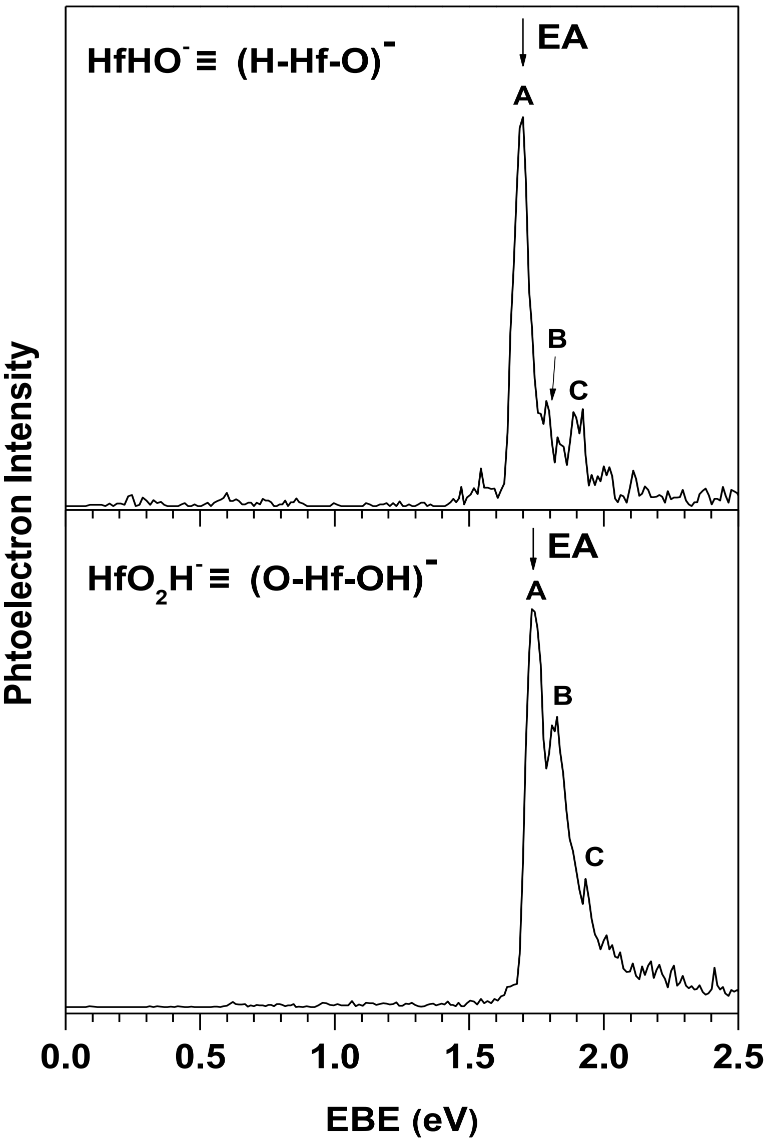

Figure II.5: Anion photoelectron spectra of $HHfO^{-}$ and $OHfOH^{-}$ taken with 3.493 eV (355nm) photons.

Table II.2: Transition assignments for the photoelectron spectrum of HfO^-. T_e is the term energy in eV, and ω_e is the measured vibrational frequency in cm^{-1}. (Uncertainty of EBE is ±0.05 eV)

Peaks	EBE(eV)	T_e (eV)	Peak assignment: $^2\Delta \rightarrow$	ω_e (cm^{-1})
A	0.60	0	$X^1\Sigma^+$ (v’=0, 6s^2, $\sigma\delta^2$)	1050
B	0.73	0.13	$X^1\Sigma^+$ (v’=1)	
C	0.86	0.26	$X^1\Sigma^+$ (v’=2)	
D	1.78	1.18	a($^3\Delta_2 + {}^1\Delta_2$) (v’=0, 5d^{1}6s^1, $\sigma^2\delta$)	890
E	1.89	1.29	a$^3\Delta_1$ (v’=0, 5d^{1}6s^1, $\sigma^2\delta$)	
F	2.00	1.40	a$^3\Delta_1$ (v’=1, 5d^{1}6s^1, $\sigma^2\delta$)	
G	2.71	2.11	b$^3\Pi_0$ (v’=0) (5d^2, $\sigma^2\pi$)	890
H	2.82	2.22	b($^3\Pi_1$+$^1\Pi_1$) (v’=0, 5d^2, $\sigma^2\pi$)	
I	2.92	2.32	b$^3\Pi_2$ (v’=0, 5d^2)	

Table II.3: Measured EA values of HHfO and OHfOH, and the measured vibrational frequency of $OHfOH^-$. (Uncertainty of EBE is ±0.05 eV)

Systems	Peaks	EBE (eV)	ω_e (cm^{-1})
HHfO	A	1.70	730
	B	1.79	
	C	1.89	
OHfOH	A	1.73	810
	B	1.83	
	C	1.93	

II.2.4. DISCUSSION

II.2.4.1 ZrO-

Our anion photoelectron spectrum of ZrO^- is consistent with the previously reported anion photoelectron spectra of ZrO^-,[19,20] although due to differences in resolution and photon energy windows, the present spectrum shows more spectral detail. We assign peak **A** at EBE = 1.26 eV as the origin transition in the photoelectron spectrum of ZrO^-, i.e., the transition from the ground vibrational (v"=0) and electronic ($^2\Delta$) state of the ZrO^- anion to the ground vibrational (v'=0) and electronic ($^1\Sigma^+$) state of neutral ZrO. The ground state of anion was determined based on the fact that the relativistic mass-velocity stabilization of the 6s orbital of Zr would favor the σ orbital over the δ orbital of ZrO^-. It means that the ground state of HfO^- should have been arisen from the $\sigma^2\delta$ configuration ($^2\Delta$) rather than $\sigma\delta^2$ ($^2\Sigma^-$). This assignment determines the adiabatic electron affinity (EA) of ZrO to be 1.26 eV, in agreement with previous experiments and calculations.[14,15,18-20] Peak **A** is the lowest EBE peak which does not vary in intensity with source conditions relative to the other higher EBE peaks. The two slightly lower EBE, shoulder peaks at EBE ~ 1.1 and ~1.2 eV vary with source conditions and are likely to be due to the photodetachment of vibrationally excited ground state anions; they are vibrational hot bands. The low intensity signal in the EBE region between 0.3-0.7 eV was also seen in a previous study and was assigned as an electronic hot band, i.e., as being due to photodetachment transitions from an electronically excited anion.

With the EBE value of the origin transition established, the spectroscopic assignments of neutral ZrO by Kaledin et al.[5] were used to assign the other significant transitions in the anion photoelectron spectrum of ZrO^-. These assignments are presented in Table 1.[5, 36] The most intense feature in the spectrum is peak **B**, located at EBE = 1.39 eV. It and its associated vibronic peaks, **C** and **D**, correspond to transitions from the ground state anion to the various components of the first excited $^3\Delta_1$ state of neutral ZrO. While the **B**-**C** and **C**-**D** spacings were measured to be 890 cm^{-1}, the vibrational frequency of the $^3\Delta_1$ state cannot be unambiguously determined from this spectrum, since the $^3\Delta_2$ spin-orbit component lies in the same region as the vibrational transitions to the $^3\Delta_1$ state, causing the features associated with both to overlap. Nevertheless, we expect the vibrational frequency of the $^3\Delta_1$ state to be very close to the spin-orbit splitting between $^3\Delta_1$ and $^3\Delta_2$ components. (Peak **E** is discussed and assigned below.) Similarly, peak **F**, located at EBE = 1.98 eV and its associated vibronic peaks, **G** and **H**, correspond to transitions from the ground state anion to the second excited state of neutral ZrO, $^1\Delta_2$. The peaks, **G** and **H**, are probably comprised of both transitions to vibrational levels of the $^1\Delta_2$ state and $^3\Phi_2$ and $^3\Phi_3$ spin-orbit components, which arise from the Zr^{2+} (4d^2) configuration. Based on the measured **F**-**G** and **G**-**H** spacing's, the vibrational frequency of the $^1\Delta_2$ state is determined to be 880 cm^{-1}. Furthermore, peak **I**, located at EBE = 2.80 eV and peak **J**, located at EBE = 2.88 eV are respectively assigned to the transitions from the anion ground state to the $^3\Pi_0$ and $^3\Pi_1$ excited states of neutral ZrO. All of these assignments are presented in Table 1.

In proposing these assignments, we have considered both prior assignments and an analysis of analogous electronic states for neutral ZrO. Due to the strong ionic nature of ZrO, we expect that the bonding can be described as being predominantly Zr^{2+}O^{2-}. Thus, the excited electronic states of ZrO can be analyzed and rationalized using the atomic energy levels of Zr^{2+}. Since the isoelectronic Y$^+$ atomic energy levels[27] are readily available, we have used the energy separations between Y$^+$ electronic states to provide additional guidance in the assignment of the observed photoelectron spectra of ZrO^- (see Figure II.6). As seen from

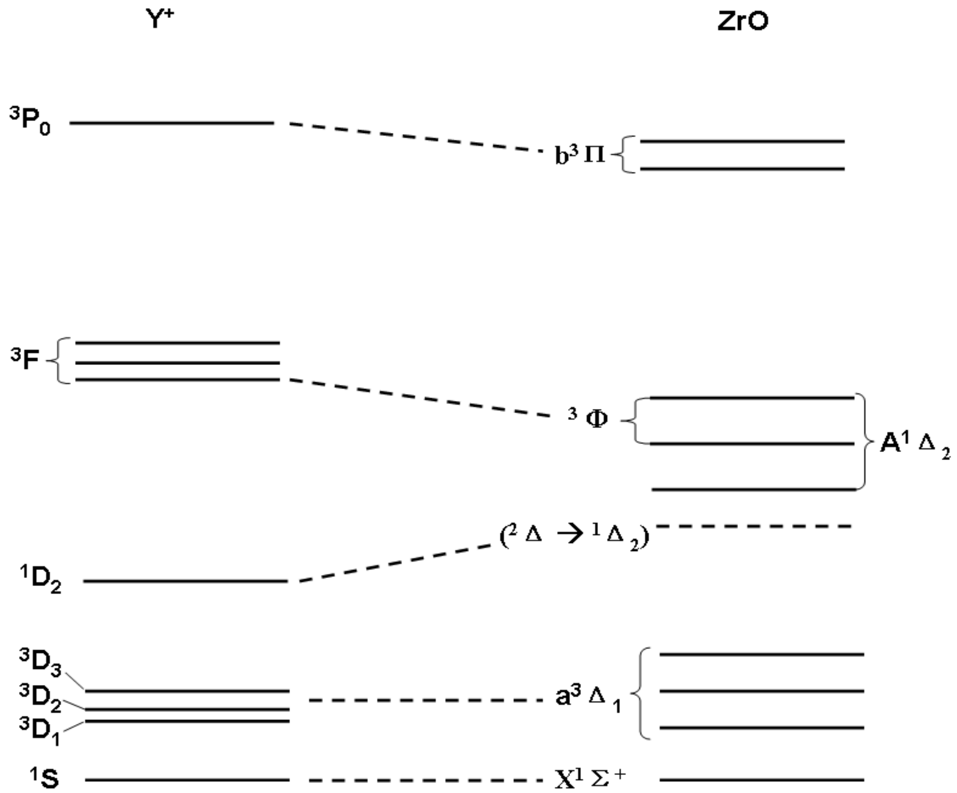

Figure II.6: Comparison between the atomic energy levels of Y^+ and the assigned molecular energy levels of neutral ZrO as extracted from the anion photoelectron spectrum of the ZrO^- anion.

Moore's atomic spectra data[27] the ground state of Y^+ is ^1S with $^3D_1$, $^3D_2$, and $^3D_3$ excited states located at 840, 1045 and 1450 cm^{-1}, respectively, above the ground state. These states could correspond to the observed transitions **B**, **C** and **D** in the anion photoelectron spectrum of ZrO^-. Moreover, the $^1D_2$ excited state of Y^+ at 3,296 cm^{-1} corresponds to the $^1\Delta_2$ excited state of neutral ZrO, which correlates with the $(4d^15s^1)$ configuration of Zr^{2+}. A transition from the $^2\Sigma^-$ electronically excited state of the ZrO^- anion to the $^1\Delta_2$ excited state of neutral ZrO can be assigned to peak **E**, which is an electronic hot band. In addition, the ^3F state of Y^+, arising from the $4d^2$ configuration,[33] has a T_e of 8,003 cm^{-1}, thereby supporting our assignment of peaks, **G** and **H**, to the $^3\Phi_2$ and $^3\Phi_3$ spin-orbit components. Finally, the $^3P_0$ state of Y^+ is observed at 13,883 cm^{-1}, which supports our assignment of peak **I** to a transition terminating on the $^3\Pi_0$ excited state of neutral ZrO and our assignment of peak **J** to a transition terminating on the $^3\Pi_1$ excited state of neutral ZrO.

II.2.4.2 HfO$^-$

We assign peak **A**, located at EBE = 0.60 eV as the origin transition in the anion photoelectron spectrum of HfO$^-$, i.e., the transition from the ground vibrational (v"=0) and electronic ($^2\Delta$) state of the HfO$^-$ anion to the ground vibrational (v'=0) and electronic ($^1\Sigma^+$) state of neutral HfO. Similarly to ZrO$^-$, the ground state of HfO$^-$ anion was determined to have arisen from the $\sigma^2\delta$ configuration. This assignment determines the adiabatic electron affinity (EA) of HfO to be 0.60 eV. Peak **A** is the lowest EBE peak which does not vary in intensity with source conditions relative to the other higher EBE peaks. The intensity of the shoulder peak at slightly lower EBE (at 0.48 eV) varies with source conditions and is assigned as being due to the photodetachment of a vibrationally excited, ground electronic state anion; it is a vibrational hot band. Peaks **B** and **C** correspond respectively to transitions from the ground vibrational and electronic state of the HfO$^-$ anion to the v' = 1 and the v' = 2 vibrational levels of the ground electronic state of neutral HfO. The **A**-**B** and **B**-**C** spacings were measured to be 1050 cm^{-1}, and this is a measure of the vibrational frequency of neutral HfO. This value is higher than the literature value,[21] which is 967 cm^{-1}. We attribute this slight discrepancy to the low signal-to-noise ratio observed for this particular band. A Franck-Condon analysis of the band containing peaks **A**, **B**, **C** (using a program developed by Ervin and Lineberger[28]) found the bond length of the HfO$^-$ anion to be 1.759

Å. The literature value of the neutral HfO bond length (and thus the input value utilized in the program) is 1.723 Å. This difference is consistent with the expectation of a weaker bond and longer bond length for the HfO^- anion relative to its neutral HfO counterpart.

With the origin transition tentatively located, the spectroscopic assignments of neutral HfO by Kaledin et al.[21] (see Ref. 36) were used to assign the other significant transitions in the anion photoelectron spectrum of HfO^-. The most intense features in the spectrum are peaks **D**, located at EBE = 1.78 eV, peak **E**, located at EBE = 1.89 eV, and peak **G**, located at EBE = 2.71. Relative to the EBE of peak **A**, peak **D** lies at an EBE which corresponds to a photodetachment transition from the ground state of the HfO^- anion to the $a^3\Delta_1$ excited state of neutral HfO, as assigned by Kaledin.[21] Likewise, peak **E** lies at an EBE which corresponds to a transition to the similarly assigned $a^3\Delta_2$ excited state of neutral HfO. Peak **F** is a vibronic peak, corresponding to a transition from the ground state anion to v' = 1 of the $a^3\Delta_2$ state of neutral HfO. The **E**-**F** spacing, measured to be 890 cm^{-1}, is a measure of the vibrational frequency of the $a^3\Delta_2$ excited state of HfO. In similar fashion, peak **G** lies at an EBE which corresponds to a transition to the $b^3\Pi_0$ excited state of neutral HfO. Peaks **H** and **I** correspond to transitions to higher components of $b^3\Pi$ excited states of neutral HfO. The close correspondence between the energy levels of neutral HfO measured by Kaledin and the peak locations in our observed spectrum confirms our assignment of the origin transition to peak **A**.

As was the case for ZrO above, we have also conducted an analysis of analogous electronic states for neutral HfO in order to further assist in making assignments. This approach involved utilizing the atomic energy levels[27] of La^+. However, because there are lanthanide atoms between lanthanum and hafnium in the periodic table, we scaled the energies of the

La^+ states by the atomic numbers of hafnium and lanthanum in order to make a meaningful comparison. The assignment of peak **A** as the origin transition remains unchanged. However, the assignments of peaks **D** and **E** differ slightly under this approach. Under the assignment based on Kaledin's work,[21] peak **D** is due to a transition from the ground state of the HfO^- anion to the $a^3\Delta_1$ excited state of neutral HfO. Alternatively, peak **D** could be assigned to the $^2\Delta \rightarrow \Omega = 2$ ($^3\Delta_2 + {}^1\Delta_2$) transition. Note that the mixing of $^3\Delta_2$ and $^1\Delta_2$ is expected to be substantial in hafnium due to its large spin-orbit interaction,[29,30] and thus this state could be lowered in energy relative to the $\Omega = 1$ ($^3\Delta_1$) state. This argues for peak **E** being assigned to the $^2\Delta \rightarrow \Omega = 1$ ($^3\Delta_1$) transition. In other words, the Kaledin- based assignments of peaks **D** and **E** should perhaps be switched. In support of this possibility, we note that the corresponding states of La^+ violate Hund's rule in that the $^1D_2$ state of La^+ is lower than the spin-orbit components of the ^3D state due to the mixing of the J=2 components of $^1D_2$ and $^3D_2$.[33] Thus, we tentatively assign peak **D** to a $\Omega = 2$ state, even though an assignment of peak **D** to $^3\Delta_1$ and of peak **E** to $\rightarrow \Omega = 2$ ($^3\Delta_2 + {}^1\Delta_2$) cannot be ruled out. Peak **G** remains assigned to the $^2\Delta \rightarrow {}^3\Pi_0$ transition. Peaks **H** and **I** may simply be transitions to vibrational levels of the $^3\Pi_0$ state. However, the other two spin-orbit components of the $^3\Pi$ state, namely $\Omega = 1$ and $\Omega = 2$ states, can also be candidates for the assignments of peaks **H** and **I**. These assignments are presented in Table II.2.

Upon comparing the anion photoelectron spectra of ZrO^- and HfO^-, it is clear that these two systems show dramatically different spectral profiles. Such differences suggest that a single oxygen atom binding to these transition metals can induce significant changes in electronic properties, even though zirconium and hafnium are usually considered to be nearly chemically identical. More surprisingly, the difference between ZrO^- and HfO^- observed here is more substantial than that between ZrO_2^- and HfO_2^-.[3] We suggest that these spectral differences between HfO and ZrO are due to much larger relativistic effects in hafnium than in zirconium, and indeed, relativistic effects are most dramatically manifested in diatomic species.[31] The relativistic mass-velocity effect stabilizes the 5s orbital of Zr and 6s orbital of Hf. The same effect destabilizes the 4d orbital of Zr and 5d orbital of Hf. Specifically, using HfO as an example, the σ orbital of HfO is expected to be relativistically stabilized by mass-velocity effect while the δ orbital of HfO is expected to be destabilized, due to the fact that its s orbital is composed of the 6s-5d^{z**2} orbital of Hf, while the δ orbital is purely atomic Hf (5d). Indeed, the $^3\Delta$ state of HfO is placed 1.18 eV above the $^1\Sigma^+$ state, which evidently supports relativistic mass-velocity stabilization of the σ orbital of HfO and destabilization of the δ orbital of HfO. In addition, the relativistic mass-velocity stabilization of 6s and the destabilization of 5d is more pronounced for Hf, as it is heavier than Zr (the $^3\Delta$ state of ZrO is only 0.24 eV above the ground state of ZrO whereas the corresponding lowest $^3\Delta$ spin-orbit component is 1.18 eV above the $^1\Sigma^+$ state).

The dissociation energies of the ZrO^- anion into Zr and O^-, $D_0(Zr\text{--}O^-)$, and of the HfO^- anion into Hf and O^-, $D_0(Hf\text{--}O^-)$, can be extracted from our data by utilizing the identity,

$$D_0(X\text{--}O^-) = D_0(X\text{--}O) + EA(XO) - EA(O) \quad (1)$$

where X is either Zr or Hf. Here, we determined that EA(ZrO) = 1.26 eV and that EA(HfO) = 0.60 eV, and EA(O) is known to be 1.461 eV.[32] Furthermore, the dissociation energies of neutral ZrO and HfO, i.e., $D_0(Zr\text{--}O)$ and $D_0(Hf\text{--}O)$, are 7.91 eV[30] and 8.19 eV,[12] respectively. Thus from these values, we can obtain the dissociation energy for their corresponding anions. The results are: $D_0(Zr\text{--}O^-)$ = 7.71 eV and $D_0(Hf\text{--}O^-)$ = 7.33 eV.

Note that the value of $D_0(Zr\text{--}O^-)$ is very close to that of $D_0(Zr\text{--}O)$, i.e., only a difference of 0.20 eV. By comparison, the difference between $D_0(Hf\text{--}O^-)$ and $D_0(Hf\text{--}O)$ is much bigger, i.e., a difference of 0.86 eV.

II.2.4.3 HfHO- and HfO₂H-

The anion photoelectron spectra of $HfHO^-$ and HfO_2H^- are presented in Figure II.5. These two spectra have very similar profiles, in which each displays a strong peak (labeled peak **A**) and two higher EBE transitions (labeled peaks **B** and **C**). All of these transitions are listed in Table II.3. In each case, we assign the peak **A** as the origin transition, this assignment determining the electron affinities of HfHO and HfO_2H to be 1.70 eV and 1.73 eV, respectively. We further assign peaks **B** and **C** in both cases as vibrational transitions associated with their corresponding peak **A**, i.e., transitions to v' = 1 and v' = 2, respectively. The **A**-**B** and **B**-**C** spacings in the spectrum of $HfOH^-$ are essentially the same, at 730 cm^{-1}, while the **A**-**B** and **B**-**C** spacings in the spectrum of HfO_2H^- are the same, at 810 cm^{-1}. In both spectra, their relatively narrow spectral profiles and the curtailed extent of their vibrational progressions suggest that their anionic and neutral structures may be similar. Previous infrared and computational studies have shown that hafnium atoms can insert into O-H bonds to form HHfO.[34,35] Thus, we propose that HfHO and $HfHO^-$ exhibit the structural connectivity, H-Hf-O rather than Hf-O-H and that HfO_2H and HfO_2H^- have the connectivity, O-Hf-O-H.

ACKNOWLEDGEMENTS

This material is based upon work supported by the Division of Materials Science and Engineering, Basic Energy Sciences, U.S. Department of Energy, under KHB's Grant No. DE-FG02-09ER46558. We also thank Maciej Gutowski and Jun Li for helpful discussions.

REFERENCES

1. M. Gutowski, J. E. Jaffe, C.-L. Liu, M. Stoker, R. I. Hegde, R. S. Rai, and P. J. Tobin T, Appl. Phys. Lett. **80**, 1897 (2002).

2. J.E. Lowther, Mater. Res. Bull. **28**, 189 (2003).

3. W. Zheng, K. H. Bowen, J. Li, I. Dabkowska, and M. Gutowski, J. Phys. Chem. A **109**, 11521 (2005).

4. L. Brewer and D. W. Green, High Temp. Sci. **1**, 26 (1969).

5. L. A. Kaledin, J. E. McCord, and M. C. Heaven, J. Mol. Spectro. **174**, 93 (1995).

6. R. D. Suenram, F. J. Lovas, G. T. Fraser, and K. Matsumura, J. Chem. Phys. **92**, 4724 (1990).

7. J. B. Tatum and W. J. Balfour, J. Mol. Spectro. **48**, 292 (1973).

8. J. Jonsson, J. Mol. Spectro. **167**, 42 (1994).

9. J. E. Littleton, S. P. Davis, and M. Song, Astrophys. J. **404**, 412 (1993).

10. B. Simard, S. A. Mitchell, M. R. Humphries, and P. A. Hackett, J. Mol. Spectro. **129**, 186 (1988).

11. W. Weltner and D. McLeod, J. Phys. Chem. **69**, 3488 (1965).

12. G. V. Chertihin and L. Andrews, J. Phys. Chem., **99**, 6356 (1995).

13. S. R. Langhoff and C. W. Bauschlicher, Astrophys. J. **349**, 369(1990).

14. P. E. M. Siegbahn, Chem. Phys. Lett. **201**,15 (1993).

15. P. Song, W. Guan, C. Yao, Z. Su, Z. Wu, J. Feng, and L. Yan, Theoretica. Chimica. Acta. **117**, 407 (2007).

16. R. J. Ackermann, and E. G. Rauh, J. Chem. Phys. 60, 2266 (1974).

17. E. Murad and D. L. Hildenbrand, J. Chem. Phys. **63**, 1133 (1975).

18. O. C. Thomas, S. Xu, T. P. Lippa, and K. H. Bowen, J. Cluster Sci. **10**, 525 (1999).

19. S. J. Peppernick, K. D. D. Gunaratne, and A. W. Castleman, Proc. Natl. Acad. Sci. **107**, 975 (2009).

20. A. W. Castleman, J. Phys. Chem. Lett. **2**, 1062 (2011).

21. L. A. Kaledin, J. E. McCord, and M. C. Heaven, J. Mol. Spectro. **173**, 37(1995).

22. R. S. Ram and P. F. Bernath, J. Mol. Spectro. **169**, 268 (1995).

23. C. Yao, W. Guan, P. Song, Z. Su, J. Feng, L. Yan, and Z. Wu, Theoretica. Chimica. Acta. **117**, 115 (2007).

24. M. Aldener, A. Hansson, A. Pettersson, and U. Sassenberg, J. Mol. Spectro. **216**, 131 (2002).

25. A. Hansson, A. Pettersson, P. Royen, and U Sassenberg, J. Mol. Spectro. **224**, 157 (2004).

26. M. Gerhards, O. C. Thomas, J. M. Nilles, W. J. Zheng, and K. H. Bowen, J. Chem. Phys. **116**,10247 (2002).

27. C. E. Moore, Tables of Atomic Energy Levels, Vol II & III, NSRDS-NBS 35, National Institute of Standards & Technology, Washington DC 1971

28. PESCAL Fortran program, written by K. M. Ervin and W. C. Lineberger

29. G. H. Huber, *Molecular spectra and molecular structure, Vol IV. Constants of diatomic molecules*. Van Nostrand Reinhold Company, New York, 1979.

30. D. Andrae, U. Häußermann, M. Dolg, H. Stoll, and H. Preuß, Theoretica. Chimica. Acta. **77**, 123 (1990).

31. K. Balasubramanian, “Relativistic Effects in Chemistry”, Vols I and II, Wiley Interscience 1997.

32. D. M. Neumark, K. R. Lykke, T. Andersen, and W. C. Lineberger, Phys. ev. A **32**, 1890 (1985).

33. N. D. Gibson, B. J. Davies, and D. J. Larson, J. Chem. Phys. **98**, 5104 (1993).

34. X. Wang and L. Andrews, Inorg. Chem. **44**, 7189 (2005).

35. M. Zhou, L. Zhang, J. Dong, and Q. Qin, J. Amer. Chem. Soc. **122**, 10680 (2000).

36. See Supplementary Material Document at http://dx.doi.org/10.1063/1.4704127 for assignments of the electronic states of neutral ZrO and HfO.

Chapter III: Light Metal Hydride Cluster Anions

Almost 50 years ago, the use of hydrogen was proposed as a substitute for hydrocarbon fuels (i.e. fossil fuels). Hydrogen is a completely combustible fuel which results in zero-emissions. Interest in hydrogen as an alternative to fossil fuels is not only because of its limited environmental impact but hydrogen is also a light-weight molecule and vastly abundant. The main concern, however, is how to safely store large volumes of hydrogen due to its high flammability. Hydrogen can be physically stored as a gas or liquid as well as on the surfaces of solids (by adsorption) or within solids (by absorption). Several metals, Al, Mg, Ti, have been of particular interest in material based hydrogen storage research since they form metal hydrides. Here, the electronic structure of the metal hydrides, MgH and AlH_4 were determined using anion photoelectron spectroscopy in the quest for materials to safely store hydrogen.

III.1. Photoelectron Spectra of the MgH$^-$ and MgD$^-$ Anions

Allyson Buytendyk,[1] Jacob Graham,[1] Haopeng Wang,[1] Xinxing Zhang,[1] Evan Collins,[1]
Y.-J. Ko,[1] Gerd Gantefoer,[2] Bryan Eichhorn,[3] Anushoba Regmi,[4] Kiran Boggavarapu,[4]
and Kit H. Bowen[1]*

[1]*Department of Chemistry, Johns Hopkins University, Baltimore, Maryland 21218, USA*
[2]*Department of Physics, University of Konstanz, 78457 Konstanz, Germany*
[3]*Department of Chemistry, University of Maryland, College Park, MD* 20742, USA
[4]*Department of Chemistry, McNeese State University, Lake Charles, LA 70609, USA*

ABSTRACT

The molecular anions, MgH$^-$ and MgD$^-$ were generated in a pulsed arc cluster ionization source (PACIS) and studied using anion photoelectron, velocity-map imaging spectroscopy. The electron affinities of MgH and MgD were determined to be 0.90 ± 0.05 eV and 0.89 ± 0.05 eV, respectively. These findings were supported by *ab initio* calculations. Our experimental and theoretical results were compared with those from previous studies.

III.1.1. INTRODUCTION

Magnesium hydride, MgH, has been detected in stellar atmospheres through its optical spectrum,[1,2] and as a light metal hydride, it may also find applications in hydrogen storage and in propulsion.[3] Both MgH and MgD have been extensively studied by experimental[1,2,4-9] and computational[10-14] methods. Their negative ions, however, have received less attention. MgH^- anions were first observed almost fifty years ago in a mass spectrometric study which generated them in a Penning discharge negative ion source.[15] At about the same time, semi-empirical calculations predicted the electron affinities of several gaseous radicals, including MgH.[13] A decade later, again using a Penning discharge source, threshold photodetachment experiments were conducted on MgH^- anions by using the combination of a high pressure xenon lamp and a monochromator as a variable wavelength light source.[16] These experiments provided the first measurement of the electron affinity (EA) of MgH. Around the same time, a cesium beam, sputter ion source was developed to produce MgH^- anions for use in heavy ion, tandem accelerator experiments.[17] Somewhat later, theory provided the bond length and vibrational frequency of the MgH^- anion[18] as well as its magnetizability.[19]

Here, we report the generation of MgH^- and MgD^- anions using a third type of anion source, we present their vibrationally-resolved anion photoelectron spectra, we determine the electron affinities of MgH and MgD, we present calculations which support our findings, and we compare our results with those from previous studies. The present anion photoelectron study of the alkaline earth metal hydride anion, MgH^- joins previous photoelectron studies of metal hydride anions including alkali metal,[20] transition metal,[21,22] and semi-metal[23,24] diatomic hydride anions.

III.1.2. METHODS

III.1.2.1 Experimental

Anion photoelectron spectroscopy is conducted by crossing a mass-selected beam of negative ions with a fixed-frequency photon beam and energy-analyzing the resultant photodetached electrons. This technique is governed by the energy-conserving relationship, hν = EBE + EKE, where hν, EBE, and EKE are the photon energy, electron binding (transition) energy, and the electron kinetic energy, respectively.[25] Electron kinetic energy is measured using a velocity-map imaging (VMI)[26,27] spectrometer. There, mass-gated anions are crossed with 532 nm, linearly polarized photons in an electric field, so that resultant photodetached electrons are accelerated along the axis of the ion beam towards a position sensitive detector (75 mm diameter dual microchannel plate detector with a phosphor screen coupled to a CCD camera). The sum of ~50,000 electrons form a 2D image which is then reconstructed into a slice of the 3D distribution via the BASEX[28] method. Photoelectron spectra were calibrated against the well-known photoelectron spectrum of NO^-.

In the present work, MgH^- anions were generated in a pulsed arc cluster ionization source (PACIS), which has been described in detail elsewhere and shown schematically in Figure III.1.[29] Briefly, a ~30 μsec duration, 150 V electrical pulse, applied at 10 Hz across an anode and its sample cathode, vaporized magnesium metal and formed a plasma. Simultaneously, a 200 psi pulse of ultrahigh purity hydrogen gas was delivered into the arc region using a pulsed valve (Parker Series 9). There, many of the H_2 molecules were dissociated into hydrogen atoms and together with magnesium atoms and free electrons were directed down a 20 cm long tube, where they reacted and cooled before exiting into high vacuum. The resulting anions were then extracted into a time-of-flight mass spectrometer, mass-selected using a mass gate, and photodetached with second harmonic photons from a Nd:YAG laser and energy analyzed as described above. MgD^- was generated similarly, but with deuterium gas.

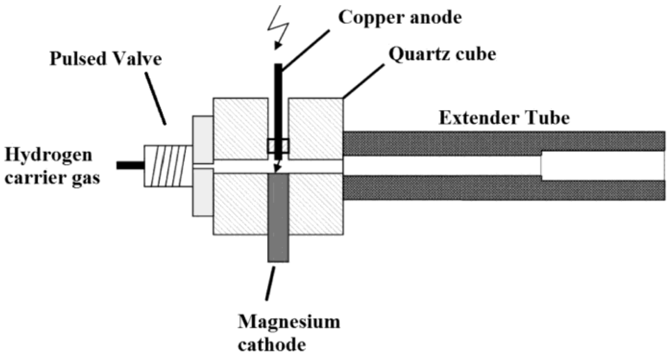

Figure III.1: Schematic diagram of the pulsed arc cluster ionization source (PACIS).

III.1.2.2 Computational

Our calculations were conducted at both the B3LYP/aug-cc-pVQZ and the CCSD(T)/aug-cc-pVQZ levels of theory.[30] Electron affinities were corrected with zero point energies which were calculated at each respective level of theory.[30]

III.1.3. RESULTS AND DISCUSSION

Figure III.2 presents the mass spectrum showing the MgH^- anions. The expected isotopic ratios of magnesium at masses, 24, 25, and 26 amu are reproduced in the intensity pattern of MgH^- anions at masses, 25, 26, and 27. Figure III.3 presents the anion photoelectron spectra of $^{24}MgH^-$ and $^{24}MgD^-$, both measured using 532 nm (2.33 eV) photons.

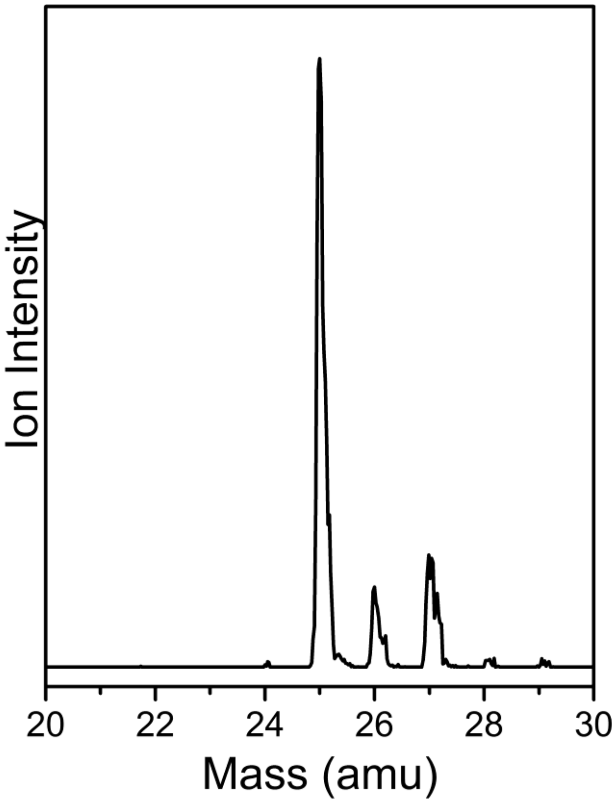

Figure III.2: Mass spectrum showing the three isotopic forms of MgH^- anions.

In the photoelectron spectrum (PES) of MgH^- anion, the observed transitions are centered at EBE = 0.90, 1.08, and 1.24 eV, while in the MgD^- anion spectrum, the transitions are centered at EBE = 0.89 and 1.02 eV. The adiabatic electron affinity, EA, is the energy difference between the lowest energy state of the anion and the lowest energy state of its neutral counterpart. The lowest EBE transition in each spectrum is its origin-containing transition, i.e., the $X\ ^2\Sigma^+$ (v'=0) $\leftarrow$ $X\ ^1\Sigma^+$ (v"=0) transition, and it defines the adiabatic electron affinity. Thus, EA(MgH) and EA(MgD) were determined to be 0.90 ± 0.05 eV and 0.89 ± 0.05 eV, respectively. Our electronic structure calculations, at the B3LYP/aug-cc-pVQZ found the EA for MgH and MgD to be 0.86 eV and 0.85 eV, respectively. Similarly, at the CCSD(T)/aug-cc-pVQZ level of theory, the EA of MgH and MgD were calculated to be 0.86 eV and 0.85 eV, respectively.

The peak separations in the photoelectron spectra of the MgH$^-$ and MgD$^-$ anions agree relatively well with the known vibrational frequencies of MgH and MgD, respectively.[4,5] The spacing between the two lowest EBE peaks in the spectra of MgH$^-$ and MgD$^-$ are 1452 cm^{-1} and 1049 cm^{-1}, respectively, whereas the vibrational frequencies of MgH and MgD are 1495 cm^{-1} and 1078 cm^{-1}, respectively. Therefore, we assigned the three lowest EBE peaks in the photoelectron spectrum of MgH$^-$ as the (0,0), (1,0), and (2,0) vibrational transitions, respectively. Likewise, we assigned the two lowest EBE peaks in the photoelectron spectrum of MgD$^-$ as the (0,0) and (1,0) vibrational transitions, respectively. Peak locations, adjacent peak splitings, and assignments are presented in Table III.1. We also conducted Franck-Condon analyses using the program, PESCAL2010.[31] The best fit is shown as an inset above the photoelectron spectrum of MgH$^-$ in Figure III.3. While hot bands were not evident in the spectra, an anion temperature of ~ 450 K was implied.

Table III.1: Transition assignments for the photoelectron spectra of MgH$^-$ and MgD$^-$

	Peak Location (eV)	**Adjacent Spacing** (cm^{-1})	**Assignment** **X $^2\Sigma^+$ ← X $^1\Sigma^+$** (v’, v”)
MgH$^-$			
	0.90		(0,0)
		1452	
	1.08		(1,0)
		1290	
	1.24		(2,0)
MgD$^-$			
	0.89		(0,0)
		1049	
	1.02		(1,0)

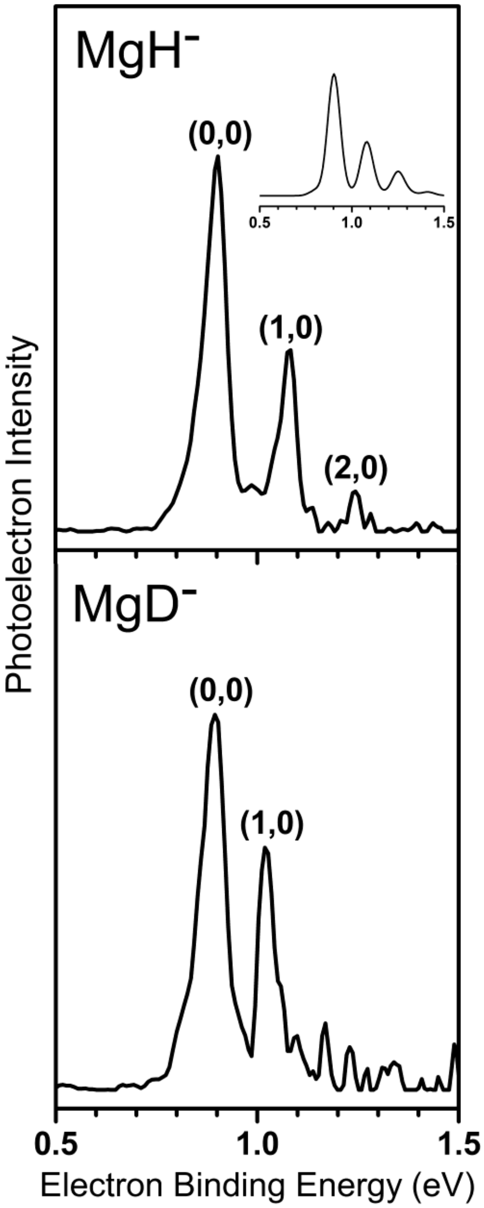

Figure III.3: Photoelectron spectra of MgH^{-} and MgD^{-} anions, both measured with 2.33 eV photons. The Franck–Condon fit for MgH^{-} is shown as an inset above the MgH^{-} spectrum.

The first measurement of the photodetachment spectrum of MgH^{-} was conducted by Rackwitz and coworkers[16], who recorded the total photodetachment cross section versus photon energy in discrete steps. In threshold photodetachment spectra, such as this, one observes inflection points rather than line spectra as are seen in fixed-frequency photoelectron spectra. Based on their data, these investigators reported the electron affinity of MgH to be 1.05 eV, as compared with 0.90 eV in our work. Inspection of their published threshold photodetachment spectrum, however, shows that the first inflection point actually occurs at 0.9 eV. Thus, the two experiments are in good agreement.

The first calculation of the electron affinity of MgH was performed by Gaines and Page, who utilized semi-empirical methods.[13] These investigators found its value to be 1.08 eV. More recently, the EA for MgH was computed at a higher level of theory by Eizaguirre *et al.*[11], who reported a value of 0.83 eV. In the present study, our computations at both the B3LYP/aug-cc-pVQZ and the CCDS(T)/aug-cc-pVQZ level of theory found the EA value of MgH to be 0.86 eV, as compared to our experimentally-determined value of 0.90 ± 0.05 eV.

III.1.4. CONCLUSION

We have prepared the diatomic anions, MgH^- and MgD^- in a pulsed arc cluster ionization source and measured their anion photoelectron spectra using velocity-map imaging, electron energy analysis. The electron affinities of MgH and MgD were determined to be 0.90 ± 0.05 eV and 0.89 ± 0.05 eV, respectively. These findings were supported by *ab initio* calculations at the B3LYP/aug-cc-pVQZ and the CCDS(T)/aug-cc-pVQZ level of theory which found the electron affinity of MgH to be 0.86 eV. Both our experimental and theoretical results were in good agreement with those from previous studies.

ACKNOWLEDGEMENTS

This work was supported by the Air Force Office of Scientific Research through grant numbers, FA9550-11-1-0068 (K.H.B.) and FA9550-11-1-0171 (B.E.). K.B. acknowledges funding support through a BoR-RCS grant.

REFERENCES

1. H. D. Babcock, Astrophys. J. **102**, 154 (1945).

2. J. Tomkin and D. L. Lambert, Astrophys. J. **235**, 925 (1980).

3. A. Zaluska, L. Zaluski and J.O. Stroem-Olsen, Appl. Phys. A **72**,157 (2001).

4. W. J. Balfour and H. M. Cartwright, Astron. Astrophys. Supp. Sec., **26**, 389 (1976).

5. W. J. Balfour and H. M. Cartwright, Can. J. Phys. **53**, 1477 (1975).

6. L. B. Knight and William Weltner, J. Chem. Phys. **54**, 3875 (1971).

7. B. Lemoine, C. Demuynck, J. L. Destombes and P. B. Davies, J. Chem. Phys. **89**, 673 (1988).

8. A. Guntsch, Z. Phys. **93**, 534 (1935).

9. W. D. Slafer and D. J. Benard, Appl. Phys. Lett. **32**, 654 (1978).

10. A. C. H. Chan and E. R. Davidson, J. Chem. Phys. **52**, 4108 (1970).

11. A. Eizaguirre, O. Mó, M. Yáñez and J.-C. Guillemin, Chem. Eur. J.**14**, 10423 (2008).

12. P. G. Wenthold, Int. J. Mass Spectrum. **195/196**, 319 (2000).

13. A. F. Gaines and F. M. Page, Trans. Faraday Soc. **62**, 3086 (1966).

14. J.-M. Mestdagh, P. de Pujo, B. Soep and F. Spiegelman, Chem. Phys. Lett. **471**, 22 (2009).

15. K. Bethge, E. Heinicke and H. Baumann, Phys. Lett. **23**, 542 (1966).

16. R. Rackwitz, D. Feldmann, H. J. Kaiser and H. Heinicke, Z. Naturforsh. **32A**, 595 (1977).

17. R. Middleton, Nucl. Instrum. Methods **141**, 373 (1977).

18. R. J. Hinde, J. Phys. Chem. A **104**, 7580 (2000).

19. S. P. A. Sauer, T. Enevoldsen and J. Oddershede, J. Chem. Phys. **98**, 9748 (1993).

20. H. W. Sarkas, J. H. Hendricks, S. T. Arnold, V. L. Slager and K. H. Bowen, J. Chem. Phys., **100**, 1884 (1994).

21. A. E. Stevens, C.S. Feigerle and W.C. Lineberger, J. Chem. Phys. **78**, 5420 (1983).

22. A. E. S. Miller, C.S. Feigerle and W.C. Lineberger, J. Chem. Phys. **87**, 1549 (1987).

23. C. B. Freidhoff, J. T. Snodgrass, J. V. Coe, K. M. McHugh, and K. H. Bowen, J. Chem. Phys., **84**, 1051 (1986).

24. K. M. Ervin and W. C. Lineberger, J. Chem. Phys., **122**, 194303 (2005).

25. J. V. Coe, J. T. Snodgrass, C. B. Freidhoff, K. M. McHugh and K. H. Bowen, J. Chem. Phys. **87**, 4302 (1987).

26. A. T. J. B. Eppink and D. H. Parker, Rev. Sci. Instrum. **68**, 3477 (1997).

27. R. Mabbs, E. Surber and A. Sanov, Analyst **128**, 765 (2003).

28. V. Dribinski, A. Ossadtchi, V. A. Mandelshtam and H. Reisler, Rev. Sci. Instrum. **73**, 2634 (2002).

29. X. Li, A. Grubisic, S. T. Stokes, J. Cordes, G. F. Gantefoer, K. H. Bowen, B. Kiran, M. Willis, P. Jena, R. Burgert, and H. Schnoeckel, Science **315**, 356 (2007).

30. M. J. Frisch, *et al*. Gaussian 09, Revision A.1; Gaussian, Inc. Wallingford, CT, 2009.

31. K.M. Ervin, J. Ho and W.C. Lineberger, J. Phys. Chem. **92**, 5405 (1988).

III.2. The Alanate Anion, AlH_4^-: Photoelectron Spectrum and Computations

J. D. Graham,[1] A. M. Buytendyk,[1] X. Zhang,[1] E. L. Collins,[1] B. Kiran,[2] G. Gantefoer,[3]
B. W. Eichhorn,[4] G. L. Gutsev,[5*] S. Behera, [6] P. Jena,[6*] and K. H. Bowen[1*]

[1] *Department of Chemistry, Johns Hopkins University, Baltimore, Maryland 21218, USA*
[2] *Department of Chemistry, McNeese State University. Lake Charles, LA 70609, USA*
[3] *Department of Physics, Konstanz University, 78457 Konstanz, Germany*
[4] *Department of Chemistry, University of Maryland, College Park, MD, 20742 USA*
[5] *Department of Physics, Florida A&M University, Tallahassee, FL, 32307, USA*
[6] *Department of Physics, Virginia Commonwealth University, Richmond, VA 23284, USA*

ABSTRACT

The alanate anion, AlH_4^-, was generated in the gas phase using a pulsed arc cluster ionization source. Its photoelectron spectrum was then measured with 193 nm photons. The spectrum consists of a broad feature, spanning electron binding energies from 3.8 eV to over 5.3 eV. This band reflects the photodetachment transitions between the ground state of the AlH_4^- anion and the ground state of its thermodynamically unstable neutral counterpart, AlH_4. The vertical detachment energy (VDE) of AlH_4^- was measured to be 4.4 eV. Additionally, VDE values were also computed in a comprehensive theoretical study and compared both with the previously computed value and with our experimentally-determined value.

III.2.1. INTRODUCTION

The AlH_4^- anion is perhaps the best known aluminum hydride in chemistry. The AlH_4^- anion is the anionic moiety in alkali alanate salts, such as $LiAlH_4$ and $NaAlH_4$, these being powerful reducing agents.[1] AlH_4^- is also of interest as a candidate for hydrogen storage, e.g., as in $Mg(AlH_4)_2$, owing to its high hydrogen gravimetric density.

The AlH_4^- anion has been observed and studied in cryogenic matrices[2-5] and has been found to be relatively unreactive during gas phase thermochemical measurements.[6] Calculations by Boldyrev and co-workers[7,8] showed that the high stability of this anion arises from its excess electron occupying a bonding molecular orbital spread over each of its Al-H bonds. They also found the vertical detachment energy (VDE) of this anion to be 4.83 eV, and that AlH_4^- is stable against dissociation into $AlH_2^- + H_2$ and into $AlH_3 + H^-$ by 3.0 eV and 3.3 eV, respectively. Additionally, other computations have found neutral AlH_4 to be unstable, dissociating along a barrier-free potential surface into AlH_2 and H_2.[9]

Although we had previously observed the AlH_4^- anion along with other aluminum hydride anionic species in mass spectra[10], here we report the measurement of its anion photoelectron spectrum for the first time. Additionally, we have expanded on previous theoretical work by calculating the vertical detachment energy of the AlH_4^- anion at various higher levels of theory. We also computed the energetic differences between AlH_4^- and its decomposition products, AlH_2^- and H_2 and between the unbound neutral AlH_4 and its decay products, AlH_2 and H_2.

III.2.2. EXPERIMENTAL METHODS

AlH_4^- ions were generated in the gas phase using a pulsed arc cluster ionization source (PACIS). A detailed description of the PACIS can be found elsewhere[11], but a brief overview is given here. During operation, a pulsed valve backed by 200 psi of UHP hydrogen is opened for about 200 microseconds and fills a region between a copper anode and grounded aluminum cathode. A 30 microsecond long, 100 V pulse is applied to the copper anode that discharges through the hydrogen gas and subsequently vaporizes the aluminum cathode. The combination of free atomic hydrogen and vaporized aluminum is entrained with the remaining molecular hydrogen and carried along a 20 cm flow tube where it reacts, cools, and forms AlH_4^- along with other aluminum hydrides. AlH_4^- is then extracted and mass-selected before photodetachment.

Anion photoelectron spectroscopy is conducted by crossing a beam of mass-selected negative ions with a fixed-frequency photon beam and energy-analyzing the resultant photodetached electrons. The photodetachment process is governed by the energy-conserving relationship, hv = EBE + EKE, where hv is the photon energy, EBE is the electron binding energy, and EKE is the electron kinetic energy. Our instrument consists of a PACIS, a time-of-flight mass spectrometer, a magnetic bottle electron energy analyzer, and an excimer laser. The ArF excimer laser detaches photoelectrons with 193 nm (6.42 eV) photons. The magnetic bottle has an energy resolution of better than 50 meV at EKE = 1 eV and photoelectron spectra are calibrated against well-known transitions of atomic Cu^-.

III.2.3. COMPUTATIONAL METHODS

Our calculations of AlH_4, AlH_4^-, AlH_2, AlH_2^- and H_2 have been carried out using a number of different methods which include density functional theory (DFT), hybrid Hartree-Fock-DFT, and post-HF methods combined with basis sets whose quality ranges from triple-ξ to penta-ξ. The methods applied are the BPW91 (DFT),[12,13] B3LYP[14,15] and M06[16] (HFDFT), second-order Moller-Plesset perturbation theory (MP2),[17] coupled-cluster with single and doubles (CCSD) and non-iterative triples CCSD(T),[18] and the outer valence Green's function (OVGF).[19-21] The OVGF computations were performed with the geometry optimized at the B3LYP level of theory. The basis sets used for Al and H atoms are 6-311+*G**, 6-311++*G*(*3df,3pd*)),[22] cc-pVQZ, cc-pV5Z, and aug-cc-pV5Z,[23,24] as implemented in Gaussian 03[25] and 09[26] codes.

III.2.4. EXPERIMENTAL RESULTS

The photoelectron spectrum of AlH_4^- is presented in Figure III.4. The spectrum consists of a broad feature, spanning electron binding energies from 3.8 eV to over 5.3 eV. This feature corresponds to transitions between the ground electronic state of the anion and the ground state of the thermodynamically unstable neutral species. The vertical detachment energy (VDE) of AlH_4^- was measured to be 4.4 eV. Since 6.42 eV photons are energetic enough to dissociate AlH_4^- into $AlH_2^- + H_2$ or $AlH_3 + H^-$, it is possible that these products could have also been formed and subsequently photodetached in the ion-photon interaction region of our spectrometer. Nevertheless, we saw no evidence for either AlH_2^- at EBE = 1.5 eV (its VDE value) or for H^- at EBE = 0.75 eV (its electron affinity value).

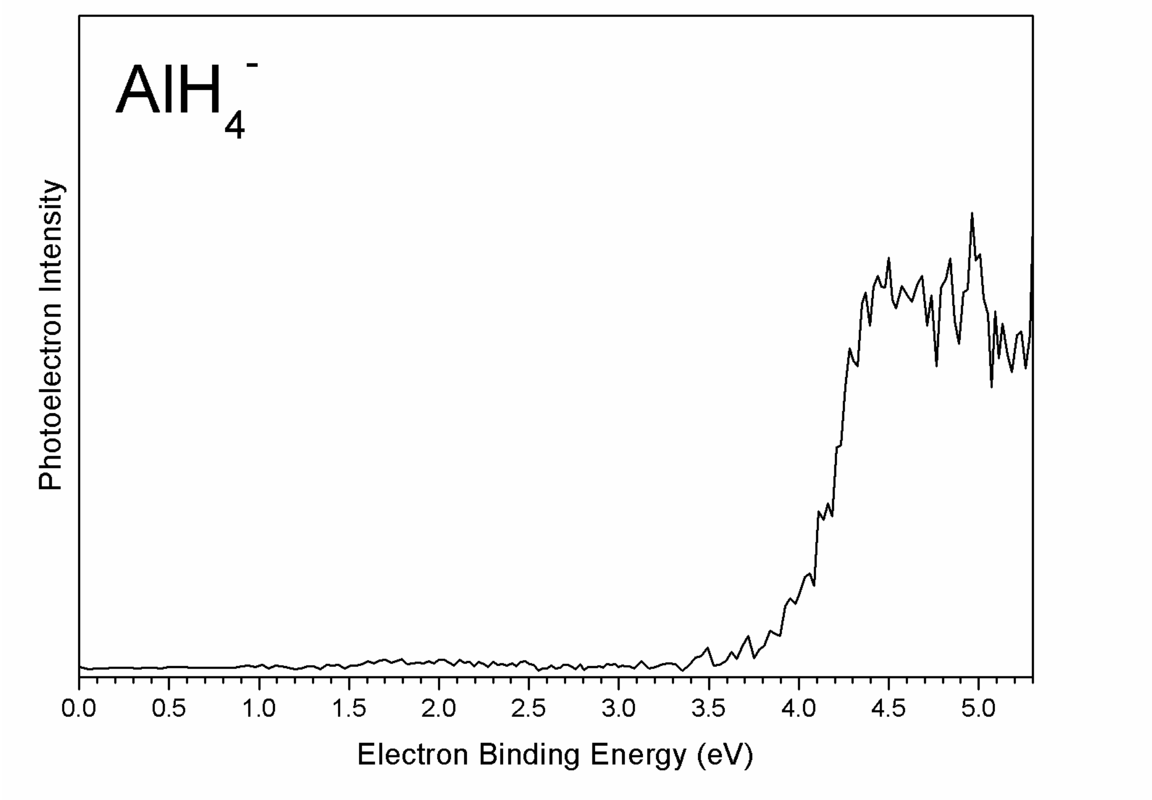

Figure III.4: The photoelectron spectrum of the AlH_4^- anion.

III.2.5. COMPUTATIONAL RESULTS

We began our optimizations without imposing symmetry constraints, followed by re-optimization of the structures obtained within the actual symmetry of their nuclei. All optimizations have been followed by harmonic vibrational frequency calculations in order to confirm that the structure obtained corresponds to a minimum on the potential energy surface. The convergence threshold in total energy and force was $1\text{x}10^{-8}$ eV and $1\text{x}10^{-3}$ eV/Å, respectively.

The AlH_4^- anion geometry converged to a geometry of T_d symmetry and its ground state is $^1A_1$. Figure III.5 (a) shows the geometrical structure of the AlH_4^- ground state optimized at the B3LYP/6-311++*G*(3*df,3pd*) level, along with the charges on its atoms obtained from the Natural Atomic Orbital (NAO)[27] population analysis. In the AlH_4^- anion, the charge of the central atom is +0.63*e*, which means that the extra electron is delocalized over hydrogen atoms, each carrying a negative charge of –0.41*e*. The AlH_4^- anion satisfies the superhalogen[28,29] formula, MX_{k+1} for monovalent ligands, *X*, where *k* is the maximal formal valence of the central atom, *M*. This is because the maximal formal valence of an aluminum atom with the electronic configuration of $[Ne]3s^23p^1$ is three. Formally, the extra electron in AlH_4^- serves as the fourth valence electron of aluminum, which forms single bonds of the 30%(Al) + 70%(H) type with each hydrogen atom in AlH_4^-. The vertical detachment energy (VDE) of the anion is computed at the anion equilibrium geometry according to the following expression,

$$VDE(AlH_4^-) = E(AlH_4 \text{ at anion equilibrium geometry}) - E(AlH_4^- \text{ at equilibrium geometry}) \quad (1)$$

where *E* is the electronic energy. The values obtained from this equation using different methods and basis sets are listed in Table III.2. alongside the value measured from the experimental spectrum.

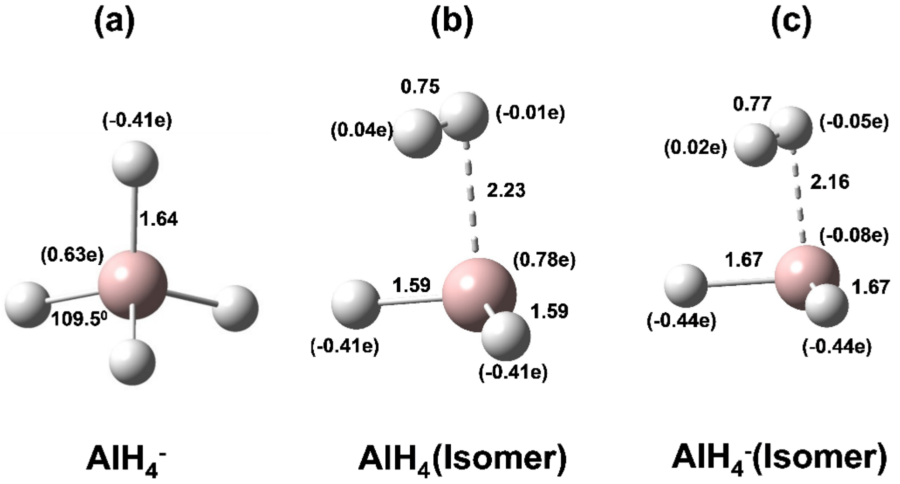

Figure III.5: Geometrical structures of the AlH_4^- ground state (a) and electronically stable states of the neutral (b) and anion (c) isomers as optimized at the B3LYP/6-311++G(3df,3pd) level. Bond lengths are in Å and charges on atoms are in units of electronic charge.

Table III.2: Energetic difference between AlH_4^- anion and the unbound neutral AlH_4 decay products, AlH_2 and H_2, (E_{asym}), vertical electron detachment energy (VDE) of the AlH_4^- anion, interatomic distances and harmonic vibrational frequency of the H – H vibration (ω_e) in the AlH_4 isomer given in Figure (b), and the differences in total electronic (ΔE) energy and total energy (ΔE_{tot}) for the neutral isomer channels (N ISO) $AlH_4 \rightarrow AlH_2 + H_2$ and (A ISO) $AlH_4^- \rightarrow AlH_2^- + H_2$ computed using different methods and basis sets.

Method	Basis set	E_{asym} eV	VDE eV	R(H – H) Å	R(Al – H_2) Å	ω_e(H–H) eV	ΔE eV
BPW91	6-311++*G*(3*df*,3*pd*))	2.97	4.14	0.76	2.21	0.50	ΔE(N ISO) = +0.04 ΔE_{tot}(N ISO) = –0.06 ΔE(A ISO) = +0.08 ΔE_{tot}(A ISO) = –0.04
	cc-pVQZ	2.87	4.14	0.77	2.12	0.49	ΔE(N ISO) = +0.08 ΔE_{tot}(N ISO) = –0.04
	cc-pV5Z	2.89	4.13	0.77	2.12	0.49	ΔE(N ISO) = +0.08 ΔE_{tot}(N ISO) = –0.03
B3LYP	6-311+*G**	3.14	4.69	0.75	2.53	0.53	
	6-311++*G*(3*df*,3*pd*)	3.17	4.69	0.75	2.41	0.52	ΔE(N ISO) = +0.06 ΔE_{tot}(N ISO) = –0.05 ΔE(A ISO) = +0.03 ΔE_{tot}(A ISO) = –0.06
	aug-cc-pV5Z	3.09	4.47	0.75	2.23	0.52	ΔE(N ISO) = +0.07 ΔE_{tot}(N ISO) = –0.04
M06	6-311++*G*(3*df*,3*pd*)	3.11	4.43	0.75	2.29	0.50	
	aug-cc-pV5Z	3.02	4.40	0.76	2.22	0.51	ΔE(N ISO) = +0.19 ΔE_{tot}(N ISO) = –0.16
MP2	6-311+G*	2.59	4.50	0.74	3.06	0.56	
	6-311++*G*(*3df*, *3pd*))	2.84	4.61	0.74	2.48	0.54	
	cc-pVQZ	2.95	4.83	0.75	2.27	0.54	ΔE(N ISO) = +0.09 ΔE_{tot}(N ISO) = –0.02

CCSD	6-311+*G**	2.62	4.39	0.75	3.17	0.51	
	6-311++*G*(3*df*,3*pd*))	2.91	4.52	0.75	2.51	0.50	
CCSD(T)	6-311+*G**	2.63	4.39	0.75	3.14	0.51	
	6-311++*G*(3*df*, 3*pd*))	2.94	4.52	0.75	2.46	0.50	ΔE(N ISO) = +0.04 ΔE_{tot}(N ISO) = –0.05 ΔE(A ISO) = +0.04 ΔE_{tot}(A ISO) = –0.12
OVGF	6-311+*G**		4.61				
	6-311++*G*(3*df*, 3*pd*))		4.74				
Exp.			4.4 [a]			0.547[b]	

[a] This work.

[b] Experimental value of ω_e for the gas-phase H_2 is 0.547 eV (see Ref.[31]) .

It was found previously[3] and confirmed by the results of our computations that the neutral AlH_4 geometry optimization, beginning with the anion T_d geometry, leads to a transition state of C_{2v} symmetry. We performed an extensive search for a stable state of AlH_4 and found an isomer of the $H_2 \otimes AlH_2$ adduct type of C_s symmetry with all real harmonic vibrational frequencies. This AlH_4 isomer is stable with respect to the sum of total electronic energies of both AlH_2 and H_2 and AlH_3 and H (see Figure III.6). This neutral isomer is also shown in Figure III.5 (b) and as is seen from the charges on atoms, the positive charge on the aluminum atom is nearly balanced by the negative charges in the chemically bound hydrogen atoms. The hydrogen atoms in the quasi-molecularly bound H_2 molecule carry negligible charge and bind weakly to the AlH_2 complex through the charge polarization mechanism.[30] This weak interaction is evident from the differences in total electronic energies, ΔE computed according to equation,

$$\Delta E(\text{N ISO}) = E(\text{AlH}_2) + E(\text{H}_2) - E(\text{AlH}_4\ \text{Isomer}) \qquad (2)$$

where N and ISO indicate ΔE is for the neutral AlH_4 isomer. This value is listed in Table 1 and varies between +0.04 eV and +0.19 eV depending on the method and basis set used.

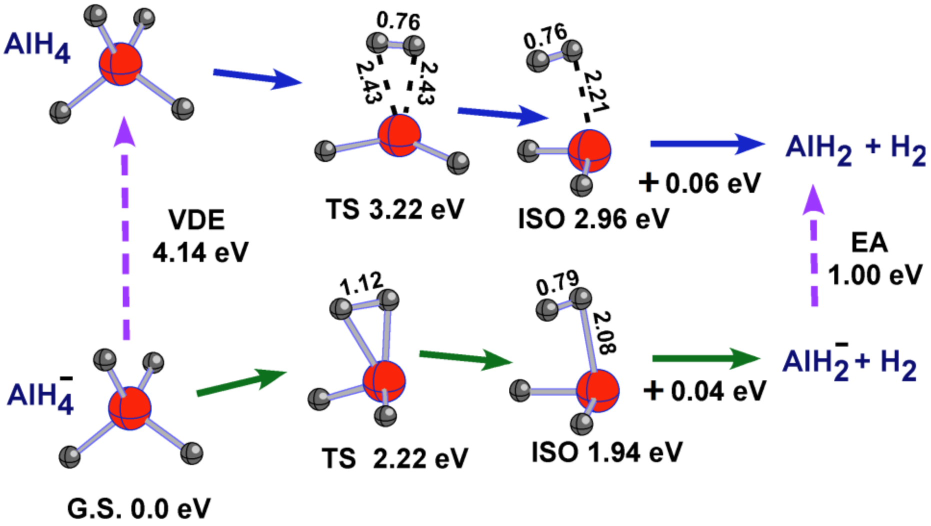

Figure III.6: Decay channels of the AlH_4^- anion (in its ground state) and of the AlH_4 neutral, both computed at the BPW91/6-311++G(3df) level of theory. Ground state is abbreviated G.S., transition state is abbreviated TS and isomer is abbreviated ISO. Bond lengths are in Å.

However, the neutral isomer becomes thermodynamically unstable with respect to the $AlH_4 \rightarrow AlH_2 + H_2$ decay channel when the zero point vibrational energies (ZPVE) are added to the total electronic energies of the AlH_4, AlH_2, and H_2 species. Adding the zero point vibrational energies to the total electronic energies, we compute the differences in total energies for the neutral isomer as:

$$\Delta E_{tot}(\text{N ISO}) = E_{tot}(\text{AlH}_2) + E_{tot}(\text{H}_2) - E_{tot}(\text{AlH}_4\ \text{Isomer}) \qquad (3)$$

where E_{tot} is the sum of the total electronic energy of a given species and the corresponding ZPVE. The ΔE_{tot}(N ISO) values computed according to Eq. (3) are negative (see Table III.2) which means that the neutral isomer is thermodynamically unstable.

As there is no stable neutral AlH_4 species, in place of an adiabatic electron affinity, we define E_{asym} as the energetic difference between AlH_4^- and the unbound neutral AlH_4 decay products, AlH_2 and H_2, as

$$E_{asym} = E_{tot}(AlH_2) + E_{tot}(H_2) - E_{tot}(AlH_4^-) \quad (4)$$

The computed E_{asym} values are listed in Table III.2.

Additionally, a stable anion isomer was found and is shown in Figure III.5 (c). The anion isomer shows similar behavior to the neutral isomer and is weakly bound at the BPW91, B3LYP and CCSD(T) levels with the 6-311++*G*(3*df*,3*pd*) basis. In a similar manner as the neutral isomer, the ΔE value for the anion isomer was computed according to the equation,

$$\Delta E(\text{A ISO}) = E(AlH_2^-) + E(H_2) - E(AlH_4^- \text{ Isomer}) \quad (5)$$

where A and ISO indicate ΔE is for the anionic AlH_4^- isomer. Again, as with the neutral isomer, including zero point vibrational energy to the energy of each component yields,

$$\Delta E_{tot}(\text{A ISO}) = E_{tot}(AlH_2^-) + E_{tot}(H_2) - E_{tot}(AlH_4^- \text{ Isomer}) \quad (6)$$

The computed ΔE_{tot}(A ISO) values are negative which indicates that the anion isomer is thermodynamically unstable. The decay channels for the ground-state AlH_4^- anion calculated at the BPW91/6-311++*G*(3*df*,3*pd*) level are shown in Figure III.6.

III.2.6. DISCUSSION

Using several computational methods belonging to the density functional theory (DFT), hybrid DFT, second-order perturbation theory, and couple-cluster groups, we studied the geometrical and electronic structure of AlH_4 and AlH_4^-. The AlH_4^- anion is thermodynamically stable by 1.98 eV with respect to the to the $AlH_4^- \rightarrow AlH_2^- + H_2$ decay channel according to our BPW91/6-111++*G*(*3df,3pd*) computations. On the contrary, the neutral AlH_4 is thermodynamically unstable and dissociates to AlH_2 and H_2. The temporary AlH_4 radical presents a case of when a species is electronically stable within the Born-Oppenheimer approximation but is unstable with respect to nuclear motions. The energy of the vertical detachment of an extra electron strongly depends on the method and basis used and is enclosed in the range from 4.13 eV to 4.83 eV according to the results of our computations by different methods. The broad width of the photoelectron spectrum of the AlH_4^- anion is consistent with the instability of neutral AlH_4. Our experimental VDE value of 4.4 eV for the AlH_4^- anion is within the range of our theoretical estimates. The closest to experimental values are obtained at the B3LYP/aug-cc-pV5Z (4.47 eV), M06/aug-cc-pV5Z (4.40 eV), CCSD/6-311+*G** (4.39 eV), and CCSD(T)/6-311+*G** (4.39 eV) levels. The values obtained using the BPW91 method are somewhat underestimated, whereas the OVGF values are somewhat overestimated compared to the experimental value. Since agreement between experiment and theory is quite reasonable, one can conclude that the theoretical results are reliable.

ACKNOWLEDGEMENTS

This material is based upon work supported by the Air Force Office of Scientific Research (AFOSR) under Grant No. FA9550-11-1-0068 (K.H.B.). Portions of this research were conducted with high performance computational resources provided by the Louisiana Optical Network Initiative.

REFERENCES

1. Cotton, F. A.; Wilkinson, G. *Advanced Inorganic Chemistry*; Interscience: New York, 1996.

2. Pullumbi, P.; Bouteiller, Y.; Manceron, L. The Vibrational Spectrum of Isolated AlH_4^-: An Infrared Matrix Isolation and A*b Initio* Study. *J. Chem. Phys.* **1994**, 101, 3610-3617.

3. Andrews, L.; Wang, X. Infrared Spectra of Dialanes in Solid Hydrogen. *J. Phys. Chem. A*, **2004**, 108, 4202–4210.

4. Wang, X.; Andrews, L.; Tam, S.; DeRose, M.; Fajardo, M. Infrared Spectra of Aluminum Hydrides in Solid Hydrogen: Al_2H_4 and Al_2H_6. *J. Am. Chem. Soc.*, **2003**, 125, 9218–9228.

5. Andrews, L.; Wang, X. The Infrared Spectrum of Al_2H_6 in Solid Hydrogen. *Science*, **2003**, 299, 2049-2052.

6. Goebbert, D.; Hernandez, H.; Francisco, J.; Wenthold, P. The Binding Energy and Bonding in Dialane. *J. Am. Chem. Soc.*, **2005**, 127, 11684–11689.

7. Boldyrev A. I.; Simons, J. Vertical and Adiabatical Ionization Potentials of MH^-_{K+1} Anions. *Ab Initio* Study of the Structure and Stability of Hypervalent MH_{k+1} Molecules. *J. Chem. Phys.*, **1993**, 99, 4628-4637.

8. Boldyrev, A. I.; von Niessen, W. The First Ionization Potentials of Some MH_{k+1}^- and $M_2H_{2k+1}^-$ Anions Calculated by a Green's Function Method. *Chem. Phys.*, **1991**, 155, 71-78.

9. Wong, S.; Li, W.; Paddon-Row, M. On the Structure and Stability of the AlH_4 Radical and its Potential Energy Surface for Rearrangement and Dissociation: An Ab Initio MO Study. *J. Mol. Struc-Theochem.* **1991**, 226, 285-301.

10. Zhang, X.; Wang, H.; Collins, E.; Lim, A.; Ganteför, G.; Kiran, B.; Schnöckel H.; Eichorn, B.; Bowen, K. Photoelectron Spectroscopy of the Aluminum Hydride Anions: AlH_2^-, AlH_3^-, $Al_2H_6^-$, $Al_3H_9^-$, and $Al_4H_{12}^-$. *J. Chem. Phys.* **2013**, 138, 124303.

11. Cha, G.; Ganteför G.; Eberhardt, W. New Experimental Setup for Photoelectron Spectroscopy on Cluster Anions. *Rev. Sci. Instrum.* **1992**, 63, 5661-5666.

12. Becke, A. D. Density-functional Exchange-energy Approximation with Correct Asymptotic Behavior. *Phys. Rev. A* **1988**, 38, 3098-3100.

13. Perdew, J. P.; Wang, Y. Accurate and Simple Analytic Representation of the Electron-gas Correlation Energy. *Phys. Rev. B* 1922, 45, 13244-13249.

14. Becke, A. D. Density-functional Thermochemistry. III. The Role of Exact Exchange. *J. Chem. Phys.* **1993**, 97, 5648-5652.

15. Lee, C.; Yang, W.; Parr, R. G. Development of the Colle-Salvetti Correlation-energy Formula into a Functional of the Electron Density. *Phys. Rev. B* **1988**, 37, 785-789.

16. Zhao, Y.; Truhlar, D. G. Density Functional for Spectroscopy: No Long-Range Self-Interaction Error, Good Performance for Rydberg and Charge-Transfer States, and Better Performance on Average than B3LYP for Ground States. *J. Phys. Chem. A* **2006**, 110, 13126-13130.

17. Head-Gordon, M.; Pople, J. A.; Frisch, M. MP2 Energy Evaluation by Direct Methods. J. *Chem. Phys. Lett.* **1998**, 153, 503-506.

18. Bartlett, R. J.; Musial, M. Coupled-cluster Theory in Quantum Chemistry. *Rev. Mod. Phys.* **2007**, 79, 291-352.

19. Cederbaum, L. S. One-body Green's Function for Atoms and Molecules: Theory and Application. *J. Phys. B*, **1975**, 8, 290-303.

20. Ortiz, J. V. Partial Third-order Quasiparticle Theory: Comparisons for Closed-shell Ionization Energies and an Application to the Borazine Photoelectron Spectrum. *J. Chem. Phys.* **1996**, 104, 7599-7605.

21. Zakrzewski, V. G.; von Niessen, W. Vectorizable Algorithm for Green Function and Many-body Perturbation Methods. *J. Comp. Chem.* **1993**, 14, 13-18.

22. Krishnan, R.; Binkley, J. S.; Seeger, R.; Pople, J. A. Self-consistent Molecular Orbital Methods. XX. A Basis Set for Correlated Wave Functions. *J. Chem. Phys.* **1980**, 72, 650-654.

23. Woon, D. E.; Dunning Jr., T. H. Gaussian Basis Sets for Use in Correlated Molecular Calculations. III. The Atoms Aluminum Through Argon. *J. Chem. Phys.* **1993**, 98, 1358-1371.

24. Dunning Jr., T. H. Gaussian Basis Sets for Use in Correlated Molecular Calculations. I. The Atoms Boron Through Neon and Hydrogen. *J. Chem. Phys.* **1989**, 90, 1007-1023.

25. Frisch, M. J.; Trucks, G. W.; Schlegel, H. B.; Scuseria, G. E.; Robb, M. A.; Cheeseman, J. R.; Montgomery, Jr., J. A.; Vreven, T.; Kudin, K. N.; Burant, J. C.; et al. *Gaussian 03*, rev. C.02; Gaussian, Inc.: Wallingford CT, 2004.

26. Frisch, M. J.; Trucks, G. W.; Schlegel, H. B.; Scuseria, G. E.; Robb, M. A.; Cheeseman, J. R.; Scalmani, G.; Barone, V.; Mennucci, B.; Petersson, G. A.; et al. *Gaussian 09*, rev. A.2. ed.; Gaussian Inc.: Wallingford, CT, 2009.

27. Reed, A. E.; Curtiss, L. A.; Weinhold, F. Intermolecular Interactions from a Natural Bond Orbital, Donor-acceptor Viewpoint. *Chem. Rev.* **1988**, 88, 899-926.

28. Gustev, G. L.; Boldyrev, A. I. DVM-Xα Calculations on the Ionization Potentials of MX_{k+1}^{-} Complex Anions and the Electron Affinities of MX_{k+1} "Superhalogens". *Chem. Phys.* **1981**, 56, 277-283.

29. Gustev, G. L.; Boldyrev, A. I. The Theoretical Investigation of the Electron Affinity of Chemical Compounds. *Adv. Chem. Phys.* **1985**, 61, 169.

30. Niu, J.; Rao, B.; Jena, P. Binding of Hydrogen Molecules by a Transition-metal Ion. *Phys. Rev. Lett.* **1992**, 68, 2277-2280.

31. Hotop, H.; Lineberger, W. C. Binding Energies in Atomic Negative Ions: II. *J. Phys. Chem. Ref. Data.* **1985**, 14, 731-750.

Chapter IV: Aromatic Heterocyclic Organic Molecules

In the effort to reduce greenhouse gases from the Earth's atmosphere, metal-organic-frameworks (MOFs) have been studied and shown to capture and separate gas molecules, such as CO_2, CO and O_2. It is unclear, however, the nature of the molecular interactions between the MOF and these gas molecule. Synthetic metal porphyrins mimic many of the chemical and physical properties of their biological counterparts (e.g. heme proteins), and can be found as building blocks in some MOFs. Here, the electron affinity of tetraphenyl porphyrins (with metal centers, Fe, Ni, and Mn) and quinoline, another linker-ligand found in MOFs, were measured using anion photoelectron spectroscopy.

IV.1. Photoelectron Spectrum of a Polycyclic Aromatic Nitrogen Heterocyclic Anion: Quinoline$^-$

Allyson M. Buytendyk[a], Yi Wang[a], Jacob D. Graham[a], Anil K. Kandalam[b*], Boggavarapu Kiran[c*], and Kit H. Bowen[a*]

[a]*Department of Chemistry, Johns Hopkins University, Baltimore, Maryland 21218, USA*
[b]*Department of Physics, West Chester University of Pennsylvania, West Chester, Pennsylvania 19383, USA*
[c]*Department of Chemistry, McNeese State University, Lake Charles, LA 70609, USA*

ABSTRACT

We report a joint photoelectron spectroscopic and theoretical study on the molecular anion, quinoline$^-$. Analysis of the vibrationally resolved photoelectron spectrum found the adiabatic electron affinity, $EA_a(C_9H_7N)$, to be 0.16 ± 0.05 eV. These findings were supported by density functional theory calculations. Our experimental and computational results demonstrate the unusual electrophilicity for a polycyclic aromatic heterocycle.

IV.1.1. INTRODUCTION

Typically, cyclic aromatic hydrocarbons such as benzene and naphthalene as well as their heteroaromatic analog structures do not support a valence bound anion. Quinoline is a polycyclic aromatic nitrogen heterocycle that is structurally equivalent and π-isoelectronic to naphthalene, where a nitrogen atom replaces the position 1 CH group on the hydrocarbon. Semi-empirical calculations predicted a small *positive* electron affinity for quinoline almost fifty years ago[1]. The neutral quinoline molecule has been extensively studied computationally[2-9] and experimentally in the gas phase by measuring the dielectric constant to determine the dipole moment[10], photoionization[11-13], UV-Vis absorbance[14-16], microwave[17] and infrared[18] spectroscopy. Quinoline has also general astrophysical interest.[19-21] Nevertheless, few experimental negative ion gas phase studies exist. The compound negative ion resonance (CNIR)[22] of quinoline was reported and the gas phase lifetime[23] of the negative parent ion was determined, however, no experimentally measured electron affinity value for quinoline has been reported in the literature.

Here, we present the vibrationally-resolved anion photoelectron spectrum of quinoline$^-$ anion. From the spectrum we determined the adiabatic electron affinity to be 0.16 ± 0.05eV. This assignment is supported by our theoretical calculations and computationally simulated spectrum. The active vibrational frequencies observed compare favorably with previous experimentally measured vibrational modes of quinoline.

IV.1.2. METHODS

IV.1.2.1 Experimental

Anion photoelectron spectroscopy is conducted by crossing a mass-selected beam of negative ions with a fixed-frequency photon beam and energy-analyzing the resultant photodetached electrons. The photodetachment process is governed by the relationship hν = EBE + EKE, where hν is the photon energy, EBE is the electron binding energy, i.e., the transition energy between the anion and a particular vibronic state of its neutral counterpart, and EKE is the electron kinetic energy. Negative ions of quinoline were formed in a biased (-500 V) supersonic expansion nozzle-ion source, where the quinoline sample was placed in a stagnation chamber, heated to 70 °C, and coexpanded with ~30 psig of argon gas through a 23 μm orifice into $\sim 10^{-4}$ Torr vacuum. Negative ions were formed by injecting low energy electrons from a more negatively biased, thoriated-iridium filament into the expanding jet, where a microplasma was formed in the presence of a weak external magnetic field. These anions were then extracted, collimated, and transferred into the flight tube of a 90° magnetic sector mass spectrometer with a mass resolution of ~400. The mass-selected anions of interest were then crossed with the intracavity laser beam of an argon ion laser, and the photodetached electrons were energy-analyzed in a hemispherical electron energy analyzer having a resolution of ~20 meV. The photoelectron spectrum reported here was recorded with 2.540 eV photons (488 nm), and it was calibrated against the photoelectron spectrum of the O^- anion.[24] It was also measured at lower resolution using our pulsed photoelectron magnetic bottle instrument.

IV.1.2.2 Computational

Density functional theory (DFT) calculations of quinoline neutral and anion were performed with the Gaussian09[25] software package. Geometry optimizations, energy calculations and frequency analysis were all performed with the unrestricted wb97xd[26] functional and aug-cc-pVTZ[27-28] basis set. The highest occupied molecular orbital of the relaxed anion was generated in GaussView.[29] A simulated photoelectron spectrum was generated using the Franck-Condon method as implemented[30] in Gaussian09 using the default parameters which includes a convolution of the spectrum with Gaussian distributions with a 135 cm^{-1} half-width at half-maximum.

IV.1.3. RESULTS AND DISCUSSION

The photoelectron spectrum of quinoline anion, presented in Figure IV.1a, exhibits a vibrationally resolved profile. The observed transitions are centered at EBE 0.16 eV (peak **A**), 0.23 eV (peak **B**), 0.33 eV (peak **C**), and 0.52 eV (peak **D**). The lowest EBE transition in the spectrum is its origin-containing transition, i.e., the $\nu'=0 \leftarrow \nu''=0$ transition, and it defines the adiabatic electron affinity. Thus, $EA_a(C_9H_7N)$ was determined to be 0.16 eV ± 0.05 eV (Peak **A)**. Our electronic structure calculations, including the zero-point energy, found quinoline to support a bound valence anion with an EA of 0.19 eV, which is in very good agreement with our experimentally measured value and the previous calculated semi-empirical value of 0.2eV.[2] Since the electron is added to a closed shell molecule, the electron affinity is expected to be small. There is scant evidence of vibrational hot bands in the spectrum, possibly because of anion autodetachment. The optimized geometries for

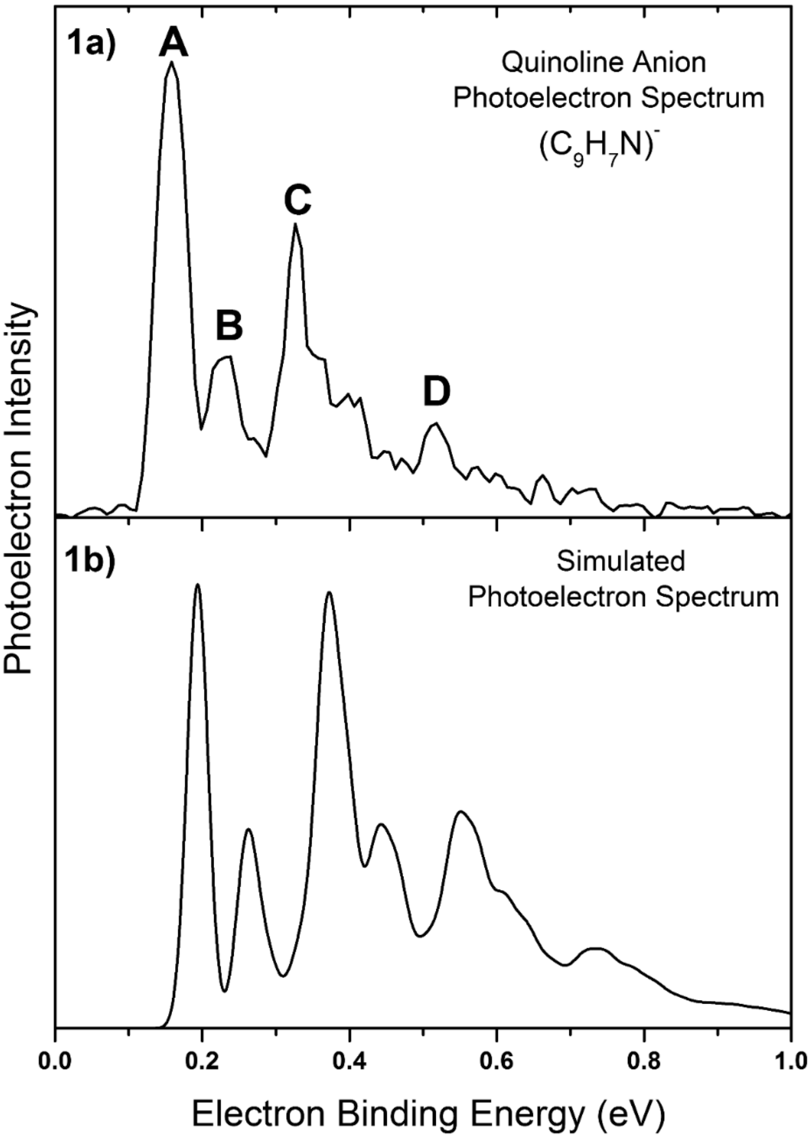

Figure IV.1: a) The measured photoelectron spectrum of the quinoline$^-$ anion recorded using 2.540 eV photons. b) The calculated Franck-Condon simulated photoelectron spectrum.

both anion and neutral quinoline were calculated and found to be planar with very similar bond lengths between the structures (Figure IV.2a). The highest occupied molecular orbital (HOMO) structure for the quinoline anion is shown in Figure IV.2b, where the excess electron is delocalized in the π^* anti-bonding orbital. A computationally simulated photoelectron spectrum was generated and is also shown in Figure IV.1b. The profile of the calculated spectrum matches well compared to the experimentally measured photoelectron spectrum.

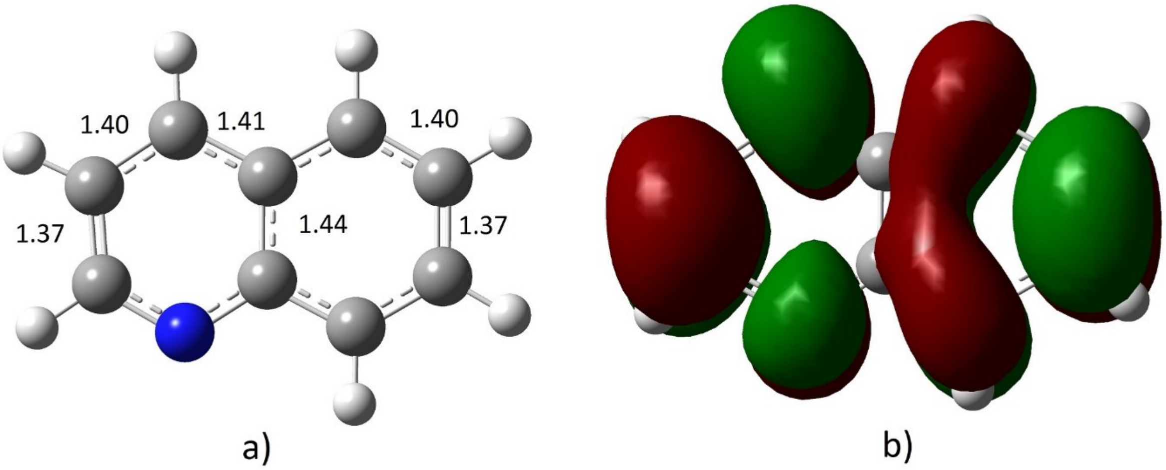

Figure IV.2: a) Optimized (wb97xd/aug-cc-pVTZ) structure of the quinoline$^-$ anion along with the critical bond lengths (Å). b) The highest occupied molecular orbital (HOMO) of the ground state of the anion.

Since quinoline is a planar species belonging to the C_s point group, there are 45 vibrational modes that can be classified as even or odd, 31A′ and 14A″, respectively. The A′ modes will have the greatest Franck-Condon overlap and be active in a photoelectron spectrum. The vibrational frequencies from Figure 1a were measured as the energy spacing between peak centers in the spectrum and are presented in Table 1. Previous IR studies were considered to identify and assign the vibrational modes.[18] The vibrational frequency 565cm^{-1} (spacing between **A** and **B**) is assigned as vibrational mode ν_{29}, an in-plane ring distortion. The adjacent vibrational frequency (between **A** and **C**) at 1371 cm^{-1} is assigned as the vibrational modes ν_{14} and ν_{15} a C-C bond stretch. The spacing between **A** and **D** is 2904 cm^{-1} which corresponds to the C-H vibrational modes ν_{1-7}. The calculated vibrational frequencies are close to the experimentally measured vibrational modes which is expected since the calculated simulated spectrum of quinoline is very similar to the experimentally measured spectrum (Table IV.1).

Table IV.1: Transition assignments for the photoelectron spectrum of quinoline compared with calculations from this study[a] and previously reported literature values

Experimental (this work)					Calculated (this work)		Reported values (from literature)	
Peak Location		Vibrational Spacing			Peak Location	Vibrational Mode	Experimental Vibrational Spacing[b]	Calculated Peak Location[c]
	eV	Δ	eV	cm^{-1}	(eV)	cm^{-1}	cm^{-1}	eV
A	0.16				0.19			0.20
B	0.23	**B-A**	0.07	565	0.26	532, 535	522 (ν_{29})	
C	0.33	**C-A**	0.17	1371	0.37	1371	1392 (ν_{14}), 1371(ν_{15})	
D	0.52	**D-A**	0.36	2904	0.55	3161	3086(ν_1), 3056(ν_2), 3036(ν_3), 3014(ν_4), 3004(ν_5), 2979(ν_7)	

[a] Uncertainties are ± 0.05 eV or less.
[b] From ref [18].
[c] From ref [2].

IV.1.4. SUMMARY

The molecule quinoline, displays a greater electrophilicty than its analog, naphthalene. Quinoline anion was formed by injecting low energy electrons into a supersonic expansion of the molecule seeded in argon and the anion photoelectron spectrum was recorded. A small but positive electron affinity of 0.16 eV was experimentally measured, indicating that quinoline supports a valence bound anion. Density functional theory calculations at the wb97xd /aug-cc-pVTZ level of theory found the electron affinity to be 0.19 eV. Both our experimental and theoretical results were in good agreement with those from previous studies.

ACKNOWLEDGEMENTS

This contribution is in honor of Prof. Dr. John P. Maier. We acknowledge a helpful discussion with G. B. Ellison. This work was supported by the US National Science Foundation under Grant No. CHE-1360692 (KHB).

REFERENCES

1. T. L. Kuni and H. Kuroda, Theoret. Chim. Acta (Berl.) **11**, 97 (1968).

2. J. M. Younkin, L. J. Smith and R. N. Compton, Theoret. Chim. Acta (Berl.) **41**, 157 (1976).

3. A. E. Ozel, Y. Buyukmurat and S. Akyuz, J. Mol. Struct. **565-566**, 455 (2001).

4. E. E. Ebenso, M. M. Kabanda, T. Arslan, M. Saracoglu, f. Kandemirli, L. C. Murulana, A. K. Singh, S. K. Shukla, B. Hammouti, K. F. Khaled, M. A. Quraishi, I. B. Obot and N. O. Eddy, Int. J. Electrochem. Sci. **7,** 5643 (2012).

5. L. Goodman and R. W. Harrell, J. Chem. Phys. **30,** 1131 (1959).

6. G. Favini, I. Vandoni and M. Simoneta, Theoret. Chim. Acta. (Berl.) **3**, 45 (1965).

7. K. Nishimoto, Theoret. Chim. Acta. (Berl.) **10**, 65 (1968).

8. R. D. Brown and B. A. W. Coller, Theoret. Chem. Acta. (Berl.) **7**, 259 (1967).

9. B. Tinland, Theoret. Chim. Acta. (Berl.) **8**, 361(1967).

10. A. D. Buckingham, J. Y. H. Chau, H. C. Freeman, R. J. W. Le Fevre, D. A. A. S. N. Rao and J. Tardif, J. Chem. Soc. 1405-1411 (1956).

11. A. J. Yencha and M. A. ElSayed, J. Chem. Phys. **48**, 3469 (1968).

12. F. Brogli, E. Heilbronner and T. Kobayashi, Helv. Chim. Acta. **55,** 274 (1972).

13. W. Schafer and A. Schweig, Tetrahedron Lett. **39**, 3743 (1973).

14. J. P. Byrne and I. G. Ross, Austral. J. Chem. **24**, 1107 (1971).

15. N. Mataga, Y. Kaigu and M. Koizumi, Bull. Chem. Soc. Japan, **29**, 373(1956).

16. J. E.Purvis, J Chem. Soc. Trans. **97**,1035 (1910).

17. Z. Kisiel, O. Desyatnyk, L. Pszczolkowski, S. B. Charnley and P. Ehrenfreund, J. Mol. Spectrosc. **217**, 115 (2003).

18. S. C. Wait and J. C. McNerney, J. Mol. Spectrosc. **34**, 56 (1970).

19. P. G. Stoks and A. W. Schwartz, Geochim. Cosmochim. Ac. **46**, 309 (1982).

20. S. B. Charnley, Y.-J. Kuan, H.-C. Huang, O. Botta, H. M. Butner, N. Cox, D. Despois, P. Ehrenfreund, Z. Kisiel, Y.-Y. Lee, A. J. Markwick, Z. Peeters and S. D. Rodgers. Adv. Space Res. **36**, 137 (2005).

21. J. E. Elsila, M. R. Hammond, M. P. Bernstein, S. A. Sandford and R. N. Zare, Meteorit. Planet. Sci. **41**, 785 (2006).

22. M. N. Pisanias, L. G. Christophorous and J. G. Carter, Chem. Phys. Lett. **13**, 433 (1972).

23. A. Hadjiantonious, L. G. Christophorou and J. G. Carter, J. Chem. Soc., Faraday Trans. 2, **69**, 1704 (1973).

24. A. Joiner, R. H. Mohr and J. N. Yukich, Phys. Rev. A. **83**, 035401 (2011).

25. Gaussian 09, Revision A.2, M. J. Frisch, G. W. Trucks, H. B. Schlegel, G. E. Scuseria, M. A. Robb, J. R. Cheeseman, G. Scalmani, V. Barone, B. Mennucci, G. A. Petersson, H. Nakatsuji, M. Caricato, X. Li, H. P. Hratchian, A. F. Izmaylov, J. Bloino, G. Zheng, J. L. Sonnenberg, M. Hada, M. Ehara, K. Toyota, R. Fukuda, J. Hasegawa, M. Ishida, T.

Nakajima, Y. Honda, O. Kitao, H. Nakai, T. Vreven, J. A. Montgomery, Jr., J. E. Peralta, F. Ogliaro, M. Bearpark, J. J. Heyd, E. Brothers, K. N. Kudin, V. N. Staroverov, R. Kobayashi, J. Normand, K. Raghavachari, A. Rendell, J. C. Burant, S. S. Iyengar, J. Tomasi, M. Cossi, N. Rega, J. M. Millam, M. Klene, J. E. Knox, J. B. Cross, V. Bakken, C. Adamo, J. Jaramillo, R. Gomperts, R. E. Stratmann, O. Yazyev, A. J. Austin, R. Cammi, C. Pomelli, J. W. Ochterski, R. L. Martin, K. Morokuma, V. G. Zakrzewski, G. A. Voth, P. Salvador, J. J. Dannenberg, S. Dapprich, A. D. Daniels, Ö. Farkas, J. B. Foresman, J. V. Ortiz, J. Cioslowski, and D. J. Fox.

26. J.-D. Chai and M. Head-Gordon, Phys. Chem. Chem. Phys.**10**, 6615 (2008).

27. D. E. Woon and T. H. Dunning, Jr. J. Chem. Phys. **90**, 1007 (1989).

28. D. E. Woon and T. H. Dunning, Jr. J. Chem. Phys. **98**, 1358 (1993).

29. GaussView, Version 5.0, R. Dennington, T. Keith and J. Millam, *Semichem Inc.*, Shawnee Mission, KS, 2009.

30. F. Santoro, A. Lami, R. Improta, J. Bloino and V. Barone, J. Chem. Phys.**128**, 224311 (2008).

IV.2. Parent Anions of Iron, Manganese, and Nickel Tetraphenyl Porphyrins: Photoelectron Spectroscopy and Computations

Allyson M. Buytendyk, Jacob D. Graham, Julian Gould, and Kit H. Bowen

Department of Chemistry, Johns Hopkins University, Baltimore, MD 21218, USA

ABSTRACT

The singly-charged, parent anions of three transition metal, tetraphenyl porphyrins, M(TPP): Fe(TPP), Mn(TPP), and Ni(TPP) were studied by negative ion photoelectron spectroscopy. The observed (vertical) transitions from the ground state anions of these porphyrins to the various electronic states of their neutral counterparts were modeled by density functional theory (DFT) computations. Our experimental and theoretical results were in good agreement.

IV.2.1. INTRODUCTION

Metalloporphyrins are large, often highly symmetric macrocyclic molecules, which play important roles in nature. In heme proteins, iron porphyrins are the prosthetic groups responsible for the transport and storage of oxygen in hemoglobin and myoglobin.[1] Synthetic metal porphyrins mimic many of the chemical and physical properties of their biological counterparts. These properties can be tailored by coordination of specific metal centers, typically those of Fe, Mg, Ni and Co. Metalloporphyrins can also be found as building blocks in some metal-organic frameworks (MOF's). These materials are finding applications in selective gas storage and separation and in catalysis.[2-13] Metalloporphyrins can be considered to be models for important portions of some MOF's. Identifying the electronic and structural properties of isolated metal porphyrins is important for understanding their ability to bind small molecules and to transfer electrons. This may lead to insight on how to design MOFs for specific applications.

Several gas-phase studies of porphyrins have been conducted by collision induced dissociation (CID),[14-16] although resonance Raman[17] and ion cyclotron resonance (ICR) mass spectrometry[18,19] studies have also been reported. Additionally, photoelectron spectroscopy experiments on both neutrals[20] and anions[21] of porphyrins have been carried out. In particular, multiply-negatively-charged anions of meso-tetra-(4-sulfonatophenyl)-porphyrins with Mn and Cu metal centers were studied by Kappes and co-workers using anion photoelectron spectroscopy.[21] Similarly, phthalocyanines, which are closely related to porphyrins, have also been examined by negative ion photoelectron spectroscopy. Specifically, Wang and co-workers studied multiply negatively-charged copper phthalocyanine tetrasulfonate anions and found the excess charges to be localized on the peripheral –SO_3 functional groups.[22,23] Nevertheless, until now, no photoelectron spectra of singly-charged, parent negative ions of porphyrins or porphyrin analogs have been measured.

Here, we focus on studying singly-charged, transition metal, tetraphenyl porphyrin parent anions, $M(TPP)^-$. Tetraphenyl porphyrins are heterocyclic macromolecules composed of four modified pyrrole sub-units linked together around a metal center, M, by four methine (=CH-) bridges, each of these having a phenyl functional group, i.e., M(TPP). The structure of these porphyrins is depicted in Figure IV.3. Singly-charged negative ions of both $Fe(TPP)^-$ and $Ni(TPP)^-$ were first observed by Ridge and co-workers in ICR mass spectrometric experiments, from which they reported electron affinities.[18,19] Somewhat later, a theoretical study by Liao and Scheiner found that $Fe(TPP)^-$ accommodates its excess electron among iron's d-orbitals, whereas in $Ni(TPP)^-$ the excess electron was found to reside in the π* orbital of the porphyrin's heterocyclic moieties.[24]

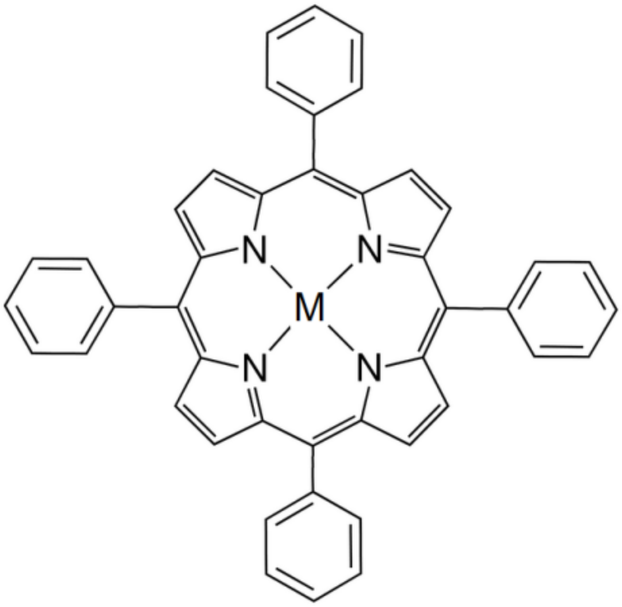

Figure IV.3: A tetraphenylporphine with a metal center, i.e., M(TTP).

In this work, we present a negative ion photoelectron spectroscopic and density functional theoretical (DFT) study of three such systems, i.e., Fe(TPP)$^-$, Mn(TPP)$^-$, and Ni(TPP)$^-$, from which we determine the electron affinities of their neutral counterparts. These are compared with results from previous studies.

IV.2.2. EXPERIMENTAL AND COMPUTATIONAL METHODS

Anion photoelectron spectroscopy is conducted by crossing a beam of mass-selected negative ions with a fixed-frequency photon beam and energy-analyzing the resultant photodetached electrons. The photodetachment process is governed by the energy-conserving relationship hν = EBE + EKE, where hν is the photon energy, EBE is the electron binding energy, and EKE is the electron kinetic energy. Measuring electron kinetic energies and knowing the photon energy provides electron binding (photodetachment transition) energies. Because these transitions are vertical, their relative intensities and band shapes are determined by the extent of Franck−Condon overlap between the anion and its corresponding neutral. The apparatus consists of a laser photoemission/oven anion source, a linear time-of-flight mass spectrometer for mass analysis and mass selection, a magnetic bottle electron energy analyzer, and a Nd:YAG photodetachment laser. The instrumental resolution of the photoelectron spectrometer is ∼35 meV at a 1 eV EKE. The third (355 nm) harmonic of a Nd:YAG laser was used to photodetach the mass-selected porphyrin molecular anions. Photoelectron spectra were calibrated against the well-known atomic transitions of Cu$^-$.

To produce the parent porphyrin anions, Fe(TPP)$^-$, Mn(TPP)$^-$, and Ni(TPP)$^-$, small amounts of 5,10,15,20-tetraphenyl-21*H*,23*H*-porphine iron(III) chloride, 5,10,15,20-tetraphenyl-

21*H*,23*H*-porphine manganese(III) chloride, and 5,10,15,20-tetraphenyl-21*H*,23*H*-porphine nickel(II) powder, respectively, were placed in a small oven (heated to 60, 80, 25 °C, respectively) attached to the front of a pulsed (10 Hz) gas valve (General Valve Series 9), where helium (at 75, 285, 75 psia, respectively) was expanded over the samples and into a high vacuum chamber (10^{-6} Torr). Just outside the orifice of the oven, low-energy electrons were produced by laser/photoemission from a pulsed Nd:YAG laser beam (10 Hz, 532 nm) striking a translating, rotating, copper rod (6.35 mm diameter) (see Figure IV.4). Negatively-charged anions were then pulse-extracted into the spectrometer prior to mass selection and photodetachment.

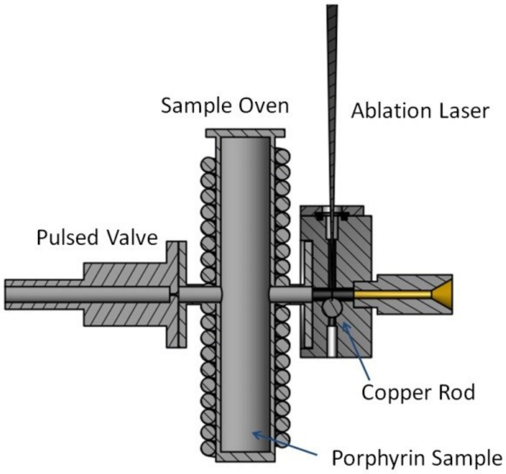

Figure IV.4: A cross sectional view of the laser photoemission/oven anion source.

Electron detachment spectra from the anion have been calculated using PBE-GGA,[25] NRLMOL, and very large Gaussian-orbital basis sets.[26,27] In all cases the anion geometry has been fully relaxed. For example, for the Fe center we have used 20 single Gaussians, with decay parameters ranging between $0.0452\text{-}3.87\text{x}10^6$, to construct a set of 11 s-type contracted Gaussians, 4 of which have r^2 pre-factors, 5 p-type contracted Gaussians, and 4 d-type contracted Gaussians. Similar size basis sets were used for the Ni- and Mn-calculations. For the nitrogen atoms we used 13-single Gaussians, with decay parameters ranging from 0.094-5.18x10^5, to construct a set of 8 s-type contracted Gaussians, 3 of which have r^2 pre-factors, 3 p-type contracted Gaussians, and 4 d-type contracted Gaussians. For the carbon atoms we used 12-single Gaussians ranging between 0.077-2.22x10^4 with the same contractions as for the N case. For the hydrogen atoms we used 6-single Gaussians, with decay parameters ranging from 0.0745-77.8, to construct a set of 4 s-type contracted Gaussians, 1 of which has an r^2 pre-factors, 2 p-type contracted Gaussians, and 1 d-type contracted Gaussians. These basis sets have been well tested on molecular magnets, which contain multiple ligated transition-metal centers. The functions satisfy a theorem,[27] which says that the shortest range function on each atom should scale as $Z^{10/3}$ to ensure that basis-set superposition error, rigorously for the 1s-core electrons, is zero. A discussion of the numerical details and the strategy for massive parallelization has been presented elsewhere.[26] Additionally, calculations using this same methodology have been applied to molecules having metal ions[28-30] and to porphyrin complexes.[31]

All possible rotations of phenyl groups in neutral Fe(TPP) were tested. The structure with all four phenyl groups perpendicular to the plane of the porphyrin was found to be the lowest energy structure, by 2.93 eV, relative to the structure composed of two in-plane phenyl groups and two phenyl groups perpendicular to the plane of the porphyrin. The structure with all phenyl groups in plane was found to be 7.16 eV above the lowest porphyrin geometry. The sterically hindered structures are high enough in energy so that they are not expected to be present in the experiment. For the lowest energy structure, we find the neutral state to have a triplet ground state. The relaxed anion structure with four perpendicular phenyl groups is a doublet. This protocol was utilized for all three porphyrin anion systems studied here for calculating the main features of their photoelectron spectra.

IV.2.3. RESULTS AND DISCUSSION

The photoelectron spectra of Fe(TPP)$^-$, Mn(TPP)$^-$, and Ni(TPP)$^-$ parent anions are presented in Figure IV.5. The photoelectron spectrum of the Fe(TPP)$^-$ anion contains two vibrationally unresolved, electronic transitions (bands), centered at 2.0 eV and 3.1 eV. Two unresolved electronic bands are also observed in the Mn(TPP)$^-$ anion spectrum, centered at 1.7 eV and 3.1 eV. The spectrum of the Ni(TPP)$^-$ anion contains at least four unresolved bands, centered at 1.6 eV, 2.3 eV, 3.0 eV, and 3.4 eV.

The adiabatic electron affinity, EA, is the energy difference between the lowest energy state of the anion and the lowest energy state of its neutral counterpart. When significant Franck-Condon overlap exists between $v'' = 0$ of the anion and $v' = 0$ of its corresponding neutral (the origin transition) and when vibrational hot bands are not a significant issue, the EBE of the intensity threshold corresponds to the EA value. Since the structures of these anions and their neutral counterparts are similar, we expect the origin transitions to be present under the observed spectral bands. Although the presence of vibrational hot bands is more difficult to assess *a priori*, the strong helium expansions and the low porphyrin densities that were used in these experiments make it likely that the porphyrin anions were relatively cool. Thus, we interpret the EBE values of the observed intensity thresholds in these anion spectra to be the EA values of their neutral counterparts. The EA values for Fe(TPP), Mn(TPP), and Ni(TPP) were thus determined to be 1.8 eV, 1.6 eV, and 1.5 eV, respectively. We designate an uncertainty of ±0.1 eV in each case.

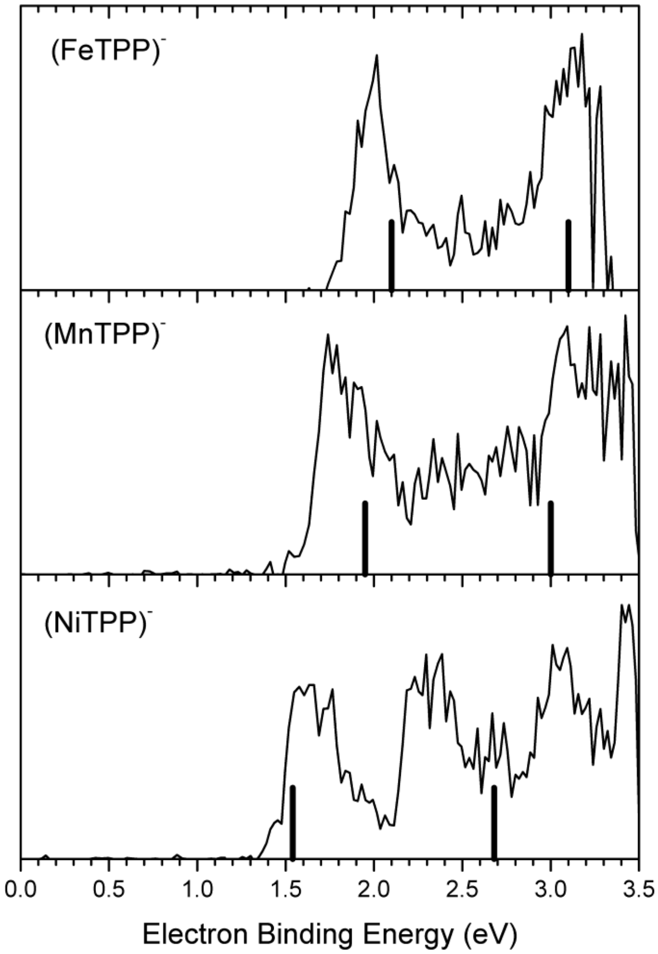

Figure IV.5: The anion photoelectron spectra of Fe(TPP)$^-$, Mn(TPP)$^-$, and Ni(TPP) measured with 355 nm photons. The calculated transitions are shown as stick spectra.

Computationally, the vertical detachment transition energies (no geometry relaxation) are determined by calculating the vertical energy difference between the anion's ground state and the various electronic states of their neutral counterpart, each of these at the structure of the anion. For Fe(TPP)$^-$, we identified a bound doublet anion with vertical transitions to its neutral triplet and singlet states at 2.1 eV and 3.1 eV, respectively. A bound triplet anion was found for Mn(TPP)$^-$ with vertical transitions to its neutral quartet and doublet states occurring at 1.95 eV and 3.0 eV, respectively. Ni(TPP)$^-$, exists as a bound doublet anion with vertical transitions to its neutral singlet and triplet states at 1.54 eV and 2.68 eV, respectively. In most cases, our calculated transition energies are consistent with our experimentally-determined values. However, there is a small discrepancy between experiment and theory in the case of the second calculated photoelectron transition for Ni(TPP)$^-$. It is well known that the application of DFT is often more challenging for nickel than for other transition metals,[32] where Hubbard-U approximations are often needed to obtain a qualitatively correct valence, within PBE-GGA, for the Ni ion.[33] Nevertheless, this suggests that the relatively large molecular systems discussed here, especially the Ni-system, should provide good tests for the recently proposed self-interaction corrected density functional methods.[34,35] These have recently been applied to systems containing isolated and open metal centers, similar to those discussed here.[35,36]

Our experimental and computational results are summarized in Table IV.2. The transition energy from the anion's ground state to the ground state of its corresponding neutral is generally referred to as the vertical detachment energy, VDE, this being the EBE of the intensity maximum for that band. Similarly, the next higher energy transition is from the anion's ground state to the first excited state state of the anion's neutral counterpart. These six values are presented in Table IV.2. Likewise, the first two calculated transition energies for all three porphyrin systems studied here are also presented there. Our experimentally reported electron affinities for Fe(TPP), Mn(TPP), and Ni(TPP) are 1.8 eV, 1.6 eV, and 1.5 eV, respectively. Those for Fe(TPP) and Ni(TPP) are in excellent agreement with the experimental EA values obtained previously by Ridge and co-workers[18,19] (1.87 eV and 1.51 eV, respectively) as well as with the calculated values for the same two systems by Liao and Scheiner[24] (1.82 eV and 1.51 eV, respectively). In the cases of Fe(TPP) and Ni(TPP), the excellent agreement between our photoelectron-determined EA values, the

ICR-determined EA values of Ridge and co-workers, and the calculated EA values of Liao and Scheiner validates our assumption of insignificant vibrational excitation (hot bands) in their anions.

Table IV.2: Experimentally-Observed and Theoretically-Calculated Transitions of Metal-Tetraphenyl Phorphyrins and their Anions

Porphyrin	**EA**	**VDE**		**Vertical transition to first excited neutral state**	
	Experiment	Experiment	Theory	Experiment	Theory
Fe(TPP)	1.8	2.0	2.1 (S=1/2 to S=1)	3.1	3.1 (S=1/2 to S=0)
Mn(TPP)	1.6	1.7	1.95 (S=1 to S=3/2)	3.1	3.0 (S=1 to S=1/2)
Ni(TPP)	1.5	1.6	1.54 (S=1/2 to S=0)	2.3	2.68 (S=1/2 to S=1)

ACKNOWLEDGEMENTS

This research was supported in part by the U.S. Department of Energy, Office of Basic Energy Sciences, Division of Chemical Sciences, Geosciences and Biosciences under Award DE-FG02-12ER16362. This research was also supported in part by the U. S. National Science Foundation under Grant Number CHE-1360692 (KHB).

REFERENCES

1. Scheidt, W. R.; Reed, C. A. Spin-State/Stereochemical Relationships in Iron Porphyrins: Implications for Hemoproteins. *Chem. Rev.* **1981**, 81, 543-555.

2. Karpuschkin, T.; Kappes, M. M.; Hampe, O. Binding of O_2 and CO to Metal Porphyrin Anions in the Gas Phase. *Angew. Chem. Int. Ed.* **2013**, 52, 10374-10377.

3. Chen, O.; Groh, S.; Liechty, A.; Ridge, D. P.; Binding of Nitric Oxide to Iron (II) Porphyrins: Radiative Association, Blackbody Infrared Radiative Dissociation, and Gas-Phase Association Equilibrium. *J. Am. Chem. Soc.* **1999**, 121, 11910-11911.

4. Abrahams, B. F.; Hoskins, B. F.; Robson, R. A New Type of Infinite 3D Polymeric Network Containing 4-Connected, Peripherally Linked Metalloporphyrin Building Blocks. *J. Am. Chem. Soc.* **1991**, 131, 3606-3607.

5. Wang, X.-S.; Meng, L.; Cheng, Q.; Kim, C.; Wojtas, L.; Chrzanowski, M.; Chen, Y.-S.; Zhang, X. P.; Ma, S. Three-Dimensional Porous Metal-Metalloporphyrin Framework Consisting of Nanoscopic Polyhedral Cages. *J. Am. Chem. Soc.* **2011**, 133, 16322-16325.

6. Lee, D. H.; Kim, S.; Hyun, M. Y.; Hong, J.-Y.; Huh, S.; Kim, C.; Lee, S. J. Controlled Growth of Narrowly Dispersed Nanosize Hexagonal MOF rods from Mn(III)-porphyrin and In(NO_3)$_3$ and Their Applications in Olefin Oxidation. *Chem. Commun.* **2012**, 48, 5512-5514.

7. Feng, D.; Gu, Z.-Y.; Li, J.-R.; Jiang, H.-L.; Wei, Z.; Zhou, H.-C. Zironium_Metlloporphyrin PCN-22: Mesoporous Metal-Organic Frameworks with Ultrahight Stability as Biomimetic Catalysts. *Angew. Chem. Int. Ed.* **2012**, 51, 10307-10310.

8. Wang, X.-S.; Chrzanowski, M.; Kim, C.; Gao, W.-Y.; Wojtas, L.; Chen, Y.-S.; Zhang, X. P.; Ma, S. Quest for Highly Porous Metal-Metalloporphyrin Framework Based Upon a Custom-Designed Octatopic Porphyrin Ligand. *Chem. Commun.* **2012**, 48, 7172-7175.

9. Zha, Q.; Ding, C.; Rui, X.; Xie, Y. A Novel Porphyrin-Based Ligand Containing Four 4,4′-
Dipyridylamine Moieties: Syntheses, Structures, and Luminescent Properties of Mn(II), Cu(II), Zn(II), and Cd(II) Coordination Polymers. *Cryst. Growth Des.* **2013**, 13, 4583-4590.

10. Feng, D.; Chung, W.-C.; Wei, Z.; Gu, Z.-Y.; Jiang, H.-L.; Chen, Y.-P.; Darensbourg, D. J.; Zhou, H.-C. Construction of Ultrastable Porphyrin Zr Metal-Organic Frameworks Through Linker Elimination. *J. Am. Chem. Soc.* **2013**, 135, 17105-17110.

11. Johnson, J. A.; Chen, S.; Reeson, T. C.; Chen, Y.-S.; Zeng, X. C.; Zhang, J. Direct X-ray Observation of Trapped CO_2 in a Predesigned Porphyrinic Metal-Organic Framework. *Chem. Eur. J.* **2014**, 20, 7632-76732.

12. Gao, W.-Y.; Wojtas, L.; Ma, S. A Porous Metal-Metallophorphyrin Framework Featuring High-Density Active Sites for Chemical Fixation of CO_2 Under Ambient Conditions. *Chem. Commun.* **2014**, 50, 5316-5318.

13. Day, N. D.; Wamser, C. C.; Walter, M. G. Porphyrin Polymers and Organic Frameworks. *Polym. Int.* (**2015**) doi: 10.1002/pi.4908

14. Vandell, V. E.; Limbach, P. A. Electrospray Ionization Mass Spectrometry of Metallopophyrins. *J. Mass Spectrom.* **1998**, 33, 212-220.

15. Gozet, T.; Huynh, L.; Bohme, D. K. Collision-Induced Dissociation of Tetraphenyl Iron and Manganese Porphyrin Ions by Electrospray Ionization Mass Spectrometry. *Int. J. Mass. Spectrom.* **2009**, 279, 113-118.

16. Jellen, E. E.; Chappell, A. M. Ryzhov, V.; Effects of Size of Noncovalent Complexes on their Stability During Collision-Induced Dissociation. *Rapid Commun. Mass Spectrom.* **2002**, 16, 1799-1804.

17. Asher, S. A.; Murtaugh, J. Metalloporphyrin Gas and Condensed-Phase Resonance Raman Studies: The Role of Vibrational Anharmonicities as Determinants of Raman Frequencies. *J. Am. Chem. Soc.* **1983**, 105, 7244-7251.

18. Chen, H. L.; Ellis, Jr., P. E.; Wijesekera, T.; Hagan, T. E.; Groh, S. E.; Lyons, J. E.; Ridge, D. P., Correlation Between Gas-Phase Electron Affinities, Electrode Potentials, and Catalytic Acivities of Halogenated Metalloporphyrins. *J. Am. Chem. Soc.* **1994**, 114, 1086-1089.

19. Chen, H. L.; Pan, Y. H.; Groh, S.; Hagan T. E.; Ridge, D. P. Gas-Phase Charge-Transfer Reactions and Electron Affinites of Macrocyclic, Anionic Nickel Complexes: Ni(SALEN), Ni(tetraphenylporphyrin), and Derivaties. *J. Am. Chem. Soc.* **1991**, 113, 2766-2767.

20. Amashukeli, X.; Gruhn, N. E.; Lichtenberger, D. L.; Winkler, J. R.; Gray, H. B. Inner-Sphere Electron-Transfer Reorganization Energies of Zinc Porphyrins. *J. Am. Chem. Soc.* **2004**, 126, 15566-15571.

21. Schwarz, U.; Vonderach, M.; Armbruster, M. K.; Fink, K.; Kappes, M. M.; Weis, P. Cu(II)-and Mn(III)-Porphyrin-Derived Oligomeric Multianions: Structures and Photoelectron Spectra. *J. Phys. Chem. A.* **2014**, 118, 369-379.

22.Wang, X.-B.; Ferris, K.; Wang, L.-S. Photodetachement of Gaseous Multiply Charged Anions, Copper Phthalocyanine Tetrasulfonate Tetraanion: Tuning Molecular Electronic Energy Levels by Charging and Negative Electron Binding. *J. Phys. Chem. A* **2000**, 104, 25-33.

23.Wang, X.-B.; Wang, L.-S. Observation of Negative Electron-Binding Energy in a Molecule. *Nature* **1999**, 400, 245-248.

24. Liao, M.-S.; Scheiner, S. Electronic Structure and Bonding in Metal Porphyrins, Meal= Fe, Co, Ni, Cu, Zn. *J. Chem. Phys.* **2001**, 117, 205-219.

25. Perdew, J.P.; Burke, K.; M. Ernzerhof, M. Generalized-Gradient Approximation Made Simple. *Phys. Rev. Lett*. **1996**, 77, 3865.

26. Pederson, M.R.; Porezag, D.V.; Kortus, J.; Patton, D. Strategies for Massively Parallel Local-Orbital-Based Electronic Structure Calculations. *Phys. Status Solidi B* **2000**, 217, 187-218.

27. Porezag D.V.; Pederson M.R. Optimization of Gaussian-Basis Sets for Density-Functional Calculations, *Phys. Rev. A* **1999**, 60, 2840.

28. M.R. Pederson M.R.; Khanna, S.N. Electronic and Magnetic Ordering in Passivated $Mn_{12}O_{12}$-Acetate Nanomagnets. *Chem. Phys. Lett.* **1999**, 307**,** 253-258.

29. K. Park K.; Pederson, M.R. Effect of Extra Electrons on the Exchange and Magnetic Anisotropy in the Anionic Single Molecule Magnet Mn_{12}. *Phys. Rev. B* **1999**, 70, 054414.

30. Nossa, J.F.; Islam, M.F.; Canali C.M.; Pederson, M.R. Electric Control of a {Fe4} Single-Molecule Magnet in a Single-Electron Transistor, *Phys. Rev. B* **2013**, 88**,** 224423.

31. Baruah T.; Pederson, M.R. Density-Functional Study on a Light-Harvesting Carotenoid-Porphyrin-C_{60} Molecular Triad, *J. Chem. Phys.* **2006**, 125**,** 164706.

32. Park, K.; Yang, E.-C.; Hendrickson, D.N. Electronic Structure and Magnetic Anisotropy for Nickel-Based Molecular Magnets, *J. Appl. Physics* **2005**, 97**,** 10M522.

33. Cao, C.; Hill, S.; Cheng, H.P. Strongly Correlated Electrons in the $[Ni(hmp)(ROH)X]_4$ Single-Molecule Magnet. *Phys. Rev. Lett.* **2008**, 100, 167206.

34. Pederson, M.R.; Ruzsinszky, A.; Perdew, J.P. Communication: Self-Interaction Correction with Unitary Invariance in Density-Functional Theory. *J. Chem. Phys.* **2014**, 140**,** 121103.

35. Pederson, M.R. Fermi Orbital Derivatives in Self-Interaction Corrected Density Functional Theory: Applications to Closed Shell Atoms, *J. Chem. Phys.* **2015**, 142, 064112.

36. Pederson, M.R.; Zope, R.; Bursuto, L.; Baruah, T. Self-Interaction-Corrected Electronic Structures for Large Molecules: Applications to C_{60} and a Metal-Porphyrin, (in preparation).

Chapter V: Investigating the Hydrogen Bonding in Model Enzymatic Systems

A highly debated hypothesis for how enzymes provide rate enhancements during catalysis states that the reaction intermediate is stabilized by a short, strong, low barrier hydrogen bond (LBHB) which provides the necessary energy to catalyze the reaction. For this mechanism to be plausible, however, the strength of such a hydrogen bond would have to be unexpectedly high (13-17 kcal/mol). Measuring the hydrogen bond strength between proton-coupled bicarboxylates, and other molecules found in the enzyme-substrate complex, in the gas phase provides an upper limit for the forces available to the enzyme. Here, using anion photoelectron spectroscopy the anion complexes formatic-formic acid, acetate-acetic acid, imidazolium-imidazole, and phenol-phenolate were studied. Under the right environmental conditions, it is plausible LBHBs exist in enzymatic systems.

V.1. Strong, Low Barrier Hydrogen Bonds may be Available to Enzymes

Jacob D. Graham[⊥§], Allyson M. Buytendyk[⊥§], Di Wang[⊥§], Kit H. Bowen[*§] and Kim D. Collins[*‡]

[§] Department of Chemistry, Johns Hopkins University, Baltimore, MD 21218, USA
[‡] BioMET and Department of Microbiology and Immunology, University of Maryland School of Medicine, Baltimore, MD 21201, USA

ABSTRACT

The debate over the possible role of strong, low barrier hydrogen bonds in stabilizing reaction intermediates at enzyme active sites has taken place in the absence of an awareness of the upper limits to the strengths of low barrier hydrogen bonds involving amino acid side chains. Hydrogen bonds exhibit their maximum strengths in isolation, i.e., in the gas phase. In this work, we measured the ionic hydrogen bond strengths of three enzymatically-relevant model systems in the gas phase using anion photoelectron spectroscopy; we calibrated these against the hydrogen bond strength of HF_2^-, measured using the same technique, and we compared our results with other gas-phase experimental data. The model systems studied here: the formate-formic acid, acetate-acetic acid, and imidazolide-imidazole anionic complexes, all exhibit very strong hydrogen bonds, whose strengths compare favorably with that of the hydrogen bifluoride anion, the strongest known hydrogen bond. The hydrogen bond strengths of these gas-phase complexes are stronger than those typically estimated as being required to stabilize enzymatic intermediates. If there were to be enzyme active site environments that can facilitate the retention of a significant fraction of the strengths of these isolated (gas-phase), hydrogen bonded couples, then low barrier hydrogen bonding interactions might well play important roles in enzymatic catalysis.

V.1.1. INTRODUCTION

Enzymes are remarkably efficient catalysts, notable for bringing about rate enhancements of up to 10^{26} with great specificity under gentle conditions.[1] In the early days of enzymology, it was frequently assumed that there must exist some unknown physio-chemical phenomenon that was making a large contribution to these impressive rate enhancements. Even now, fifty years since modern methods were first brought to bear and with enzymatic catalysis firmly established as a pillar of biochemistry, the basis for the proficiency of enzymes, i.e., their "secret", remains elusive.

The early 1990's saw a flurry of activity that provided clues for elucidating this issue. In 1991, the x-ray structure determination by Petsko and Ringe[2] of a triosephosphate isomerase-transition state analog complex[3] and the simultaneous NMR and infrared work of Knowles[4,5] showed that neutral His-95 is the general acid stabilizing the enediolate intermediate in the reaction catalyzed by triose phosphate isomerase (TIM). In 1993, Gerlt and Gassman[6,7] estimated that TIM His-95 was stabilizing the enediolate intermediate by at least 7 kcal/mol, and they postulated that this occurred because the imidazole side chain of neutral His-95 and the enediolate intermediate had matching pK_a values, facilitating the formation of a short, strong (ionic) hydrogen bond between them. At about the same time, Cleland and Kreevoy[8] as well as Frey[9] also postulated the formation of strong, low barrier hydrogen bonds (LBHB) between moieties with matching pK_a values to be an integral part of enzyme catalytic mechanisms. Over time, additional circumstantial evidence came to light in support of the LBHB hypothesis.[10,11] Often, LBHB's were recognized in enzyme structures by their short lengths, their small deuterium fractionation factors, and/or their large downfield, proton NMR chemical shifts.[12,13]

While the LBHB hypothesis in enzyme catalysis had its proponents, it also had its critics, and it remains a controversial issue to this day.[14-16] Its opponents note that the existence of ionic hydrogen bonds in enzyme active sites does not in itself imply that they are unusually strong there, and in fact, they doubt that they are. Arguments from both sides are often based on the known or presumed strengths of ionic hydrogen bonds in different environments. Everyone agrees that hydrogen bonds are at their strongest in the gas phase, i.e., *in vacuo*. Moreover, species whose hydrogen bonds are strong in the gas phase often exhibit quite weak hydrogen bonding in aqueous solution, this likely being due to competition with water for hydrogen bonding. Both Guthrie and Perrin cite the weakening of hydrogen bond strengths in water as evidence that proponents' arguments based on strong hydrogen bonds in the gas phase are not relevant to hydrogen bond strengths in enzymes.[14,15] In solids, x-ray crystallography has provided many examples of short, hydrogen bonds in enzyme structures. Nevertheless, these structural findings are unconvincing to some critics; they do not concede that short hydrogen bond lengths in crystalline enzyme structures imply strong hydrogen bonds.[16] They furthermore argue that hydrogen bonding in crystals is simply not relevant to the environment of the enzyme's active site.

Trending against these criticisms of the LBHB hypothesis are two observations about the cloistered environments of enzyme active sites, on which the viability of short, strong hydrogen bonds there critically depends. First, enzyme active sites typically possess protein loops that fold down over the bound substrate to exclude water.[17] Thus, these sites are largely sequestered from water, making the fact that hydrogen bonds are weakened in aqueous solution beside the point; enzyme sites are not typical aqueous environments.

Second, the expectation of strong enzyme-transition state interactions, with the enzyme "bear-hugging" the transition state[18], suggests a relatively compact, semi-rigid environment at the enzyme active site and brings to mind the relatively immobile, structured environments of crystals, where there is evidence for short, possibly strong hydrogen bonds in some enzyme structures. Both of these characteristics are enabled by the macromolecular architecture of enzymes.

An essential tenet of the criticism against the LBHB hypothesis is that the strengths of enzymatically-relevant hydrogen bonds would have to be unexpectedly high in order for it to be plausible. Indeed, under the LBHB hypothesis, hydrogen bond strengths in the range of 10-20 kcal/mol have been proposed as being necessary to account for the stabilization of enzymatic intermediates.[8,19] How might nature achieve such high hydrogen bond strengths at enzyme active sites? Hydrogen bonded couples exhibit their optimal geometric structures and thus their maximal strengths in the gas phase, i.e., *in vacuo,* primarily because there they do not have competing hydrogen bonding interactions. In condensed phase environments, where potentially competing hydrogen bonding interactions among molecules are plentiful and the optimal structures of hydrogen bonded couples are correspondingly compromised, the average hydrogen bond strength is substantially weaker than in its gas phase counterpart. Environments that suppress competition for forming hydrogen bonds might be expected to allow hydrogen bonded couples to retain a portion of their *in vacuo*, hydrogen bond strengths. The nearly water-free, quasi-rigid structures of enzyme active sites are potentially opportune environments. Thus, it is plausible that some enzyme active sites may provide favorable environments in which hydrogen bond strengths retain a substantial fraction of their gas phase strengths.

Since hydrogen bonds are at their strongest in the gas phase, the strength of a given hydrogen bond there provides an upper limit to its maximum strength in any other environment. In effect, the strength of a hydrogen bonded couple in the gas phase tells us what would be possible in an optimized environment. Thus, measurements of hydrogen bond strengths in the gas phase supply upper limits to their strengths, providing important boundaries. Setting a quantitative benchmark for how strong hydrogen bonds can be at their strongest is the hydrogen bifluoride anion, HF_2^-, in the gas phase. This hydrogen bonded pair, i.e., $F^- \cdots HF$, can also be described as $F^- \cdots H^+ \cdots F^-$, thus its synonym, the proton-coupled bifluoride anion. With a $F^- \cdots HF$ bond strength of 45.8 ± 1.6 kcal/mol (1.99 eV) in the gas phase[20], it is the strongest known hydrogen bond. Even a modest fraction of its *gas phase* strength would be easily enough to supply the needed transition state stabilizations discussed above. Interestingly, the $F^- \cdots HF$ hydrogen bond strength in aqueous solution is only ~0.8 kcal/mol.[21]

Proton-coupled bi-carboxylates top the list as the earliest and still the best-studied systems suspected of forming LBHB's in the vicinity of the active sites of enzymes.[22-24] These hydrogen bonded couples can be depicted as:

Structure 1.

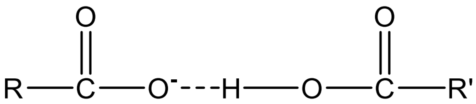

$$R-\overset{\overset{O}{\|}}{C}-O^{-}\cdots H-O-\overset{\overset{O}{\|}}{C}-R'$$

and they can be abbreviated by the general formulae, $X^- \cdots HX$. Proton-coupled bi-carboxylates appear in 16% of all protein x-ray structures.[25] There are at least four x-ray structures showing short hydrogen bonds between an enzyme carboxylate and a transition state analog bound at the enzyme active site.[26] Proton-coupled bi-carboxylates are believed to be important components of the active sites of the aspartic acid proteases, e.g., HIV-1 protease.[27] Carboxylates figure prominently in the LBHB enzymatic story in part because *all* negative charges on proteins are carboxylates.

Another system that is implicated in the formation of LBHB's in the vicinity of the active sites of enzymes is imidazole. In the early days of the LBHB story, the seminal work of Knowles had shown that the neutral imidazole side chain of His-95, acting as the general acid, stabilized the enediolate intermediate (E^-) in the reaction catalyzed by triose phosphate isomerase.[4,5] This hydrogen bonded couple can be depicted as:

Structure 2.

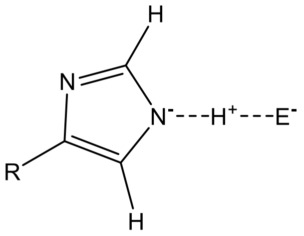

What made imidazole's role as an acid so astonishing was the fact that the pK_a of imidazole (in water) is 14. This apparent dilemma provided among the first clues that LBHB's might be playing important roles in enzyme catalysis.

Given the importance of carboxylates and imidazole in the LBHB story, it is important to know the strengths of their hydrogen bonded couples in the gas phase (*in vacuo*) in order to establish their maximal possible values. Unfortunately, the debate over the possible role of strong, low barrier hydrogen bonds in stabilizing reaction intermediates at enzyme active sites has taken place in the absence of an awareness of the upper limits to the strengths of low barrier hydrogen bonds involving amino acid side chains. To help fill this gap, we have utilized anion photoelectron spectroscopy to measure the hydrogen bond strengths of the formate-formic acid, acetate-acetic acid, and imidazolide-imidazole, anion-neutral, intermolecular, hydrogen bonded complexes (couples) *in vacuo*. To make a uniform comparison, we also measured the hydrogen bond strength of HF_2^-, i.e., the F^--HF anion-neutral interaction energy using this same experimental technique.

V.1.2. EXPERIMENTAL PROCEDURES

Anion photoelectron spectroscopy is conducted by crossing a mass-selected beam of negative ions with a fixed-frequency photon beam and energy-analyzing the resultant photodetached electrons. Photodetachment transitions occur between the ground state of a mass-selected negative ion and the ground and energetically-accessible excited states of its neutral counterpart. This process is governed by the energy-conserving relationship, hν = EBE + EKE, where hν is the photon energy, EBE is the electron binding energy, and EKE is the electron kinetic energy. Measuring electron kinetic energies and knowing the photon energy, provides electron binding (photodetachment transition) energies. Since these are vertical transitions, their relative intensities are determined by the extent of Franck-Condon overlap between the anion and its corresponding neutral. Our apparatus consists of a laser vaporization anion source, a linear time-of-flight mass spectrometer for mass analysis and mass selection, a momentum decelerator, a magnetic bottle electron energy analyzer, and an ArF excimer laser. The magnetic bottle has a resolution of ~50 meV at EKE = 1 eV. In these experiments, photoelectron spectra were recorded with 193 nm (6.42 eV) photons. The photoelectron spectra were calibrated against the well-known transitions of atomic Cu^-. A detailed description of the apparatus has been reported elsewhere.[28]

To produce the fluoride, hydrogen bifluoride; formate, formate-formic acid; and acetate, acetate-acetic acid anions, a small amount of sample (5-pentafluorobenzene, formic acid, or acetic acid, respectively) was entrained in helium (~60 psi) and expanded through the nozzle orifice (0.79 mm diameter) of a pulsed (10 Hz) valve (General Valve Series 9) in a high vacuum chamber (10^{-6} Torr). To produce the imidazolide and imidazolide-imidazole anions, imidazole was placed in a small oven (~30°C) attached to the front of the pulse valve, where helium (~60 psi) was expanded over the sample in a vacuum chamber. Just outside the orifice of the pulse valve, or in the case of imidazole, just outside the orifice of the oven, low energy electrons were produced by laser/photoemission from a pulsed Nd:YAG laser beam (10Hz, 532 nm) striking a translating, rotating, copper rod (6.35 mm diameter). Negatively-charged anions were then pulse-extracted into the spectrometer prior to mass selection and photodetachment.

V.1.3. RESULTS

In the systems studied here, the $X^- \cdots HX$ anionic complexes are bound, while the corresponding $X \cdots HX$ neutral complexes produced as a result of photodetachment are likely to be unbound. Figure V.1 illustrates this situation schematically, where EA(X) is the adiabatic electron affinity of X, E_{asym} is the energy from the ground state of the $X^- \cdots HX$ anionic complex, i.e., HX_2^-, to the X + HX + e^- energy asymptote, and $D(X^- \cdots HX)$ is the dissociation energy of $X^- \cdots HX$ separating into X^- + HX, i.e., the hydrogen bond strength of the X^- / HX couple. Thus, $D(X^- \cdots HX) = E_{asym} - EA(X)$.

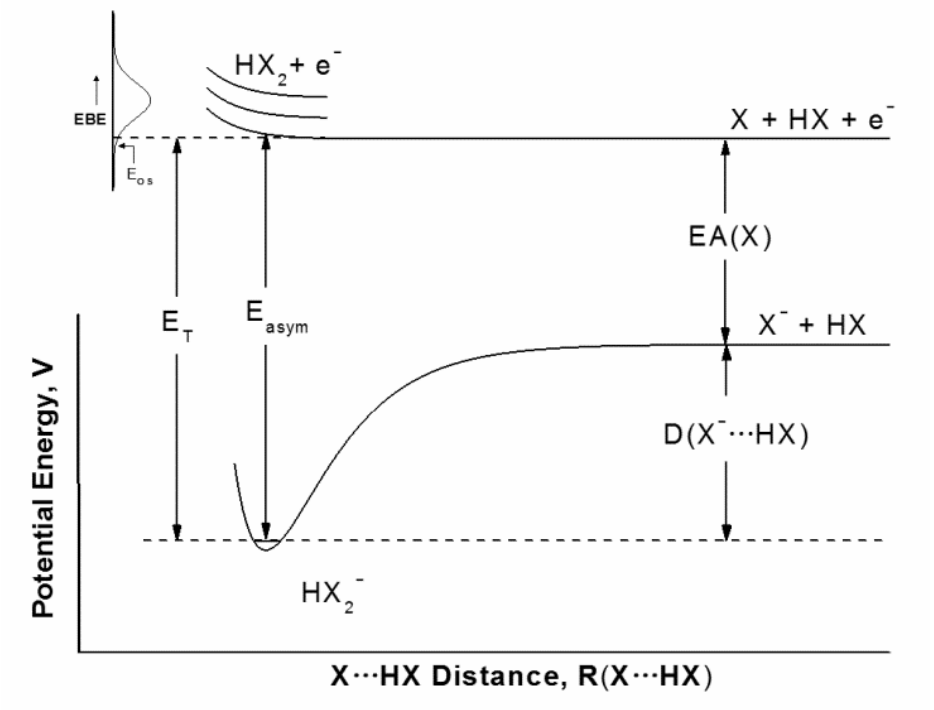

Figure V.1: Schematic representation of the energetics of anion photoelectron (photodetachment) spectroscopy as applied to HX_2^-. Symbols are defined in the text.

In anion photoelectron studies of six hydrogen bihalide anions, HX_2^-, where here X denotes both homogeneous and heterogeneous combinations of the halogen atoms, Cl, Br, and I, Neumark found the X ··· HX neutral complexes, resulting from photodetachment of HX_2^-, to be unbound.[29,30] Importantly, inspection of his photoelectron spectra shows that E_{asym} values, which in these particular cases are known from tabulated EA(X) and D(X^- ··· HX) values, usually lie only ~0.2 eV above the EBE value of the photoelectron intensity onset, E_{OS}, in the corresponding HX_2^- photoelectron spectra. (The low intensity "tail" between E_{asym} and E_{OS} was likely due to photodetachment of vibrationally excited HX_2^- anions, i.e., hot bands.) Furthermore, if one defines a photoelectron intensity threshold, E_T, by extrapolating a straight line to the baseline from high on the low EBE side of the lowest EBE band in each spectrum, then the difference between E_{asym} and E_T becomes even smaller than that between E_{asym} and E_{OS}. Thus, the photoelectron spectra of hydrogen bihalide anions, which are in many ways analogous to the systems under study in the present work, support the approximation that $E_{asym} \cong E_T$. With this, we obtain the working relationship, $D(X^- \cdots HX) \cong E_T(HX_2^-) - EA(X)$.

In the present work, we measured the photoelectron spectra of X^- and of $X^- \cdots HX$ for each of the LBHB candidate systems of interest. Upon determining EA(X) and $E_T(HX_2^-)$ values, their differences provided values of $D(X^- \cdots HX)$, these being the sought-after hydrogen bond strengths of specific X^-/HX couples. In determining EA(X) values from photoelectron spectra of X^- anions, we benefited from previous photodetachment and photoelectron studies of the fluorine atomic anion[31], the formate anion[32], the acetate anion[33], and the imidazolide anion[34]. These studies assigned the origin transitions in their respective X^- photoelectron spectra, thereby providing accurate EA(X) values. While our photoelectron spectra of these same X^- anions were recorded at lower resolution, they are fully consistent with those previously recorded, allowing us to locate the EBE value of their origin transitions on the spectral profiles observed in this study. Values of $E_T(HX_2^-)$ were determined as described above by extrapolation along the low EBE side of the lowest EBE spectral band in our HX_2^- photoelectron spectra.

Figure V.2 presents the photoelectron spectra of corresponding sets of X^- and HX_2^- species measured in this work. In each panel, the spectrum of X^- is positioned above that of HX_2^-, but on the same energy scale, facilitating a pictorial depiction of $D(X^- \cdots HX)$ as the energy difference between specific points (see vertical tick-marks) on the two photoelectron spectra, these points designating the values of EA(X) and $E_T(HX_2^-)$, respectively. For this reason, the length of the horizontal arrow in each panel is a measure of the hydrogen bond

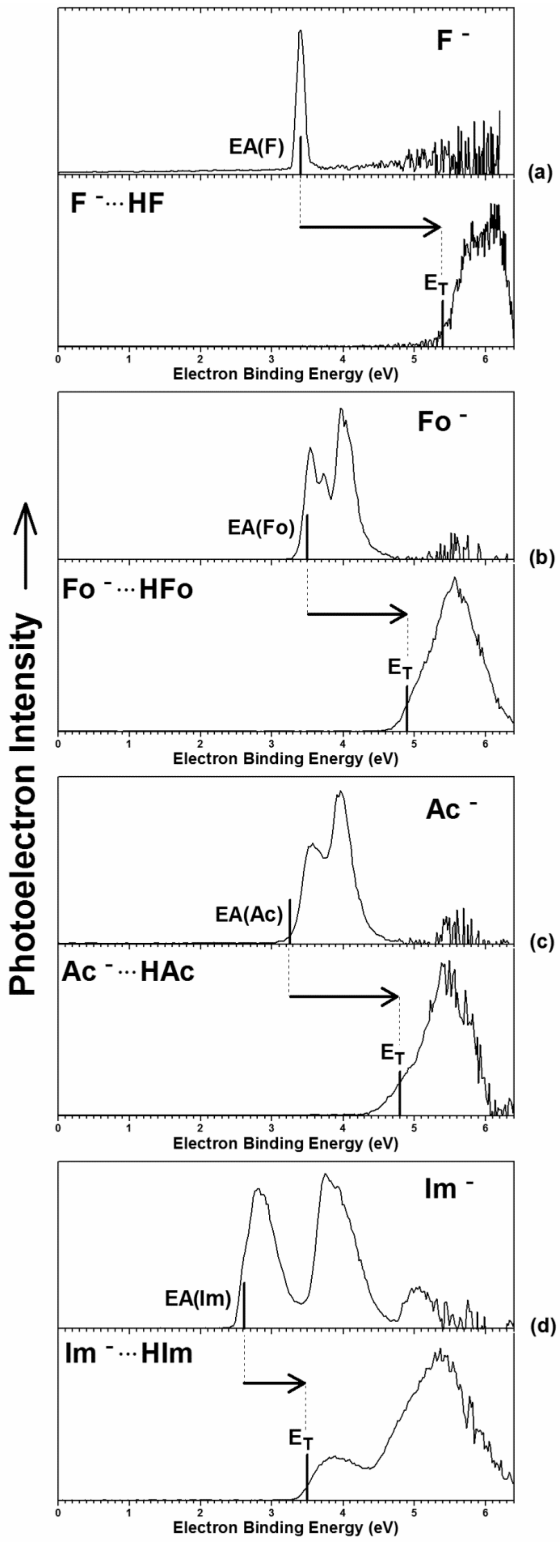

Figure V.2: Anion photoelectron spectra of the four corresponding sets of X^- and HX_2^- species measured in this work. All spectra were calibrated against the well-known photoelectron spectrum of Cu^-, the anion of the copper atom.

strength, D($X^{-} \cdots HX$), of its corresponding HX_2^- species, i.e., of the X^-/HX couple. Referencing the hydrogen bond strengths of the three enzymatic model systems studied here to that of HF_2^-, by using the same experimental method for all four, puts all these measurements on a common footing and provides confidence in comparing the results. Thus, Figures V.2(a-d) successively present the photoelectron spectra of the fluorine anion, F^- and the fluoride-hydrogen fluoride, hydrogen bonded complex, $F^-(HF)$, i.e., HF_2^-; the photoelectron spectra of the formate anion, Fo^- and the formate-formic acid, hydrogen bonded complex, $Fo^-(HFo)$; the photoelectron spectra of the acetate anion, Ac^- and the acetate-acetic acid, hydrogen bonded complex, $Ac^-(HAc)$; and the photoelectron spectra of the imidazolide anion, Im^- and the imidazolide-imidazole, hydrogen bonded complex, $Im^-(HIm)$. Table V.1 presents values of EA(X), $E_T(HX_2^-)$, and D($X^{-} \cdots HX$) for each of the four systems that we studied here, where D($X^{-} \cdots HX$) is the measured hydrogen bond strength for that particular X^-/HX couple.

Table V.1: Values leading to Hydrogen Bond Strengths of X^-/HX couples, i.e., D($X^{-} \cdots HX$). All uncertainties are ± 0.1 eV or less.

$X^{-} \cdots HX$ System	EA(X) Literature	$E_T(HX_2^-)$ This Work	D($X^{-} \cdots HX$) This Work		% of F-HF HB Strength
	eV	eV	eV	kcal/mol	%
$F^{-} \cdots HF$	3.40[a]	5.4	2.0	46	100%
$Fo^{-} \cdots HFo$	3.50[b]	4.9	1.4	32	70%
$Ac^{-} \cdots HAc$	3.25[c]	4.8	1.6	37	80%
$Im^{-} \cdots HIm$	2.61[d]	3.5	0.9	21	45%

[a]Ref 31, [b]Ref 33, [c]Ref 33, [d]Ref 34

V.1.4. DISCUSSION

In the past, the dissociation energies of the HX_2^- systems studied here have also been determined in the gas phase by Wenthold and Squires, using energy-resolved, collision-induced dissociation (CID)[20] and by Meot-Ner (Mautner), using high pressure mass spectrometry and van't Hoff plots.[35,36] The CID measurement of the hydrogen bond strength of HF_2^- gave 1.99 eV (45.8 kcal/mol), whereas the HF_2^- hydrogen bond strength measured in our work was 2.0 eV (46 kcal/mol). The thermodynamic/van't Hoff plot determinations of the hydrogen bond strengths of $Fo^-(HFo)$, $Ac^-(HAc)$, and $Im^-(HIm)$ were 1.60 eV (36.8 kcal/mol), 1.27 eV (29.3 kcal/mol), and 1.14 eV (26.4 kcal/mol), respectively, whereas the hydrogen bond strengths of the corresponding species measured in our spectroscopic work were 1.4 eV (32 kcal/mol), 1.6 eV (37 kcal/mol), and 0.9 eV (21 kcal/mol), respectively. What is important about these complementary measurements is that their values, while measured using different techniques, are comparable. They support one another by yielding the same approximate values for corresponding hydrogen bond strengths.

The core result of both the present and previous work is that all three of the enzymatically-relevant model systems considered here exhibit upper limit (gas phase), hydrogen bond strengths that are very strong. According to our measurements, the hydrogen bond strengths of the formate-formic acid, acetate-acetic acid, and imidazolide-imidazole complexes are respectively 70%, 80%, and 45% of the strength of the fluoride-hydrogen fluoride complex, HF_2^-, with values from previous measurements giving similar percentages. Thus, the carboxylate and imidazolide, inter-molecular hydrogen bonded X^-/HX couples queried here in the gas phase do indeed have hydrogen bond strengths that are comparable to that of the F^-/HF hydrogen bonded couple. Furthermore, it is also interesting to note that in a gas phase, photoelectron study by Wang[37], the shift between *trans*- versus *cis*- $HO_2CCH{=}CHCO_2^-$ (the fumaric/maleic acid mono-anion) spectra revealed the *intra*-molecular hydrogen bond strength in the *cis*-isomer (hydrogen maleate) to be 21.5 kcal/mol, which is 47% of the hydrogen bond strength of HF_2^-.

The threshold hydrogen bond strengths needed to account for the stabilization of enzymatic intermediates have been variously estimated to lie between 7 kcal/mol[6,7] (in the case of imidazole) and 20 kcal/mol.[8,19] The gas-phase, hydrogen bond strengths that we measured for the $Fo^-(HFo)$, $Ac^-(HAc)$, and $Im^-(HIm)$ complexes are 32 kcal/mol, 37 kcal/mol, and 21 kcal/mol, respectively. The lower threshold value of 7 kcal/mol is 22%, 19%, and 33% of the measured hydrogen bond strengths of these complexes, respectively, whereas the higher threshold value of 20 kcal/mol is 63%, 54%, and 105% of these same strengths, respectively. If there were to exist enzyme active site environments that allowed hydrogen bonded couples to retain significant percentages of their gas phase (isolated) strengths, and if these exceeded the pertinent threshold values, then ionic hydrogen bonding might well figure prominently in facilitating enzymatic rate enhancements.

By definition, an environment in which a hydrogen bonded couple has no opportunity to form alternative hydrogen bonds would preserve its strength, *viz.*, *in vacuo* (gas phase). In solution (liquids), however, where there may be many competing hydrogen bonding interactions, the strength per hydrogen bonded couple would be lowered. One can also envision a quasi-solid state regime of limited molecular mobility, lying between these extremes. There, both the opportunities for forming alternative hydrogen bonds (the degree of competition for forming them) and the corresponding strengths of their hydrogen bonds would be intermediate between those of gases and liquids. The envisioned relationship between hydrogen bond strength and the extent of competition in regard to these three environments is illustrated schematically in Figure V.3.

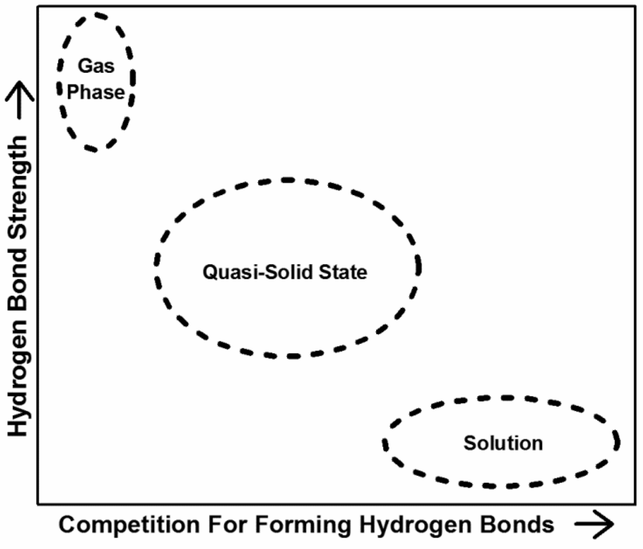

Figure V.3: Schematic representation of the relationship between hydrogen bond strengths and the degree of competition for forming hydrogen bonds in three different environments.

Thus, it is plausible that some enzyme active site environments may correspond to this intermediate case, giving them the possibility of maintaining exceptionally strong hydrogen bonds. Even so, such strong hydrogen bonds would be only part of the story, since other factors, such as local geometry and protein strain, are also expected to play important roles. This work does not prove the validity of the LBHB hypothesis. However, through gas phase (*in vacuo*) measurements, it does provide upper limits to the possible strengths of several enzymatically-relevant hydrogen bond couples. It also suggests a framework for describing how some enzyme active sites might preserve a substantial portion of that strength for their use in catalysis.

ACKNOWLEDGEMENTS

This material is based on work supported by the National Science Foundation under grant number, CHE-1111693 (K.H.B.).

REFERENCES

1. Edwards, D. R., Lohman, D. C. and Wolfenden, R. (2012) Catalytic proficiency: the extreme case of S-O cleaving sulfatases, *J. Am. Chem. Soc. 134*, 525-531.

2. Davenport, R. C., Bash, P. A., Seaton, B. A., Karplus, M., Petsko, G. A., and Ringe, D. (1991) Structure of the triosephosphate isomerase phosphoglycolohydroxamate complex: an analog of the intermediate on the reaction pathway, *Biochemistry 30*, 5821-5826.

3. Collins, K. D. (1974) An activated intermediate analogue: the use of phosphoglycolohydroxamate as a stable analogue of a transiently occurring dihydroxyacetone phosphate-delivered enolate in enzymatic catalysis, *J. Biol. Chem*. 249, 136-142.

4. Lodi, P. J. and Knowles, J. R. (1991) Neutral imidazole is the electrophile in the reaction catalyzed by triosephosphate isomerase: structural origins and catalytic implications, *Biochemistry* 30, 6948-6956.

5. Komives, E. A., Chang, L. C., Lolis, E., Tilton, R. F., Petsko, G. A., and Knowles, J. R. (1991) Electrophilic catalysis in triosephosphate isomerase: the role of histidine-95, B*iochemistry 30*, 3011-3019.

6. Gerlt, J.A. and Gassman, P. G. (1993) An explanation for rapid enzyme-catalyzed proton abstraction from carbon acids: importance of late transition states in concerted mechanisms, *J. Am. Chem. Soc. 115*, 11552-11568.

7. Gerlt, J. A. and Gassman, P. G. (1993) Understanding the rates of certain enzyme-catalyzed reactions: Proton abstraction from carbon acids, acyl transfer reactions, and displacement reactions of phosphodiesters, *Biochemistry 32*, 11943-11952.

8. Cleland, W. W. and Kreevoy, M. M. (1994) Low-barrier hydrogen bonds and enzymic catalysis, *Science 264*, 1887-1890.

9. Frey, P. A., Whitt, S. A. and Tobin, J. B. (1994) A low-barrier hydrogen bond in the catalytic triad of serine proteases. *Science 264*, 1927-1930.

10. Frey, P. A. (2001) Strong hydrogen bonding in molecules and enzymatic complexes, *Magn. Reson. Chem. 39*, S190-S198.

11. Cleland, W. W. (2010) The low-barrier hydrogen bond in enzymic catalysis, *Adv. Phys. Org. Chem. 44*, 1-17.

12. Cleland, W.W. (2000) Low-barrier hydrogen bonds and enzymatic catalysis. *Arch. Biochem. Biophys.* 382, 1-5.

13. Mildvan, A. S., Massiah, M. A., Harris, T. K., Marks, G. T., Harrison, D. H. T., Viragh, C., Reddy, P. M., and Kovach, I. M. (2002) Short, strong hydrogen bonds on enzymes: NMR and mechanistic studies, *J. Mol. Struct. 615*, 163-175.

14. Perrin, C. L. (2010) Are short, low-barrier hydrogen bonds unusually strong?, *Acc. Chem. Res. 43*, 1550-1557.

15. Guthrie, J.P. (1996) Short strong hydrogen bonds: can they explain enzymic catalysis? *Chem. Biol. 3*, 163-170.

16. Perrin, C. L. and Nielson, J. B. (1997) "Strong" hydrogen bonds in chemistry and biology. *Annu. Rev. Phys. Chem. 48*, 511-544.

17. Malabanan, M. M., Amyes, T. L., and Richard, J. P. (2010) A role for flexible loops in enzyme catalysis, *Curr. Opin. Struct. Biol. 20*, 702-710.

18. Snider, M. G., Temple, B. S., and Wolfenden, R. (2004)The path to the transition state in enzyme reactions: a survey of catalytic efficiencies, *J. Phys. Org. Chem. 17*, 586-591.

19. Snider, M. J., Gaunitz, S., Ridgway, C., Short, S. A., and Wolfenden, R. (2000) Temperature effects on the catalytic efficiency, rate enhancement, and transition state affinity of cytidine deaminase, and the thermodynamic consequences for catalysis of removing a substrate "anchor", *Biochemistry 39*, 9746-9753.

20. Wenthold, P. G. and Squires, R. R. (1995) Bond dissociation energies of F_2^- and HF_2^-. a gas-phase experimental and G2 theoretical study, *J. Phys. Chem. 99*, 2002-2005.

21. Kresge, A. J. and Chiang, Y. (1973) Solvent isotope effects on the ionization of hydrofluoric acid, *J. Phys. Chem. 77*, 822-825.

22. Pan, Y. P. and McAllister, M. A. (1997) Characterization of low-barrier hydrogen bonds. 1. microsolvation effects. an ab initio and DFT investigation, *J. Am. Chem. Soc. 119*, 7561-7566.

23. Mariam, Y. H. and Musin, R. N. (2008) Transition from moderate to strong hydrogen bonds: its identification and physical bases in the case of O−H···O intramolecular hydrogen bonds. *J. Phys. Chem. A 112*, 134-145.

24. Guo, J., Tolstoy, P. M., Koeppe, B, Golubev, N. S., Denisov, G. S., Smirnov, S. N., and Limbach, H.-H. (2012) Hydrogen bond geometries and proton tautomerism of homoconjugated anions of carboxylic acids studied via H/D isotope effects on ^{13}C NMR chemical shifts, *J. Phys. Chem. A 116*, 11180-11188.

25. Langkilde, A., Kristensen, S. M., Leggio, L. L., Mølgaard, A., Jensen, J. H., Houk, A. R., Poulsen, J.-C. N., Kauppinen, S., and Larsen, S. (2008) Short strong hydrogen bonds in proteins: a case study of hamnogalacturonan acetylesterase, *Acta Crystallogr.* D64, 851-863.

26. Collins, K.D. (2012) Why continuum electrostatics theories cannot explain biological structure, polyelectrolytes or ionic strength effects in ion-protein interactions. *Biophys. Chem. 167*, 43-59.

27. Shen, C.H., Tie, Y., Yu, X., Wang, Y.-F., Kovalevsky, A. Y., Harrison, R. W., and Weber, I. T. (2012) Capturing the reaction pathway in near-atomic-resolution crystal

structures of HIV-1 protease, *Biochemistry 51*, 7726-7732.

28. O. C. Thomas, W. J. Zheng, and K. H. Bowen, "Magic numbers in copper-doped aluminum cluster anions", J. Chem. Phys., 114, 5514-5519 (2001).

29. Metz, R. B., Weaver, A., Bradforth, S. E., Kitsopoulos, T. N., and Neumark, D. M. (1990) Probing the transition state with negative ion photodetachment: the chlorine atom + hydrogen chloride and bromine atom + hydrogen bromide reactions, *J. Phys. Chem. 94*, 1377-1388.

30. Bradforth, S. E., Weaver, A., Arnold, D. W., Metz, R. B., and Neumark, D. M. (1990) Examination of the Br + HI, Cl + HI, and F + HI hydrogen abstraction reactions by photoelectron spectroscopy of $BrHI^-$, $ClHI^-$, and FHI^-, *J. Chem. Phys. 92*, 7205-7222.

31. Blondel, C. (1995) Recent experimental achievements with negative ions, *Phys. Scr. 58*, 31-42.

32. Kim, E.H., Bradforth, S. E., Arnold, D. W., Metz, R.B., and Neumark, D. W. (1995) Study of HCO_2 and DCO_2 by negative ion photoelectron spectroscopy, *J. Chem. Phys. 103*, 7801-7814.

33. Wang, X-B., Woo, H-K., Wang, L-S., Minofar, B., and Jungwirth, P. (2006) Determination of the electron affinity of the acetyloxyl radical (CH_3COO) by low-temperature anion photoelectron spectroscopy and ab initio calculations, *J. Phys. Chem. A 110*, 5047-5050.

34. Gianola, A. J., Ichino, T., Hoenigman, R. L., Kato, S., Bierbaum V. M., and Lineberger, W. C. (2005) Photoelectron spectra and ion chemistry of imidazolide. *J. Phys. Chem. A 109*, 11504-11514.

35. Meot-Ner (Mautner), M. and Sieck, L. W. (1986) The ionic hydrogen bond and ion solvation. 5. OH-*O- bonds. gas-phase solvation and clustering of alkoxide and carboxylate anions, *J. Am. Chem. Soc. 108*, 7525-7529.

36. Meot-Ner (Mautner), M. (1988) Models for strong interactions in proteins and enzymes. 2. interactions of ions with the peptide link and with imidazole, *J. Am. Chem. Soc. 110*, 3075-3080.

37. Woo, H-K., Wang, X-B., Wang, L-S., and Lau, K-C. (2005) Probing the low-barrier hydrogen bond in hydrogen maleate in the gas phase: a photoelectron spectroscopy and ab initio study, *J. Phys. Chem. A 109*, 10633-10637.

V.2. The Hydrogen Bond Strength of the Phenol-Phenolate Anionic Complex: A Computational and Photoelectron Spectroscopic Study

Allyson M. Buytendyk[§], Jacob D. Graham[§], Kim D. Collins[‡] and Kit H. Bowen[*§]

[§] *Department of Chemistry, Johns Hopkins University, Baltimore, MD 21218, USA*
[‡] *IMET and Department of Microbiology and Immunology, University of Maryland School of Medicine, Baltimore, MD 21201, USA*

Chia-Hua Wu[#] and Judy I. Wu[#]

[#]*Department of Chemistry, University of Houston, Houston, TX 77204, USA*

ABSTRACT

The phenol-phenolate anionic complex was studied *in vacuo* by negative ion photoelectron spectroscopy using 193 nm photons and by density functional theory (DFT) computations at the ωB97XD/6-311+G(2d,p) level. We characterize the phenol-phenolate anionic complex as a proton-coupled phenolate pair, i.e., as a low-barrier hydrogen bond system. Since the phenol-phenolate anionic complex was studied in the gas phase, its measured hydrogen bond strength is its maximal ionic hydrogen bond strength. The D($PhO^- \cdots HOPh$) interaction energy (26-30 kcal/mol), i.e., the hydrogen bond strength in the $PhO^- \cdots HOPh$ complex, is quite substantial. Block-localized wavefunction (BLW) computations reveal that hydrogen bonded phenol rings exhibit increased ring π-electron delocalization energies compared to the free phenol monomer. This additional stabilization may explain the stronger than expected proton donating ability of phenol.

V.2.1. INTRODUCTION

Phenol and its chemical derivatives are important building blocks in biological systems. Phenol is the side-chain functional group in the amino acid, tyrosine. Deprotonated phenol, i.e., the phenolate anion, enjoys enhanced stabilization due to the delocalization of its excess charge onto the aromatic ring.[1-5] For this reason, phenol exhibits slightly higher gas-phase acidity than most alcohols.[6-9] While the correlation between electronegativities and hydrogen bond strengths in OH/O- proton-coupled complexes has been studied theoretically,[10-13] there have been no gas-phase experiments involving the phenol-phenolate anions.

The phenol-phenolate anionic complex can also be viewed as a likely example of an ionic, low-barrier hydrogen bond (LBHB). In a LBHB, a proton is shared between anions whose conjugate acids have matching or near matching pK_a values. Some enzymologists postulate that the remarkable rate enhancements seen in enzyme catalysis are due in part to the formation of strong, short LBHBs.[14-18] A ^{1}H NMR study by Mildvan and coworkers[19] provided evidence for the existence of a LBHB between the phenolic proton of the Tyr-14 side chain in the enzyme active site of Δ^5-3-ketosteroid isomerase (KSI) and the dienolate reaction intermediate. The strength of that hydrogen bond was estimated to be at least 7.1 kcal/mol (0.31 eV), whereas typical hydrogen bond strengths in proteins are somewhat smaller. In the gas phase (*in vacuo*), this value might be expected to be significantly larger, because competition among hydrogen bonding partners in condensed phase environments usually reduces hydrogen bond strengths compared to those in the gas phase, where there is no competition. We view the gas-phase, phenol-phenolate anionic complex as an elementary model for the above enzymatic interaction.

V.2.2. METHODS

V.2.2.1 Experimental

Anion photoelectron spectroscopy is conducted by crossing a mass-selected beam of negative ions with a fixed-frequency photon beam and energy-analyzing the resultant photodetached electrons. Photodetachment transitions occur between the ground state of a mass-selected negative ion and the ground and energetically accessible excited states of its neutral counterpart. This process is governed by the energy-conserving relationship hν = EBE + EKE, where hν is the photon energy, EBE is the electron binding energy, and EKE is the electron kinetic energy. Measuring electron kinetic energies and knowing the photon energy provides electron binding (photodetachment transition) energies. Because these are vertical transitions, their relative intensities are determined by the extent of Franck−Condon overlap between the anion and its corresponding neutral. Our apparatus consists of a laser photoemission anion source, a linear time-of-flight mass spectrometer for mass analysis and mass selection, a magnetic bottle electron energy analyzer, and an ArF excimer laser. The magnetic bottle has a resolution of ∼50 meV at an EKE of 1 eV. In these experiments, photoelectron spectra were recorded with 193 nm (6.42 eV) photons. The photoelectron spectra were calibrated against the well-known transitions of atomic Cu^-. A description of our apparatus has been reported elsewhere.[20]

To produce the phenolate and phenol−phenolate anions, phenol was placed in a small oven (∼25 °C) attached to the front of a pulsed (10 Hz) valve (General Valve Series 9), where helium (∼45 psia) was expanded over the sample in a high vacuum chamber (10^{-6} Torr). Just outside the orifice of the oven, low-energy electrons were produced by laser/photoemission from a pulsed Nd:YAG laser beam (10 Hz, 532 nm) striking a translating, rotating, copper rod (6.35 mm diameter). Negatively-charged anions were then pulse-extracted into the spectrometer prior to mass selection and photodetachment.

V.2.2.2 Computational

Geometry optimizations for the phenol, phenolate, and phenol−phenolate complex (both radical and anionic forms) as well as the electron affinity of phenolate, EA(PhO), the electron affinity of the phenol-phenolate complex, EA($(PhO_2)H$), the dissociation energy of the neutral phenol-phenolate complex, D(PhO···HOPh), and the dissociation energy of the anionic phenol-phenolate complex dissociating into those two units, D(PhO^-···HOPh), values were computed at ωB97XD[21]/6-311+G(2d,p)[22] (all energies reported include zero-point energy corrections). Minima structures were located and vibrational frequency analyses verified the nature of the stationary points. Basis set superposition error (BSSE) corrections to the hydrogen bonding interaction energies were computed using the counterpoise approach.[23] All computations were performed in Gaussian 09.[24]

Block-localized wavefunction (BLW)[25] computations quantified the π-resonance energies (RE) of the free (monomer) and hydrogen bonded phenol, following the Pauling-Wheland resonance energy definition. The BLW-RE's were computed by the total energy of the fully delocalized wavefunction (Ψ_{deloc}) of the phenol ring considred minus that of a localized wavefunction (Ψ_{loc}), in which π-conjugation among the C=C π-bonds were artificially "turned off" (BLW-RE = $\Psi_{deloc} - \Psi_{loc}$). Ψ_{loc} is computed by partitioning all of the electrons and basis functions of the molecule considered into four subspaces ("blocks"): three for each of the π-C=C units (each block includes two π-electrons, as well as the p_z, d_{xz}, and d_{yz} basis functions for each carbon atom) and one for the remainder of the molecule (including the remaining electrons and basis functions); orbitals of the same subspaces are mutually orthogonal but orbitals of different subspaces overlap freely. Both Ψ_{deloc} and Ψ_{loc} are self-consistently optimized. All vertical BLW-RE computations were performed at B3LYP/6-31G(d)//ωB97XD/6-311+G(2d,p).

V.2.3. RESULTS AND ANALYSIS

The photoelectron spectrum of the phenolate anion, PhO^- is presented in Figure V.4(a). Three distinct bands are present. The $\nu' = 0 \leftarrow \nu'' = 0$ (origin) transition resides under the lowest EBE band. Our photoelectron spectrum of the phenolate anion is in agreement with those reported previously.[1-4] In extracting the electron affinity value from our photoelectron spectrum of the PhO^- anion, we benefited from previous anion photoelectron studies of PhO^-. Lineberger and co-workers[1] determined the EA(PhO) value to be 2.2530 ± 0.0060 eV; Fielding and co-workers[2] reported an EA(PhO) value of 2.15 ± 0.15 eV; Neumark and co-workers[3] assigned an EA(PhO) value of 2.25380 ± 0.00080 eV; and Wang and co-workers[4] determined EA(PhO) value to be 2.25317 ± 0.00037 eV. While our photoelectron spectrum of the PhO^- anion was recorded at lower resolution, it is fully consistent with those previously recorded, allowing us to locate the EBE value of its origin transition on the spectral profile observed in this study. Our computational EA(PhO) value of 2.16 eV is also in good agreement with the previously reported experimental values, validating our theoretical methods, but also providing a measure of the accuracy of those methods.

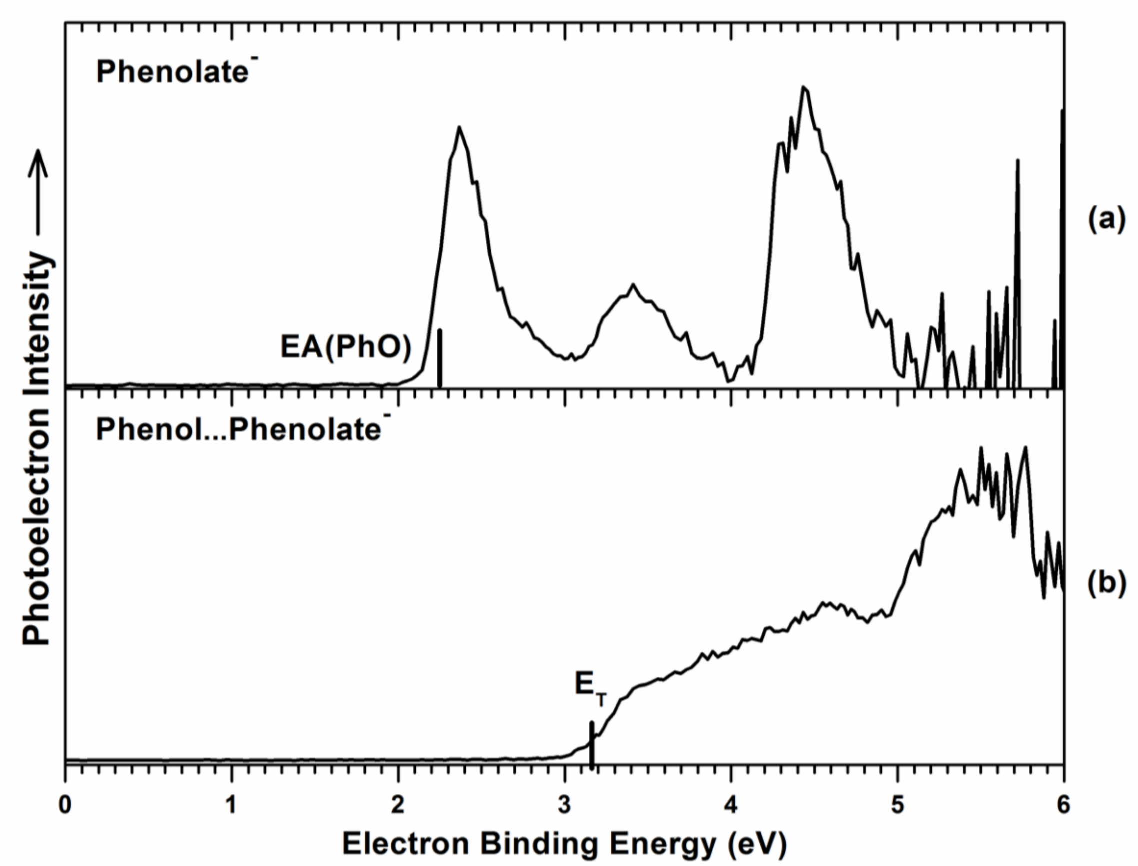

Figure V.4: Anion photoelectron spectra of (a) the phenolate anion and (b) the phenol-phenolate anionic complex. All spectra were calibrated against the photoelectron spectrum of Cu^-, the copper atomic anion.

The photoelectron spectrum of the phenol–phenolate anionic complex, $PhO^- \cdots HOPh$, is presented in Figure V.4(b). It exhibits at least two broad features, with the onset of the first transition occurring at 3.0 eV. Although an electron affinity cannot be confidently assigned to the $PhO^- \cdots HOPh$ anion spectrum, an empirical threshold value (E_T), based on a linear extrapolation of the steepest rise on the low EBE side of the lowest EBE band in the spectrum, was determined to be 3.16 eV ± 0.15 eV. Our calculated EA($(PhO)_2H$) value was 3.01 eV. This is consistent with our photoelectron spectrum of the $PhO^- \cdots HOPh$ anion, and it is close to our estimated threshold value.

In our previous LBHB work[26] we looked to the anion photoelectron studies of six hydrogen bihalide anions, HX_2^-, where X denoted both homogeneous and heterogeneous combinations of the halogen atoms, Cl, Br, and I, as guides for interpreting our photoelectron spectra and for extracting hydrogen bond strengths, i.e., $D(X^- \cdots HX)$, directly from them. The simpler hydrogen bihalide anions are in many ways analogous to more chemically complicated proton-coupled LBHB systems. Neumark and co-workers[27,28] found the $X \cdots HX$ neutral complexes, resulting from photodetachment of HX_2^-, to be unbound. Our computations involving the phenol-phenolate system, however, found the $PhO \cdots HOPh$ neutral complex to be bound by 0.36 eV. Thus, the sought-after hydrogen bond strength of the $PhO^-/HOPh$ couple cannot be estimated solely from the photoelectron spectral data.

The phenol-phenolate anion, hydrogen bond strength, $D(PhO^- \cdots HOPh)$, can be determined by inputting the calculated and/or experimental values presented above into the following energetic relationship:

$$D(PhO^- \cdots HOPh) = EA((PhO)_2H) + D(PhO \cdots HOPh) - EA(PhO) \qquad (1)$$

Using only calculated values for the quantities on the right side of this equation yields a $D(PhO^- \cdots HOPh)$ value of 1.21 eV (27.97 kcal/mol). This value is in excellent agreement with previous calculations performed at the composite CCSD(T) level with complete basis set (CBS) extrapolation (1.22 eV, 28.1 kcal/mol).[10] Substituting only the experimentally very well-determined EA(PhO) value of 2.25 eV in Eqn. (1) implies a $D(PhO^- \cdots HOPh)$ value of 1.12 eV (25.8 kcal/mol). Using the experimentally-determined values of both EA(PhO) and E_T, along with the computationally-derived value for $D(PhO \cdots HOPh)$, implies a $D(PhO^- \cdots HOPh)$ value of 1.27 eV (29.3 kcal/mol). All of these ways for finding

D(PhO$^{-}\cdots$HOPh), i.e., the phenol-phenolate anion, ionic hydrogen bond strength, imply that it is quite strong. Pertinent values and relationships are exhibited in in Figure V.5 and Table V.2.

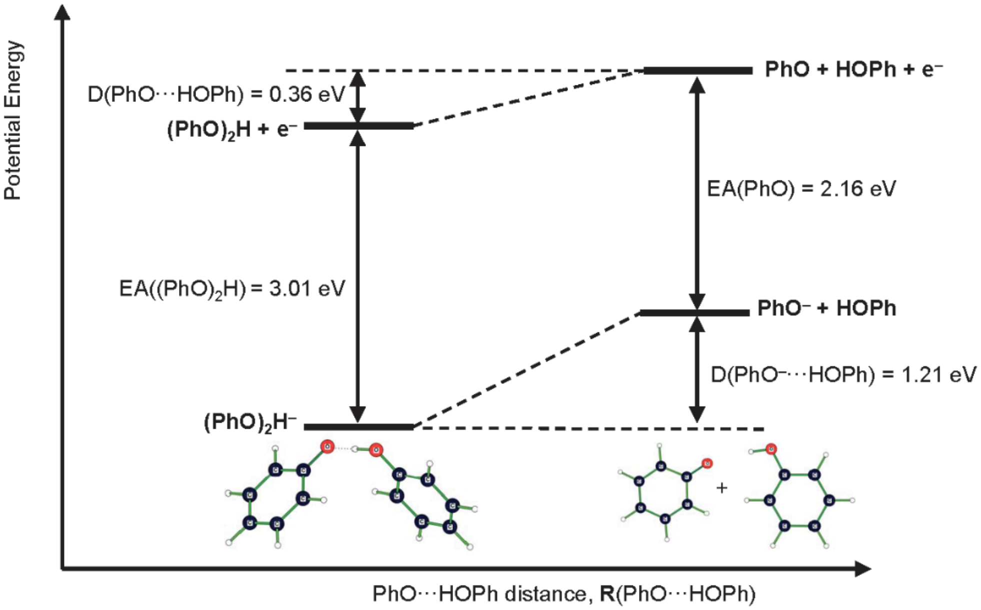

Figure V.5: Schematic illustration of the energetic relationships between EA(PhO), EA($(PhO)_2H$), D(PhO$\cdots$HOPh), and D(PhO$^{-}\cdots$HOPh) [all values include zero-point vibrational energy (ZPVE) and basis set superposition error (BSSE) corrections].

Table V.2: Computed EA(PhO), EA($(PhO)_2H$), and D(PhO$\cdots$HOPh) values[a] at ωB97XD/6-311+G(2d,p) [all values include zero-point vibrational energy (ZPVE) and basis set superposition error (BSSE) corrections]. The implied D(PhO$^{-}\cdots$HOPh) value provides a direct estimate of the PhO$^{-}\cdots$HOPh hydrogen bonding strength. Experimental values are listed in parenthesis for comparison.

EA(PhO)	EA ($(PhO)_2H$)	D(PhO$\cdots$HOPh)	D(PhO$^{-}\cdots$HOPh)
2.16	3.01	0.36	1.21
(*2.25*)[b]	(*$E_T = 3.16$*)	--	--

[a] All values are presented in units of electron volts (eV).

[b] Value taken from ref 4.

V.2.4. DISCUSSION

Since hydrogen bonds are expected to be at their strongest in the gas phase, the estimated phenol-phenolate anion hydrogen bond strength (26-30 kcal/mol) we report here represents the maximum interaction strength of the $PhO^{-}/HOPh$ couple in other environments. In the enzyme catalyzed reaction by ketosteroid isomerase (KSI), the dienolate intermediate is thought by some to be stabilized by a strong, low-barrier hydrogen bond (LBHB) involving a tyrosine hydroxyl (Tyr14) side chain. The $PhO^{-}/HOPh$ hydrogen bond, i.e, $PhO^{-} \cdots H^{+} \cdots {}^{-}OPh$, is a model for this interaction, and the interaction strength seen in this work suggests that it is a low barrier hydrogen bond.

The phenol/phenolate anion's hydrogen bond strength is ~60% of the hydrogen bond strength of HF_2^{-} (2.0 eV), the strongest known hydrogen bond.[26] This may seem surprising, since phenol is a very weak acid with a ~pK_a value of 10 (in water). What is responsible for its unexpected proton donating ability, and how can phenol form such strong hydrogen bonds? The answer lies in the increased ring π-resonance of the hydrogen-bonded phenol. In the $PhO^{-}\cdots HOPh$ complex, hydrogen bonds can polarize the π-electrons in the phenol ring, enhance its "phenolate-like" character (see Figure V.6, resonance structures on the right), and lead to increased π-electron delocalization. Note that increased π-conjugation does not necessarily reflect enhanced π-aromatic character. Upon hydrogen bonding, phenol exhibits increased net π-electron delocalization energy but reduced π-aromaticity, since the π-electrons are polarized towards the exocyclic C–O moiety (this reduces "cyclic" six π-electron character in the ring, see also resonance forms of the hydrogen bonded phenol in Figure V.6, right). The degree of π-resonance (RE) increase can be estimated directly through BLW computations (see Methods). Based on this procedure (see Figure

V.6, left), the three π-bonds in phenol can be localized into three “blocks” (each corresponding to a localized π-molecular orbital with two π electrons); this disables π-conjugation, and when compared to the energy of the fully π-electron delocalized wavefunction, provides a measure of the RE of phenol. Remarkably, the computed BLW-RE for the hydrogen-bonded phenol (BLW-RE: 117.5 kcal/mol, in PhO$^{-}\cdots$HOPh) is +9.6 kcal/mol greater than that of the free phenol monomer (BLW-RE: 107.9 kcal/mol). This “extra” stabilization is significant and may contribute to the stronger than expected PhO^{-} $\cdots$HOPh hydrogen bond strength.

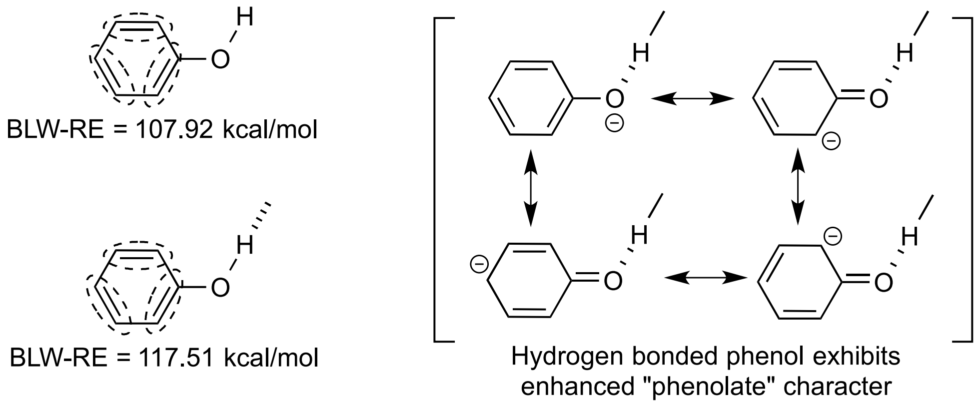

Figure V.6: (On the left) Computed vertical BLW-RE’s (in kcal/mol, at B3LYP/6-31G*) for the phenol monomer and hydrogen bonded phenol (in PhO$^{-}\cdots$HOPh). The dotted circles represent the three π-electron localized “blocks”; this BLW procedure disables π-conjugation in the ring and evaluates the π-RE’s of phenol rings considered (see Methods). (On the right) Resonance structures of hydrogen bonded phenol rings all display enhanced “phenolate” character.

The strength of the phenol-phenolate hydrogen bond is close to the previously measured gas-phase, intermolecular hydrogen bond strength of the proton-coupled pair imidazole-imidazolide (0.9 eV).[26] Imidazole is also a very weak acid with a ~pK_a value of 14 (in water). The hydrogen bond strength in the imidazole–imidazolide anionic complex, Im^{-}

⋯HIm, was estimated from the difference between the $E_T[H(Im)_2]$ and EA(Im). Given that the hydrogen bonding interaction, D(PhO⋯HOPh), in the neutral radical, Ph⋯HPh, was not negligible in the estimation of the PhO^-/HOPh hydrogen bond strength, we calculated the hydrogen bonding interaction of neutral Im⋯HIm and found it to be 0.29 eV. Thus, our previously reported value of 0.9 eV may be a lower limit to the hydrogen bond strength of the Im^-/HIm complex. A previous gas phase measurement of the dissociation energy of HIm_2^- reported a value of 1.1 eV.[29] Thus, a hydrogen bond strength that is slightly greater than 0.9 eV for the imidazole–imidazolide anionic complex would be reasonable and in good agreement with that measurement. In any case, the result of both the present work on PhO^-/HOPh and the previous work on Im^-/HIm is that the ionic hydrogen bond strengths of these enzymatically relevant models are very strong in the gas phase. If even a fraction of these hydrogen bond strengths were to be retained in enzyme active site environments, they might be able to facilitate enzymatic rate enhancements.

V.2.5. CONCLUSION

The hydrogen bonding in the phenol-phenolate anionic complex was studied experimentally using anion photoelectron spectroscopy and theoretically using density functional theory computations at the ωB97XD/6-311+G(2d,p) level. The computed and experimentally-derived phenol-phenolate anion hydrogen bond strengths agree and are rather considerable. The unexpectedly strong bonding in the PhO^-⋯HOPh complex may be due to increased π-electron delocalization stabilization in the phenol ring.

ACKNOWLEDGEMENTS

This material is based on work supported by the National Science Foundation under Grant Numbers, CHE-1360692 (KHB) and CHE-1057466 (JIW).

REFERENCES

1. R. F. Gunion, M. K. Gilles, M. L. Polak and W. C. Lineberger, *Int. J. Mass. Spectrom. Ion Processes*, 1992, **117**, 601.

2. A. R. McKay, M. E. Sanz, C. R. S. Mooney, R. S. Minns, E. M. Gill and H. H. Fielding, *Rev. Sci. Instrum.*, 2010, **81**, 123101.

3. J. B. Kim, T. I. Yacovitch, C. Hock and D. M. Neumark, *Phys. Chem. Chem. Phys.*, 2011, **13**, 17378.

4. H.-T. Liu, C.-G. Ning, D.-L. Huang, P. D. Dau and L.-S. Wang, *Angew. Chem. Int. Ed.*, 2013, **52**, 8976.

5. J. D. Steill, A. L. May, S. R. Campagna, J. Oomens and R. N. Compton, *J. Phys. Chem. A*, 2014, **118**, 8597.

6. T. B. McMahon and P. Kebarle, *J. Am. Chem. Soc.*, **1977**, 99, 2222.

7. J. E. Bartmess, J. A. Scott, R. T, McIver, Jr. *J. Am. Chem. Soc.*, 1979, **110**, 6046.

8. D. F. McMillen and D. M. Golden, *Ann. Rev. Phys. Chem.*, 1982, **33**, 493.

9. R. M. Borges dos Santos and J. A. M. Simoes, *J. Phys. Chem. Ref. Data*, 1998, **27**, 707.

10. M. Kolaski, A. Kumar, N. J. Singh and K. W. Kim, *Phys. Chem. Chem. Phys.*, 2011, **13**, 991.

11. T. M. Krygowski and H. Szatylowicz, *J. Phys. Chem. A*, 2006, **110**, 7232.

12. A. K. Chandra and T. Uchimaru, *Int. J. Mol. Sci.*, 2002, **3**, 407.

13. A. Surjoosingh, S. Hammes-Schiffer, *J. Phys. Chem. A,* 2011, **115**, 2367-2377.

14. P. J. Lodi and J. R. Knowles, *Biochemistry*, 1991, **30**, 6948.

15. J. A. Gerlt and P. G. Gassman, *J. Am. Chem. Soc.*, 1993, **115**, 11552.

16. W. W. Cleland and M. M. Kreevoy, *Science*, 1994, **264**, 1887.

17. P. A. Frey, S. A. Whitt and J. B. Tobin, *Science*, 1994 **264**, 1927.

18. W. Childs and S. G. Boxer, *Biochemistry*, 2010, **49**, 2723.

19. Q. Zhao, C. Abeygunawardana, P. Talalay, and A. S. Mildvan, *Proc. Natl. Acad. Sci.*, 1996, **93**, 8220.

20. O. C. Thomas, W. J. Zheng, and K. H. Bowen, *J. Chem. Phys.*, 2001, **114**, 5514.

21. J.-D. Chai and M. Head-Gordon, *Phys. Chem. Chem. Phys.* 2008, **10**, 6615.

22. R. Krishnan, J.S. Binkley, R. Seeger and J.A. Pople, *J. Chem. Phys.* 1980, **72**, 650.

23. S. Simon, M. Duran, and J. J. Dannenberg, *J. Chem. Phys.*, 1996, **105**, 11024.

24. Gaussian 09, Revision **D.01**, M. J. Frisch, G. W. Trucks, H. B. Schlegel, G. E. Scuseria, M. A. Robb, J. R. Cheeseman, G. Scalmani, V. Barone, B. Mennucci, G. A. Petersson, H. Nakatsuji, M. Caricato, X. Li, H. P. Hratchian, A. F. Izmaylov, J. Bloino, G. Zheng, J. L. Sonnenberg, M. Hada, M. Ehara, K. Toyota, R. Fukuda, J. Hasegawa, M. Ishida, T. Nakajima, Y. Honda, O. Kitao, H. Nakai, T. Vreven, J. A. Montgomery, Jr., J. E. Peralta, F. Ogliaro, M. Bearpark, J. J. Heyd, E. Brothers, K. N. Kudin, V. N. Staroverov, R. Kobayashi, J. Normand, K. Raghavachari, A. Rendell, J. C. Burant, S. S. Iyengar, J. Tomasi, M. Cossi, N. Rega, J. M. Millam, M. Klene, J. E. Knox, J. B. Cross, V. Bakken, C. Adamo, J. Jaramillo, R. Gomperts, R. E. Stratmann, O. Yazyev, A. J. Austin, R. Cammi, C. Pomelli, J. W. Ochterski, R. L. Martin, K. Morokuma, V. G. Zakrzewski, G. A. Voth, P. Salvador, J. J. Dannenberg, S. Dapprich, A. D. Daniels, Ö. Farkas, J. B. Foresman, J. V. Ortiz, J. Cioslowski, and D. J. Fox, Gaussian, Inc., Wallingford CT, 2009.

25. Y. Mo, L. C. Song and Y. C. Lin, *J. Phys. Chem. A*, 2007, **111**, 8291.

26. J. D. Graham, A. M. Buytendyk, D. Wang, K. H. Bowen and K. D. Collins, *Biochemistry*, 2014, **53**, 344.

27. R. B. Metz, A. Weaver, S. E. Bradforth, T. N. Kitsopoulos, and D. M. Neumark, *J. Phys. Chem.*, 1990, **94**, 1377.

28. S. E. Bradforth, A. Weaver, D. W. Arnold, R. B. Metz, D. M. Neumark, *J. Chem. Phys.*, 1990, **92**, 7205.

29. Meot-Ner (Mautner), M. *J. Am. Chem. Soc.*, 1988, **110**, 3075.

Chapter VI: APPENDIX

VI.1. Pulsed Instrument Building Improvements

VI.1.1. NEW EXTRACTION CHAMBER

In the previous pulsed source apparatus instrument setup (see Figure I.1), ions were both created and extracted in the same chamber. This arrangement limited the types of anionic species that could be produced. A new chamber was designed (by J&A) which houses a separate differrentially pumped "box" where the Wiley-McLaren type pulsed extraction region is located (Figure VI.1). It was also designed to have 3 axes intersect within a 1 mm point in the center of the extraction region, between the Wiley-McLaren plates.

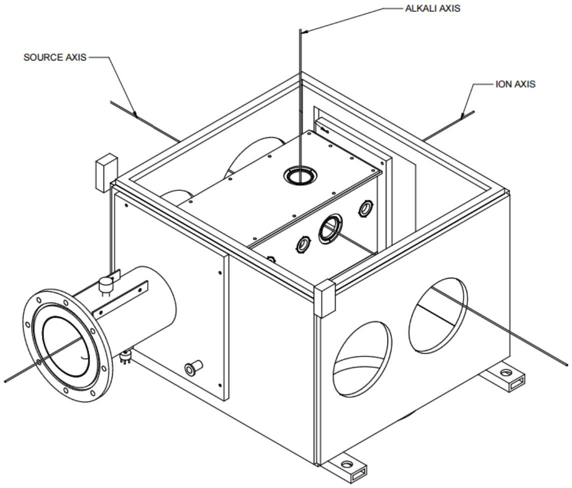

Figure VI.1: New extraction chamber with internal box showing alignment axes.

This new extraction chamber was attached to the existing instrument in place of the source chamber while the source chamber was then rotated by 90 degrees and carefully coupled to the new chamber (Figure VI.2). Once the chambers were successfully joined, the new extraction chamber vacuum system, consisting of 2 sets of gate valves, liquid nitrogen baffles, and VHS-6 diffusion pumps, were assembled and painstakingly helium leak tested until the vacuum system reached 2.3 x 10^{-7} Torr. The chamber was fabricated by the Kurt J. Lesker Company and all design plans can be found on the Bowen Fileserver in the PSA documents. Also, see Jacob Graham's Thesis for more details.

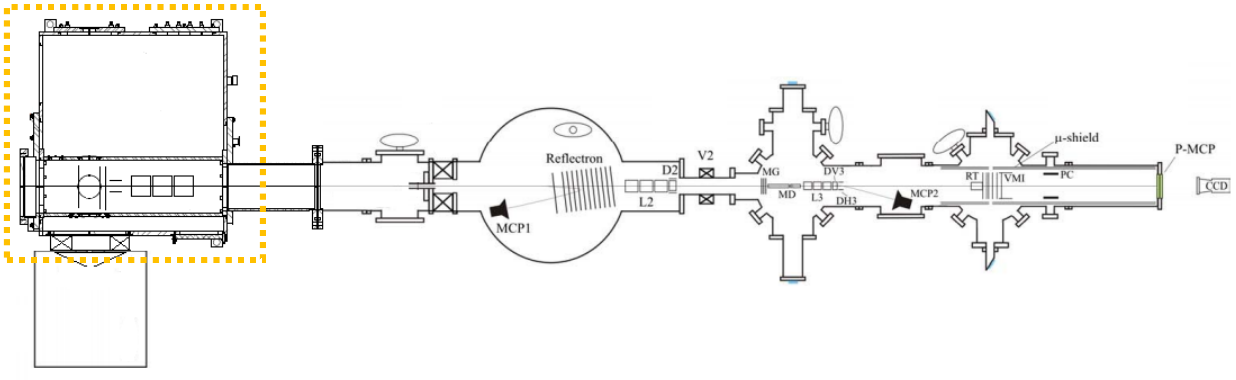

Figure VI.2: Schematic diagram of the pulsed photoelectron spectrometer with new extraction chamber. Dotted-line box highlights new extraction chamber.

VI.1.2. ALKALI OVEN

A major feature that was also incorporated during the design process of the new extraction chamber was making space beneath it for a smaller chamber to house an alkali oven source. The source is mounted on the bottom flange of the smaller chamber attached to Ch.1. The following concentric parts make up the source, starting from the center outward: a stainless steel oven (where the alkali metal is loaded), a ceramic threaded tube wrapped with tantalum wire which serves as the heater, a tantalum shield surrounding the heater to keep the temperature uniform around the heater and oven, and lastly, a water cooled jacket that helps to keep the alkali from condensing on the chamber walls to minimize clean up.

Stainless Steel Oven – 304 SS Tube with 1.0" OD, 0.87" ID, 0.065" Wall (McMaster Carr). The oven was designed with a false bottom so it would sit on a disk holder, to minimize heat sinking of the oven. The cap of the oven is secured by a press fit, using either a hydraulic press or forced on by hand (Figure IV.3). Over time, the metal oven will expand slightly, due to heat cycling, and the press fit for the cap and oven will have to be modified. The cap has a tapped 8-32 thread hole for a vented screw (~1 mm hole) and is the orifice/nozzle for the thermal expansion of alkali. Construction of the oven and cap were done by Consolidated Instruments (Michael Kratfel). (Figure VI. 4a)

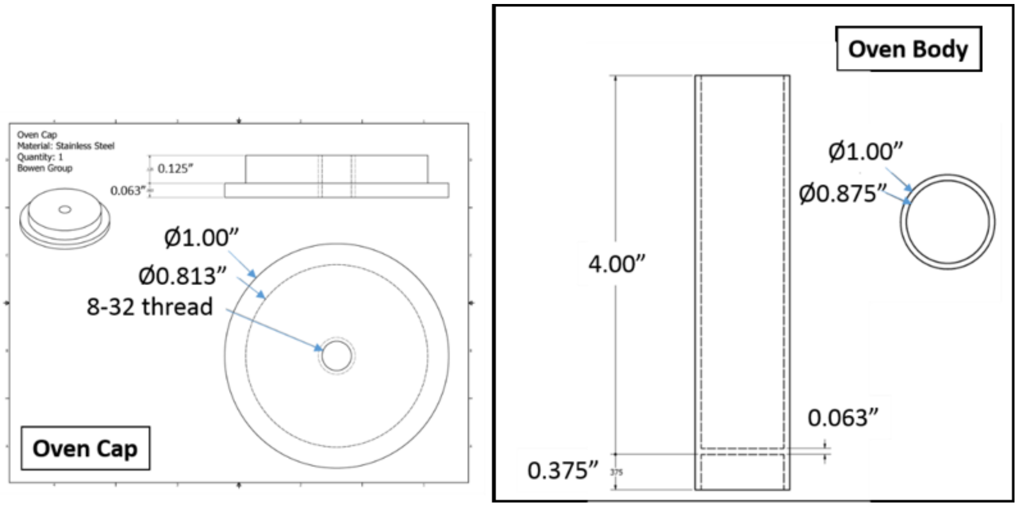

Figure VI.3: Schematic drawings of the alkali oven and cap.

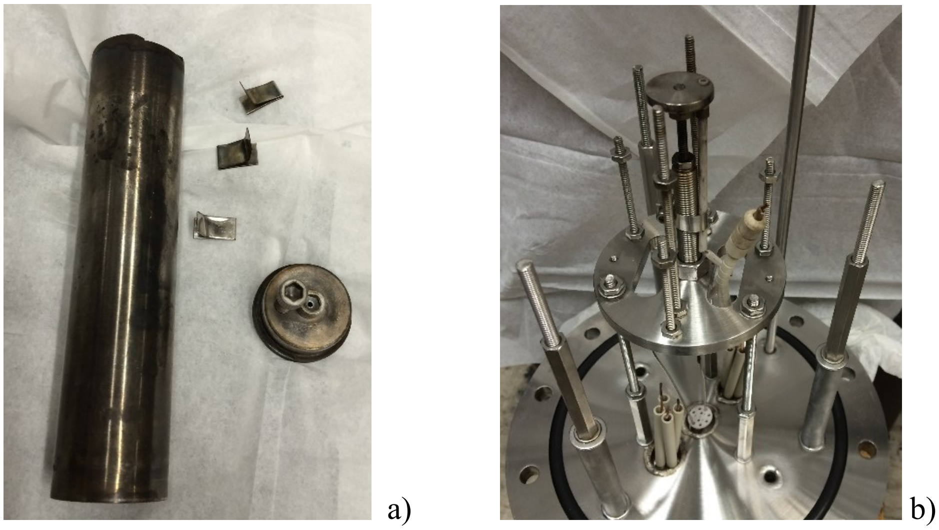

a) b)

Figure VI.4: a) Alkali oven with cap. The shims pictured are placed between the oven and ceramic heater to keep the oven vertical (see ceramic heater section). The cap has another 8-32 tapped hole off center if helium seeding is desired. b) Alkali oven flange with mounts. The flat disk, center, is the holder the false bottom of the oven sits on.

Ceramic Heater – A ceramic tube with OD 38 mm, ID 29 mm, Length 127 mm (Friatec, Part #: F281-11038-0127). The ceramic tube is wrapped with tantalum wire (0.020" diameter, ThermoShield) which sits in the threaded grooves on the tube (~6 Ω). The wire is secured at the top with self-made clamps from stainless steel shim (316 SS, 0.01" thick, McMaster Carr) and screws/nuts (Figure VI.5). The clamp at the bottom of the heater both secures the wire and serves as the holder for the oven (McMaster Carr P/N: 9633T28). Two through holes for 6-32 threaded rods were drilled 180° apart in the clamp. The threaded rods are then used to mount the heater to a platform which is mounted to the flange. The oven does not fit snuggly in the heater to allow room for heat expansion, thus, three shims are placed in between the oven and the heater to keep the oven straight in the source.


a) b)

Figure VI.5: a) Ceramic heater for the alkali oven, wrapped with tantalum wire. b) Picture of ceramic heater mounted on the source flange.

Heat Shield – Tantalum (99.95%) foil 0.003” x 6.0” x 10.5” (ThermoShield). The tantalum is wrapped into a 3” diameter circle (spotted welded closed) and is 6” in height (Figure VI.6). Three tabs were made from stainless steel shim material and hole punched for a size 6 screw. The tabs were then spot welded to the tantalum. The purpose of the heat shield is to help keep in the radiant heat and help maintain a uniform temperature for the alkali oven.

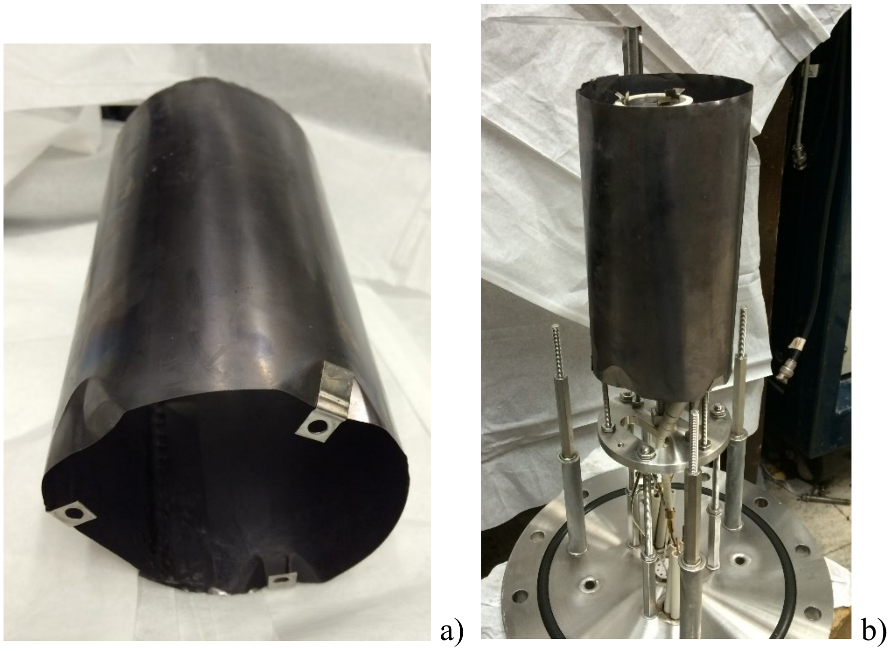

Figure VI.6: a) Tantalum heat shield with tabs for mounting. b) Tantalum shield sitting on flange mount assembly.

Water Jacket –Two stainless steel (SS 304) cylinders (5.00” and 3.50” OD, 1/8” thick, 7” Height) are welded together with 1/8” thick stainless steel (SS 304) sheet to create a closed cylinder between the 5” and 3” diameter space. Two 0.25” stainless steel (SS 304) tubes are welded 180° from each other on the bottom of the cylinder for inlet/outlet water outlets. The inlet tube was inserted ~1” away from the top of the cylinder while the outlet tube was welded to the bottom. Three mounting tabs are welded and spaced 120° on the bottom of the water jacket. A size 10 through hole in the tab allows for the water jacket to sit on threaded posts when assembled on the source flange (Figure VI.7, JHU Machine Shop).

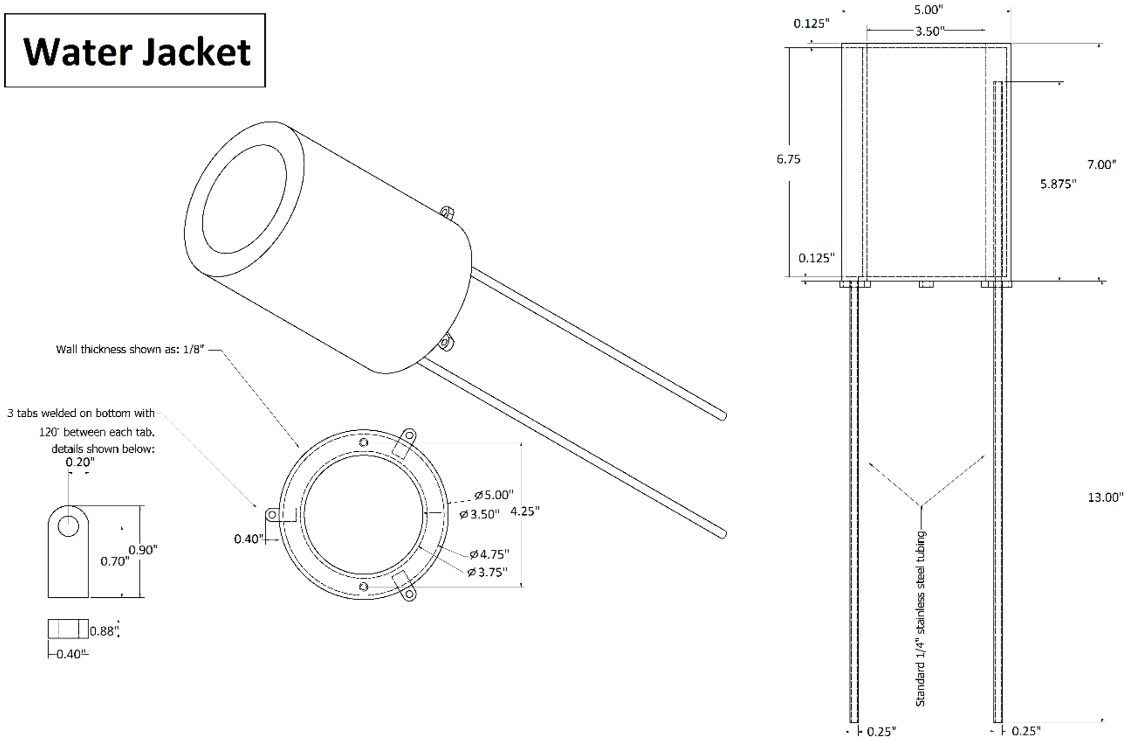

Figure VI.7: Schematic of the water jacket on the alkali oven source.


a) b)

Figure VI.8: a) Water jacket, looking beneath. b) Water jacket mounted on source flange.

The main purpose of the jacket is to serve as a vehicle for alkali vapor to condense and minimize the alkali from condensing on the vacuum chamber walls. This helps minimize alkali clean up when the source has to be removed. Two additional elements are added to collect stray alkali vapor 1) a copper disk which sits on the water jacket and 2) a beam flag. The copper disk (~0.25” thick) has a 0.5” hole drilled through the center which is enough for the thermal effusive beam to pass through but still minimize alkali collecting on the gate valve between the alkali chamber and C 1 of the instrument. Three tabs made out of stainless steel are used to keep the plate for moving due to vibrations. The beam flag is made out of ~0.1” stainless steel and attached to a 0.25” rod which fits through an ultra-torr connection welded on the source flange. A knob is attached to the end of the rod so the flag can easily be moved during the experiment. When the alkali oven in heating and not being used the flag is turned to cover the opening in the copper plate to, again, minimize the collection of alkali vapor on the gate valve (Figure VI.9).

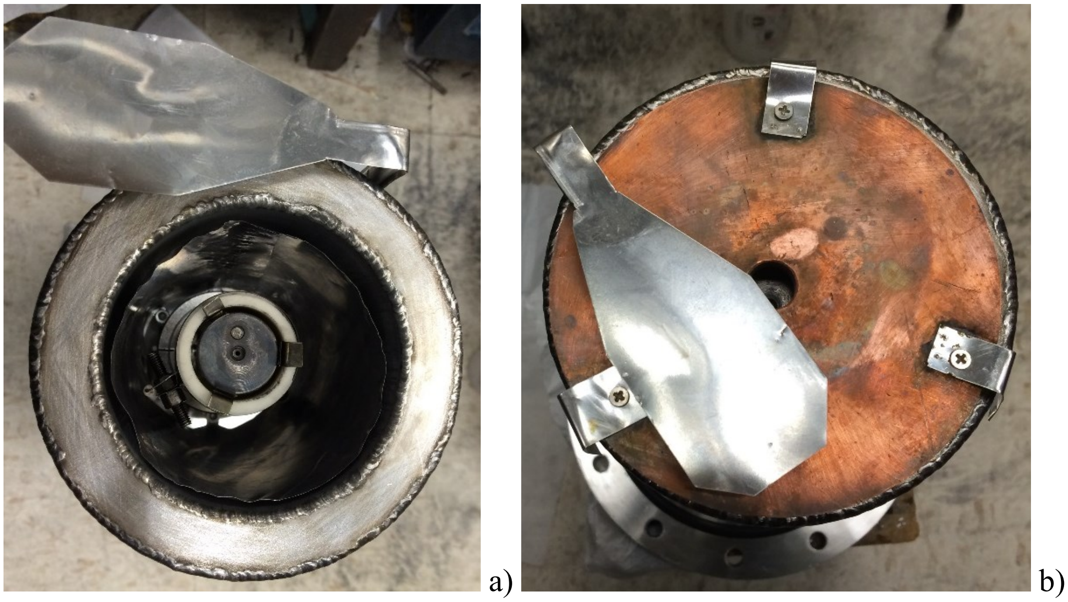

Figure VI.9: a) View looking down the alkali oven source with the oven, heater, shield, water jacket, and beam flag in place. b) View looking down alkali oven source with copper plate in place and beam flag almost covering the beam.

Feedthrough Flange – Two 4 pin feedthroughs made of copper, insulted by alumina ceramic, rated for 6kV and 27 Amps (CeramTec, P/N: 9216-08-W) are welded on the two outer 0.75” diameter holes show in Figure VI.10. The middle 0.75” diameter hole has one Type K thermocouple (TC) pair, Chromel/Alumel, (CeramTec, P/N: 8117-01-W) feedthrough welded in place, (Machining and welding by Consolidated Instruments, Michael Kratfel). Current is delivered to the ceramic heater through 2 of the pins where beryllium-copper push-ons are used to attach to the copper feeds. Additional feedthroughs were added for a future charge transfer experiment which would involve a biased filament, a lens and deflectors.

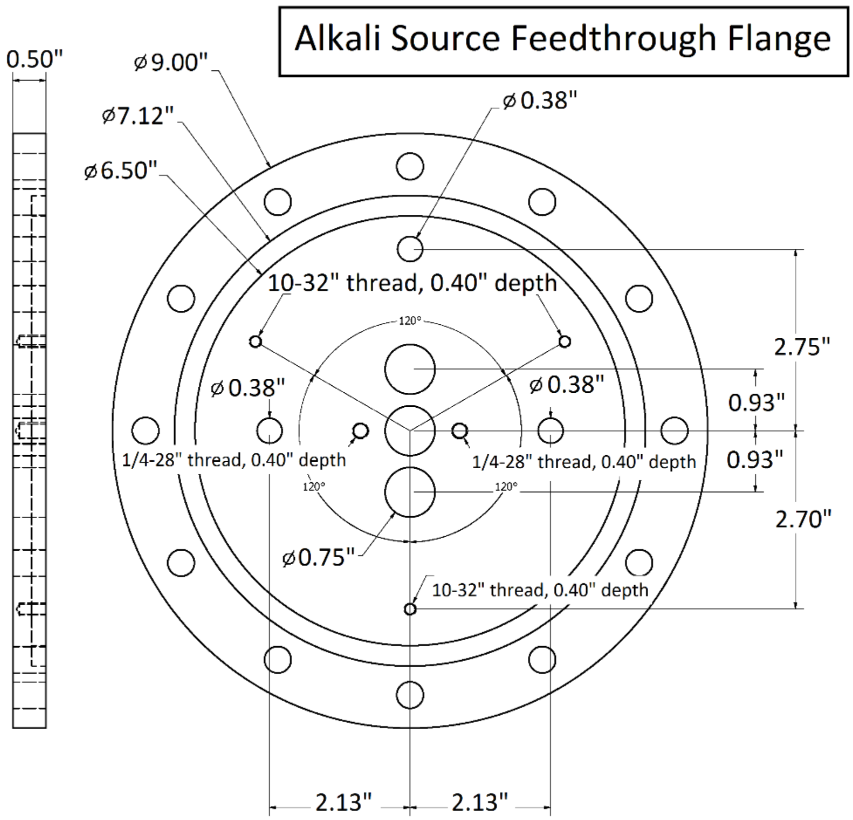

Figure VI.10: Schematic of feedthrough flange of alkali oven source.

Table VI.1: Alkali Thermocouple Calibration

Reading (mv)	**Temp** (°C)
-0.08	20
0.76	40
1.60	60
2.45	80
3.29	100
4.14	120
4.98	140
5.82	160
6.67	180
7.51	200
8.35	220
9.20	240
10.04	260
10.89	280
11.73	300
12.57	320
13.42	340
14.26	360
15.11	380
15.95	400

Chart VI.1: Alkali Thermocouple Calibration

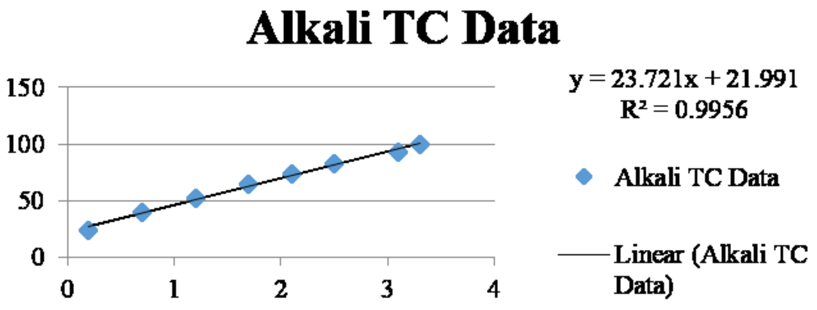

The three 10-32" threaded tapped holes are where the threaded rod support for the water jacket are attached. The two 0.38" holes which are 180° apart are where two ulta-torr connections are welded for the 0.25" inlet and outlet tubes of the water jacket to exit the chamber. The other 0.38" hole is for the 0.25" rod for the beam flag. The two 1/4-28" threaded tapped holes are for threaded rods which attach to the mounting plate which holds the oven, heater, and heat shield.

Alkali Platform – Stainless steel (SS 304) plate for mounting the alkali oven, heater, and shield (Consolidated Instruments). The platform is attached to the bottom of the feedthrough flange using the three 0.20" through holes and threaded rods/nuts (Figure VI.11). The center 3/8-24" threaded hole is for a threaded rod with a disk to support the alkali oven (Figure VI.11 and Figure VI.4b). The false bottom of the welded alkali oven fits snuggly on the disk which is attached to the threaded rod. The disk has a small hole for the thermocouple, which is insulated by a ceramic tube. Material on the threaded rod has been removed to minimize heat sinking from the contact of the false bottom with the disk. The pair of 6-32" threaded through holes (inside the diameter of the 0.20" holes) is used to hold the bottom clamp of the alkali oven heater with threaded rods and nuts. The ceramic beaded wires on the heater, which attach to the feedthoughs, are placed in between the 0.50" rectangular cut outs. The three 6-32" threaded through holes, in the same radius of the 0.20" holes but opposite by 180°, are used to hold the heat shield where threaded rods fit through the hole punched tabs, spot-welded to the tantalum, and are secured with nuts. An additional pair of 6-32" threaded through holes, in the same radius of the 0.20" holes but opposite by 180° the other pair of 6-32" threaded holes which support the heater, was made for a larger heater/clamp assembly for the future charge transfer experiment.

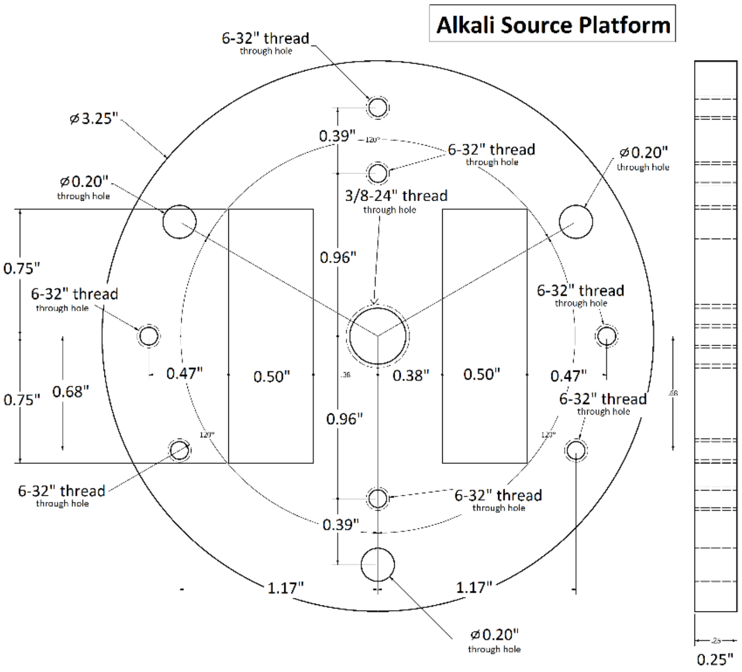

Figure VI.11: Alkali source platform for mounting the oven, heater, and shield.

VI.2. Rydberg Electron Transfer

OVERVIEW

The alkali oven source provides a method for gently producing anions through Rydberg electron transfer (RET). A beam of alkali atoms (potassium) are made in the alkali oven source below the internal box and pass through the Wiley-McLaren extraction plates. From the top and side of Ch.1, light from two dye lasers (frequency dependent based on the alkali metal), light from one laser in each direction, are used to pump and then excite potassium atoms to a desired Rydberg level. When the excited alkali atoms collide with a beam of neutral molecules from the source chamber (supersonic expansion from the pulsed valve), the outer Rydberg electron from the alkali atom is donated, creating molecular anions from the collisional charge transfer process. The resulting anions, produced in the center of the Wiley-McLaren extraction plates, are then pulsed down the time-of-flight tube and can be analyzed using photoelectron spectroscopy. Potassium was chosen because it is less flammable in air compared to the other alkali metals. Also, the frequencies necessary to excite potassium to the $^2P_{3/2}$ state (766.7 nm) and then to the Rydberg level (between 453-480 nm) are easy to achieve with lasers we have available; one Quanta Ray PDL-2 dye laser (using LDS 751) pumped by the 2nd harmonic of a Nd:YAG and one Quanta Ray PDL-2 dye laser (using Coumarin 460 or 480) pumped by the 3rd harmonic of a Nd:YAG. For more information about the laser set-up refer to Jacob Graham's thesis (2015).

VI.2.1. ALKALI OVEN SETTINGS

Approximately 6 grams of potassium can fit in the alkali oven. Potassium lumps in mineral oil (98%, Sigma 244864-50G) are used, where the sides of the alkali exposed to the mineral oil are sliced off using a clean razor blade, which can be done on a clean/dry surface in the fume hood. The potassium does not appear to oxide visibly in air and we have not observed any experimental issues preparing the sample in this manner. Based on previous alkali experiments in the literature, we desired a vapor pressure of ~10^{-2} Torr of potassium from the alkali source.[1,2] After several heating versus intensity test experiments with SF_6^- anion mass signal (made by RET), we determined the signal intensity starts to plateau after the oven reaches ~150 °C (5.5 mV TC reading). We also found that gradually heating (~1 hour) the source to the desired temperature is ideal. Otherwise, if the oven heats too quickly, there is potential for the ceramic heater to break. Also, we have found that heating in less than an hour causes the majority of the potassium to escape, clogging the nozzle, and depositing on the gate valve due to a phenomenon with alkali metal called "spritzing".

Reference

1. Struve, W. S.; Krenos, J. R.; McFadden, D. L.; Herschbach, D. R. *J. Chem. Phys.* **1975**, *62*, 404.

2. Nalley, J. S.; Compton, R. N.; Schweinler, H. C.; Anderson, V. E. *J. Chem. Phys.* **1972**, *59*, 4125.

VI.2.2. RET EXPERIMENTS

One advantage of RET is the ability to not only make valance bound anions but also dipole-bound anions. Both theoretical and previous experimental studies (including by RET) have shown that a molecule, in a low-lying rotational state, with a dipole moment greater than ≈ 2.5 D, can bind an excess electron. Many anions, including dipole-bound species, have been made by RET on the re-designed pulse apparatus, observed mass spectrally, and some have been analyzed by photoelectron spectroscopy. One nice experimental feature of RET is that since it is a gentile process, mass spectra are typically very clean, with only the peaks of the molecules of interest (assuming a clean system) since the photons used only excite electrons (i.e. do not photofragment the neutral).

VI.2.2.1 Sulfur Hexafluoride$^-$

Sulfur hexafluoride (SF_6^-) is one of the easiest (valence bound) molecules to make by RET and is primarily used as a test system to insure everything is working properly. Typically, a gas mixture of 10% SF_6 in Helium is made and about 30 psia backing pressure is placed behind the pulse valve (Parker, Series 9 General Valve, 0.79mm orifice).

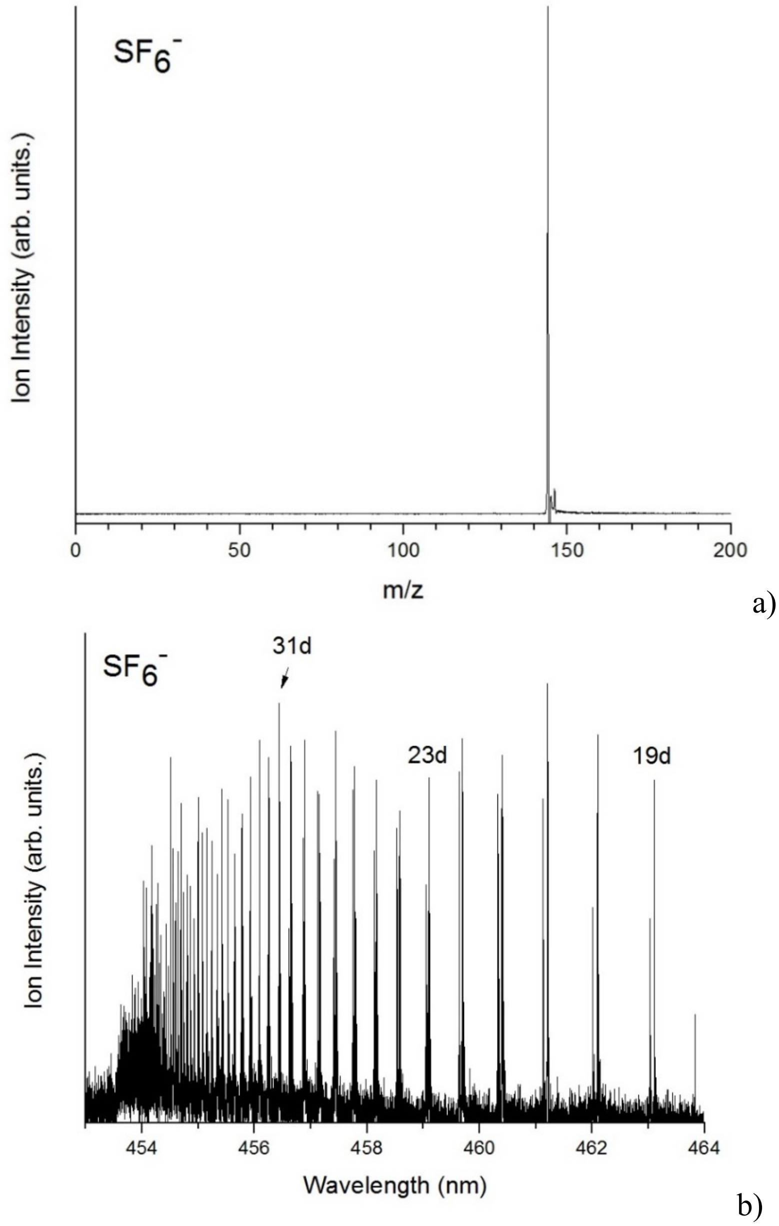

Figure VI.12: a) Mass spectrum of SF_6^- anion made by RET at one Rydberg level (top) and b) over multiple Rydberg levels (bottom).

Cluster anions ($(SF_6^-)_{n=1-3}$) are more difficult to make by RET and require higher pressure ~120 psia and use of a smaller orifice pulse valve (0.10 mm).

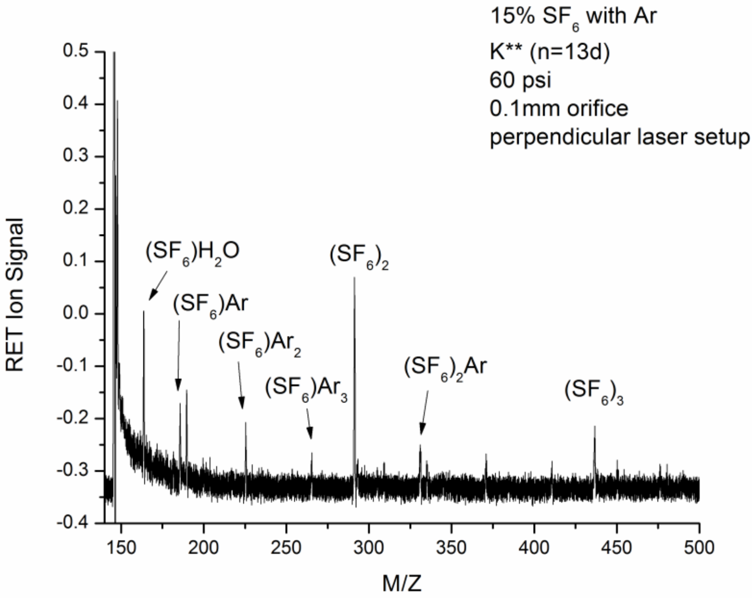

Figure VI.13: Mass spectrum of $(SF_6)_n^-$ anion clusters made by RET.

VI.2.2.2 Sulfur Dioxide⁻

The valence bound anion of sulfur dioxide anion $(SO_2)^-$ and cluster anions of $(SO_2)^-_{n=1-4}$ were made by RET by expanding a gas mixture of ~10% SO_2^- in Helium (~30 psia).

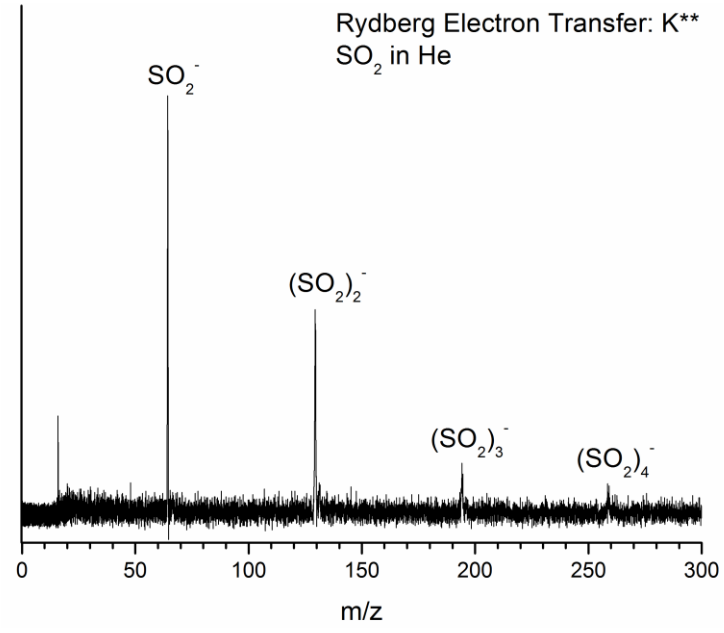

Figure VI.14: Mass spectrum of SO_2^- anion and clusters made by RET.

VI.2.2.3 Nitric Oxide⁻

The valence bound anion of nitric oxide anion $(NO)^-$ and cluster anions of $(NO)^-_{n=1-2}$ were made by RET by expanding a gas mixture of ~10% NO in Helium (~30 psia).

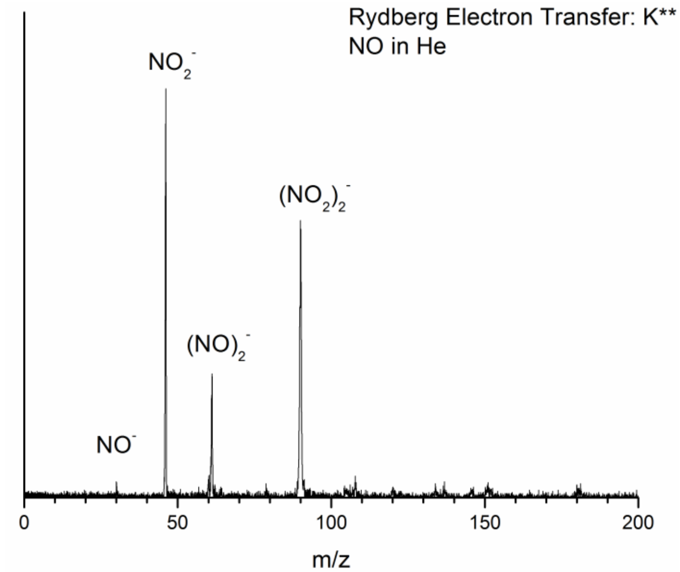

Figure VI.15: Mass spectrum of NO^- anion and clusters made by RET.

VI.2.2.4 Ammonia Clusters⁻

The valence bound anion of ammonia cluster anions of $(NH_3)^-_{n=39-52}$ were made by RET by expanding a gas mixture of ~10% NH_3 in Helium (~ 30 psia).

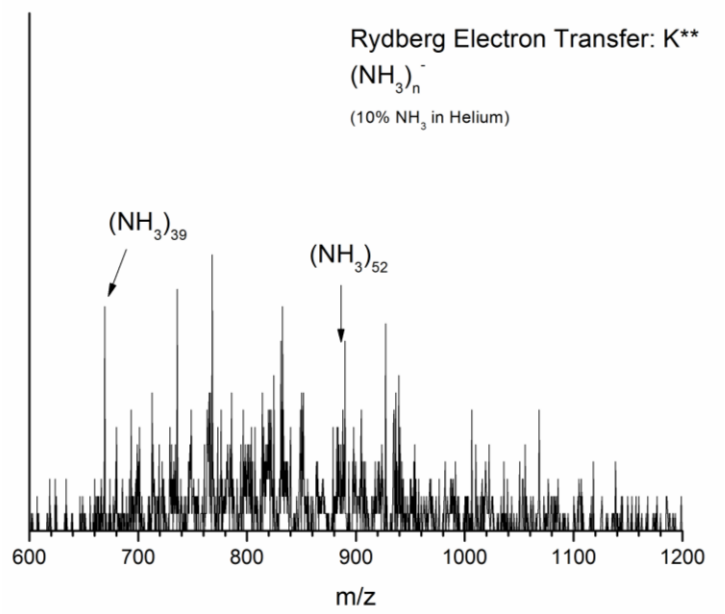

Figure VI.16: Mass spectrum of NH_4^- anion and clusters made by RET.

VI.2.2.5 Oxalic Acid⁻

The valence bound anion of oxalic acid ($C_2H_2O_4^-$) molecule was made by RET by adding a small amount of solid sample, heating the pulse valve to ~60 °C and expanded with ~30 psia of Helium.

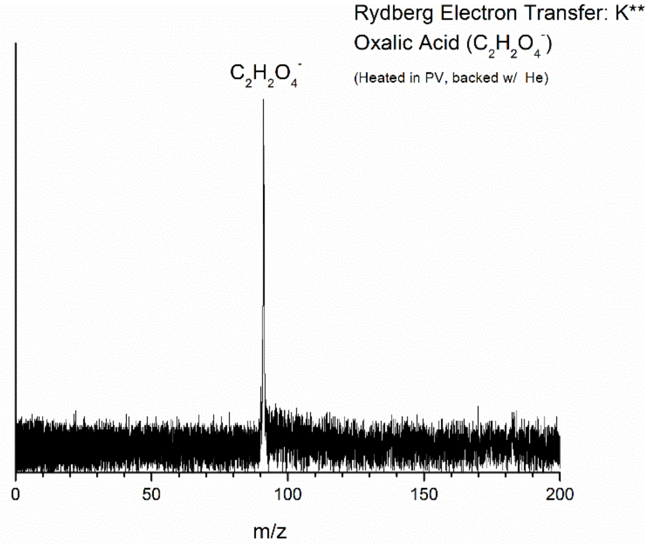

Figure VI.17: Mass spectrum of oxalic acid⁻ anion made by RET.

VI.2.2.6 Quinoline⁻

The valence bound anion of quinoline ($C_9H_7N^-$) molecule was made by RET by adding a few drops in the pulse valve and backing with ~30 psia of Helium.

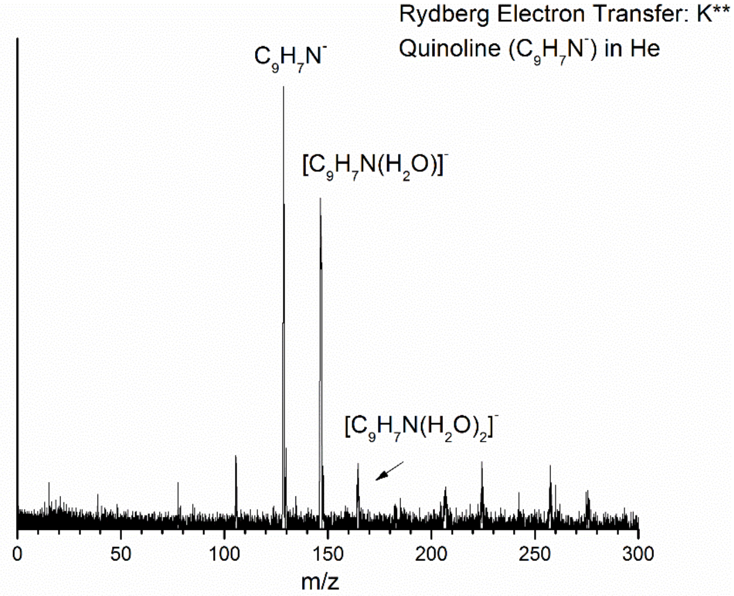

Figure VI.18: Mass spectrum of quinoline⁻ anion made by RET, either the sample or gas line was contaminated with water.

VI.2.2.7 Nitrobenzene$^-$

The valence bound anion of nitrobenzene ($C_6H_5NO_2^-$) molecule was made by RET by adding a few drops in the pulse valve and backing with ~30 psia of Helium.

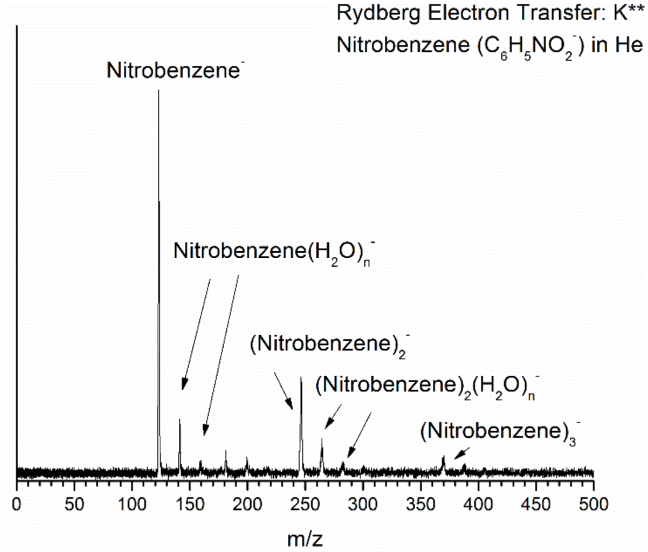

Figure VI.19: Mass spectrum of nitrobenzene$^-$ anion and clusters made by RET, either the sample or gas line was contaminated with water.

VI.2.2.8 Benzaldehyde$^-$

The valence bound anion of benzaldehyde ($C_7H_6O^-$) molecule was made by RET by adding a few drops in the pulse valve and backing with ~30 psia of helium.

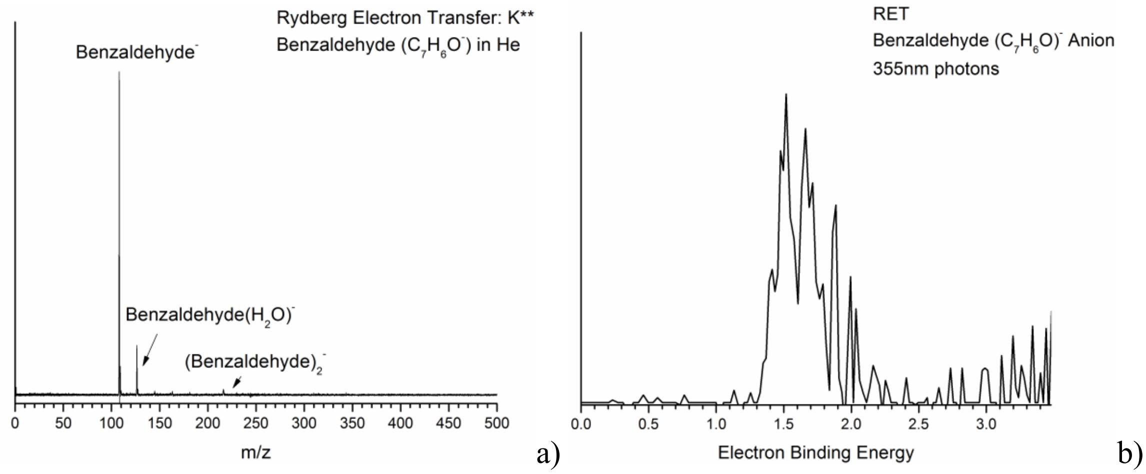

Figure VI.20: a) Mass spectrum of benzaldehyde$^-$ anion made by RET, either the sample or gas line was contaminated with water. b) PES of benzaldehyde$^-$ anion using magnetic bottle using 3.49 eV photons.

VI.2.2.9 Water Clusters$^-$

Water (H_2O^-) is the easiest cluster anion system to make. A few drops of water are added to the pulse valve (0.79 mm) and backed with ~5-30psia of helium. At best, the intensity of the strongest water cluster made by RET (levels 19d – 24d) is only about 1/3 as intense as the strongest water cluster made by laser/photoemission.

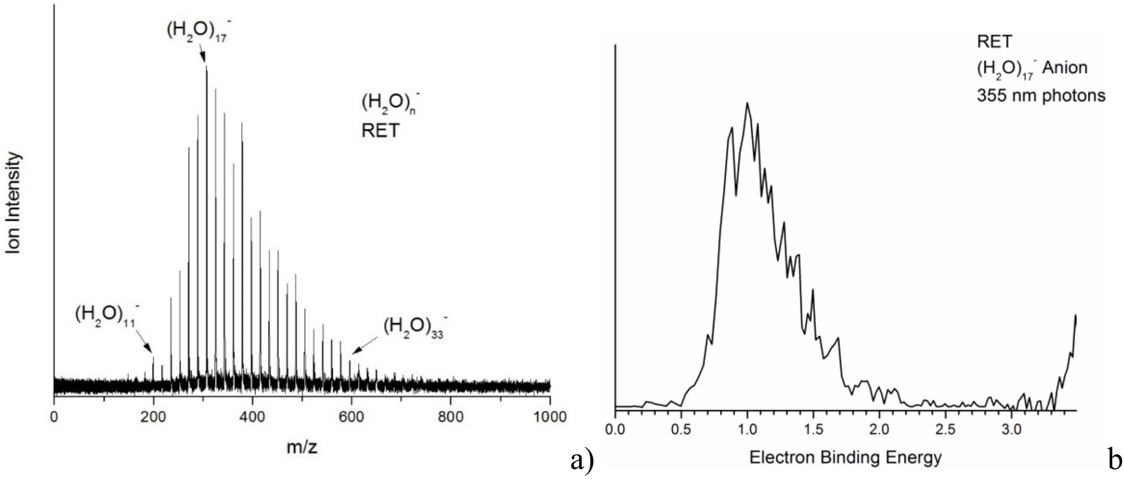

a) b)

Figure VI.21: Mass spectrum of $(H_2O)_n^-$ anion clusters made by RET and b) PES of $(H_2O)_{17}^-$ anion using magnetic bottle.

Water dimer is a dipole bound anion formed over the potassium Rydberg levels 11d-15d.

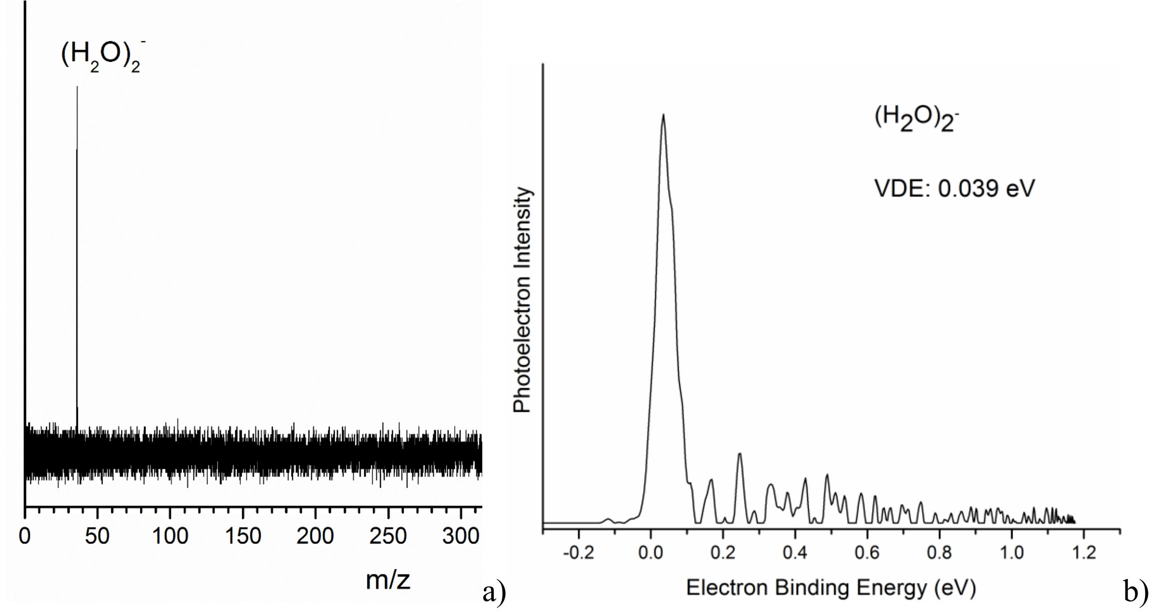

a) b)

Figure VI.22: a) Mass spectrum of $(H_2O)_2^-$ anion made by RET and b) PES of $(H_2O)_2^-$ anion using VMI.

VI.2.2.10 Thymine⁻

The dipole bound anion of the nucleobase molecule thymine ($C_5H_6N_2O_2^-$) was made by RET by adding a small amount of solid sample, heating the pulse valve to ~100 °C and expanded with ~30 psia of Helium.

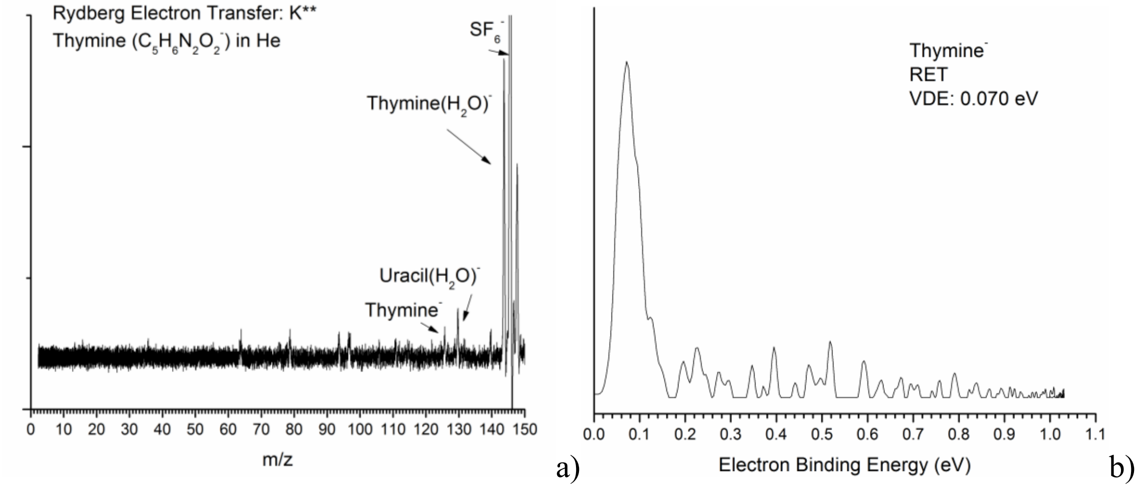

Figure VI.23: a) Mass spectrum of thymine⁻ dipole bound anion made by RET and b) PES of thymine⁻ anion using VMI.

VI.3. Acetonitrile Anion (CH_3CN^-) made by RET

VI.3.1. EXPERIMENTAL

Anion photoelectron spectroscopy is conducted by crossing a mass-selected beam of negative ions with a fixed-frequency photon beam and energy-analyzing the resultant photodetached electrons. This technique is governed by the energy-conserving relationship, hν = EBE + EKE, where hν, EBE, and EKE are the photon energy, electron binding (transition) energy, and the electron kinetic energy, respectively. Electron kinetic energy is measured using a velocity-map imaging (VMI)[1,2] spectrometer. There, mass-gated anions are crossed with 1064 nm, linearly polarized photons in an electric field, so that resultant photodetached electrons are accelerated along the axis of the ion beam towards a position sensitive detector (75 mm diameter dual microchannel plate detector with a phosphor screen coupled to a CCD camera). The sum of ~50,000 electrons form a 2D image which is then reconstructed into a slice of the 3D distribution via the BASEX[3] method. Photoelectron spectra were calibrated against the well-known photoelectron spectrum of NO^-.[4]

Acetonitrile$^-$ anions were created via Rydberg electron transfer where a beam of state selected potassium Rydberg atoms (K**) are perpendicularly crossed with a pulsed supersonic beam of neutral acetronitrile molecules seeded in helium (~15 psia) using a pulsed (10 Hz) valve (General Valve Series 9). The thermal beam of potassium atoms (~150 °C) were excited to a principle quantum number, n, using a two photon, two color excitation process. Two tunable pulsed (10 Hz) dye lasers, each separately pumped by a Nd:YAG laser, were used. One dye laser was set to the wavelength of the 4p $^2P_{3/2}$ transition (766.7 nm) while the wavelength of the other dye laser was tuned to specific transitions depending on the desired Rydberg level (14d, 467.92 nm). The resulting acetonitrile$^-$ anions were then extracted into a time-of-flight mass spectrometer, mass-selected using a mass gate, and photodetached with first harmonic photons from a Nd:YAG laser and energy analyzed as described above.

VI.3.2. RESULTS

A mass spectrum indicating acetonitrile$^-$ anions (m/z = 41) were made in the RET experiment is presented in Figure VI.24. The acetonitrile anion mass signal was also collected as a function of Rydberg level (Figure VI.25).

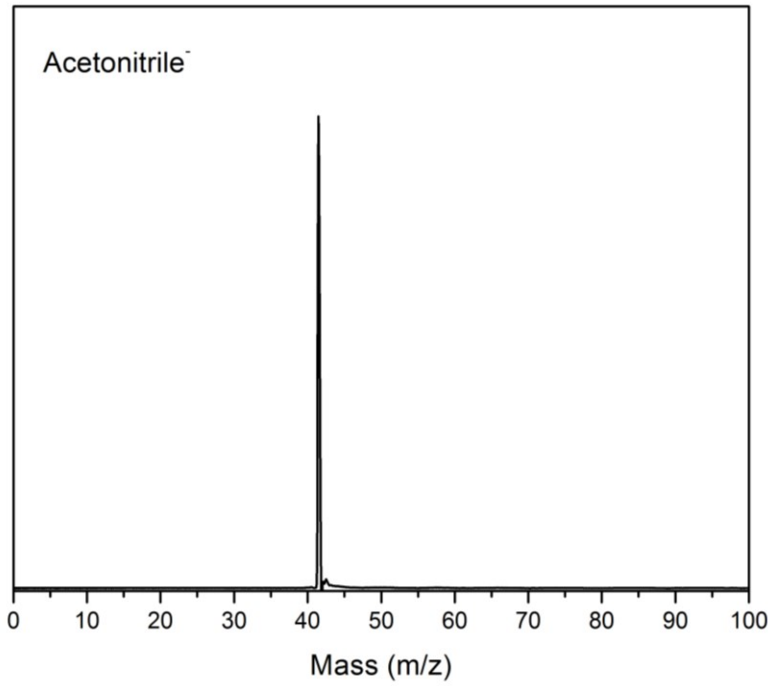

Figure VI.24: Mass spectrum showing acetonitrile$^-$ anion made by Rydberg electron transfer.

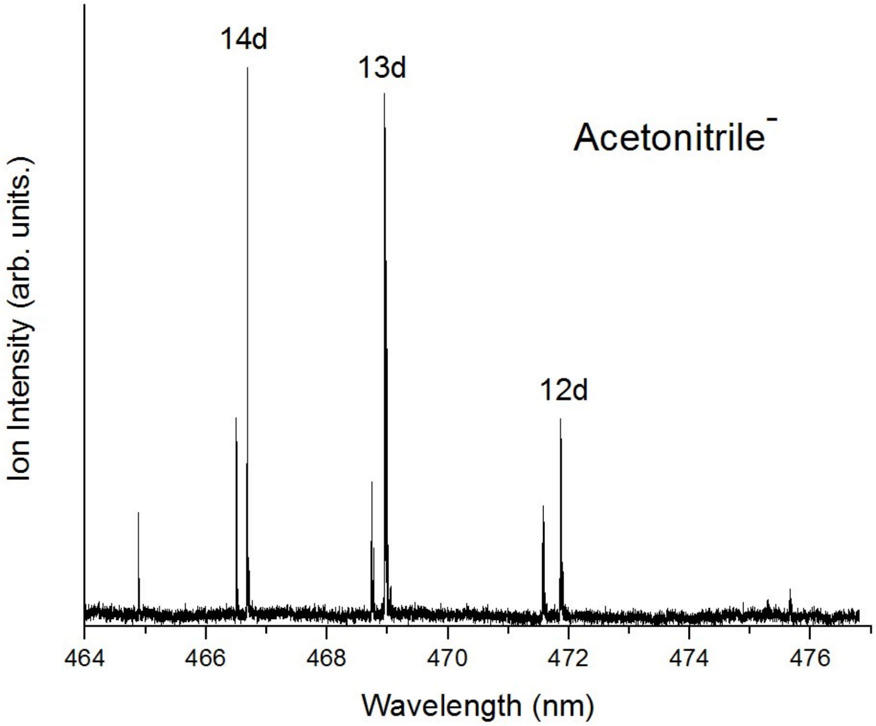

Figure VI.25: Acetonitrile anion signal as a function of Rydberg level.

The anion photoelectron spectrum (PES) of acetonitrile anion measured using 1064 nm (1.165 eV) photons is shown in Figure VI.26. In the PES only one transition is observed which is centered at EBE = 6 meV. This single sharp transition is a spectroscopic signature for a dipole bound anion (Figure VI.26).

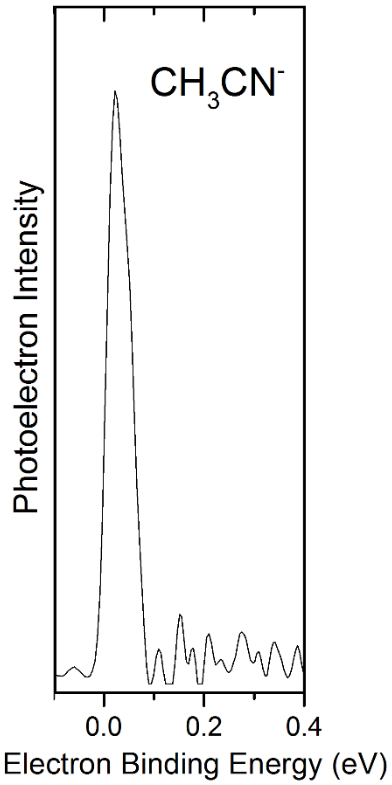

Figure VI.26: Photoelectron spectrum of acetonitrile$^-$ anion $(CH_3CN)^-$ measured with 1.165 eV photons.

REFERENCES

1. A. T. J. B. Eppink and D. H. Parker, Rev. Sci. Instrum. **68**, 3477 (1997).

2. R. Mabbs, E. Surber and A. Sanov, Analyst **128**, 765 (2003).

3. V. Dribinski, A. Ossadtchi, V. A. Mandelshtam and H. Reisler, Rev. Sci. Instrum. **73**, 2634 (2002).

4. J. V. Coe, J. T. Snodgrass, C. B. Freidhoff, K. M. McHugh and K. H. Bowen, J. Chem. Phys. **87**, 4302 (1987).

VI.4. Dimethyl sulfoxide (DMSO) Anion $((CH_3)_2SO)^-$ made by RET

VI.4.1. EXPERIMENTAL

Anion photoelectron spectroscopy is conducted by crossing a mass-selected beam of negative ions with a fixed-frequency photon beam and energy-analyzing the resultant photodetached electrons. This technique is governed by the energy-conserving relationship, hν = EBE + EKE, where hν, EBE, and EKE are the photon energy, electron binding (transition) energy, and the electron kinetic energy, respectively. Electron kinetic energy is measured using a velocity-map imaging (VMI)[1,2] spectrometer. There, mass-gated anions are crossed with 1064 nm, linearly polarized photons in an electric field, so that resultant photodetached electrons are accelerated along the axis of the ion beam towards a position sensitive detector (75 mm diameter dual microchannel plate detector with a phosphor screen coupled to a CCD camera). The sum of ~50,000 electrons form a 2D image which is then reconstructed into a slice of the 3D distribution via the BASEX[3] method. Photoelectron spectra were calibrated against the well-known photoelectron spectrum of NO^-.[4]

Dimethyl sulfoxide$^-$ (DMSO) anions were created via Rydberg electron transfer where a beam of state selected potassium Rydberg atoms (K**) are perpendicularly crossed with a pulsed supersonic beam of neutral DMSO molecules seeded in helium (~5 psia) using a pulsed (10 Hz) valve (General Valve Series 9). The thermal beam of potassium atoms (~150 °C) were excited to a principle quantum number, n, using a two photon, two color excitation process. Two tunable pulsed (10 Hz) dye lasers, each separately pumped by a Nd:YAG laser, were used. One dye laser was set to the wavelength of the 4p $^2P_{3/2}$ transition (766.7 nm) while the wavelength of the other dye laser was tuned to specific transitions depending on the desired Rydberg level (15d, 466.16 nm). The resulting $DMSO^-$ anions were then extracted into a time-of-flight mass spectrometer, mass-selected using a mass gate, and photodetached with first harmonic photons from a Nd:YAG laser and energy analyzed as described above.

VI.4.2. RESULTS

The mass spectrum from the RET experiment is presented in Figure VI.27 and shows the formation of the dipole bound dimethyl sulfoxide$^-$ (DMSO) anion. A small amount of water contaminate was in the system where $DMSO(H_2O)_n^-$ anions and pure $(H_2O)_n^-$ anion clusters are observed. It is also interesting to point out that the dipole bound anion, $(H_2O)_2^-$ is also observed in the mass spectrum.

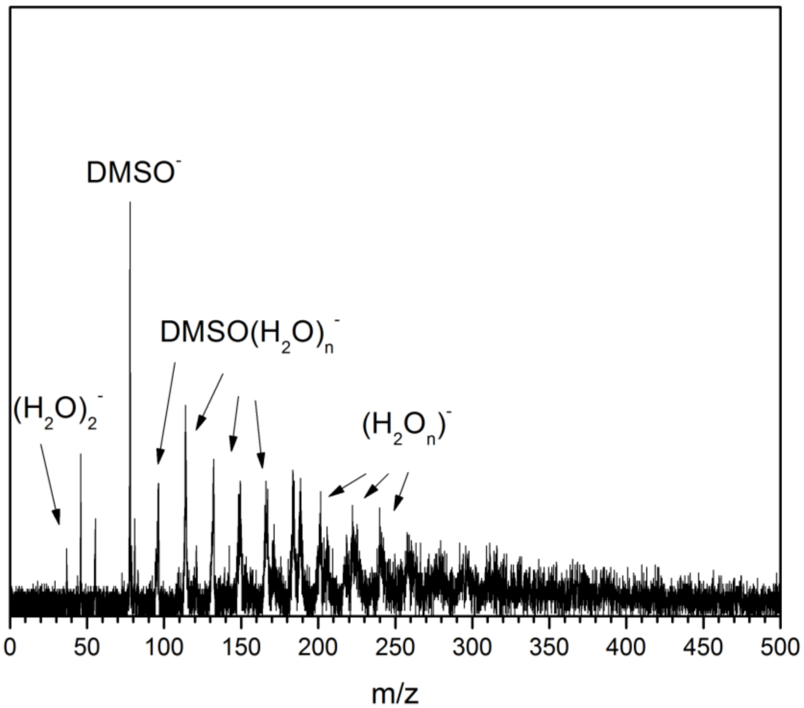

Figure VI.27: Mass spectrum showing dimethyl sulfoxide$^-$ $(DMSO)^-$ anions, with water impurity in the system, made by RET.

The anion photoelectron spectrum (PES) of DMSO anion measured using 1064 nm (1.165 eV) photons is shown in Figure VI.28. In the PES only one transition is observed which is centered at EBE = 6 meV. This single sharp transition is a spectroscopic signature for a dipole bound anion.

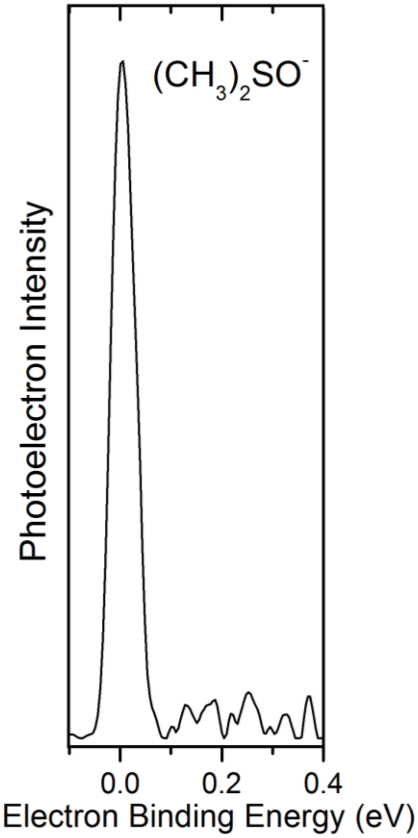

Figure VI.28: Photoelectron spectrum of dimethyl sulfoxide$^-$ anion $(CH_3)_2SO^-$ measured with 1.165 eV photons.

REFERENCES

1. A. T. J. B. Eppink and D. H. Parker, Rev. Sci. Instrum. **68**, 3477 (1997).

2. R. Mabbs, E. Surber and A. Sanov, Analyst **128**, 765 (2003).

3. V. Dribinski, A. Ossadtchi, V. A. Mandelshtam and H. Reisler, Rev. Sci. Instrum. **73**, 2634 (2002).

4. J. V. Coe, J. T. Snodgrass, C. B. Freidhoff, K. M. McHugh and K. H. Bowen, J. Chem. Phys. **87**, 4302 (1987).

VI.5. Ionic Liquid: Methyl-Imidazolium Formate Anion PES

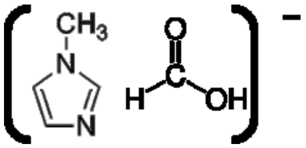

VI.5.1. EXPERIMENTAL

Anion photoelectron spectroscopy is conducted by crossing a mass-selected beam of negative ions with a fixed-frequency photon beam and energy-analyzing the resultant photodetached electrons. Photodetachment transitions occur between the ground state of a mass-selected negative ion and the ground and energetically accessible excited states of its neutral counterpart. This process is governed by the energy-conserving relationship hν = EBE + EKE, where hν is the photon energy, EBE is the electron binding energy, and EKE is the electron kinetic energy. Measuring electron kinetic energies and knowing the photon energy provide electron binding (photodetachment transition) energies. Because these are vertical transitions, their relative intensities are determined by the extent of Franck−Condon overlap between the anion and its corresponding neutral. Our apparatus consists of a laser photoemission/oven anion source, a linear time-of-flight mass spectrometer for mass analysis and mass selection, a momentum decelerator, a magnetic bottle electron energy analyzer, and an Nd:YAG laser. The magnetic bottle has a resolution of ∼50 meV at an EKE of 1 eV. In these experiments, photoelectron spectra (PES) were recorded with 355 nm (3.49 eV) photons. The photoelectron spectra were calibrated against the well-known transitions of atomic Cu^-.[1]

To create 1-methyl imidazolium formate, a few drops of each (clear) liquid, 1-methyl imidazole and formic acid, were added to a small vial and where mixed by shaking a few times by hand. A visible reaction occurred resulting in a viscous clear jelly. The combined product, presumably, methyl imidazolium formate was pipetted onto a silver (Ag) rod (0.25” diameter) and let dry (~5 mins). Laser abaltion/photoemission, using 532 nm (2.33 eV) photons, i.e., 2nd harmonic of a Nd:YAG laser, of the Ag rod with the sample, in the presence of a helium expansion (∼60 psia) through the nozzle orifice (0.79 mm diameter) of a pulsed (10 Hz) valve (General Valve Series 9) in a high vacuum chamber (10^{-6} Torr), produced the 1-methyl imidazolium formate anions.

VI.5.2. RESULTS

The anion mass spectrum from the 1-methyl imidazolium fomate experiment is shown in Figure VI.29. A mass at 128 m/z is indicative of the 1-methyl imidazolium fomate anion, however, the spectrum contains many peaks.

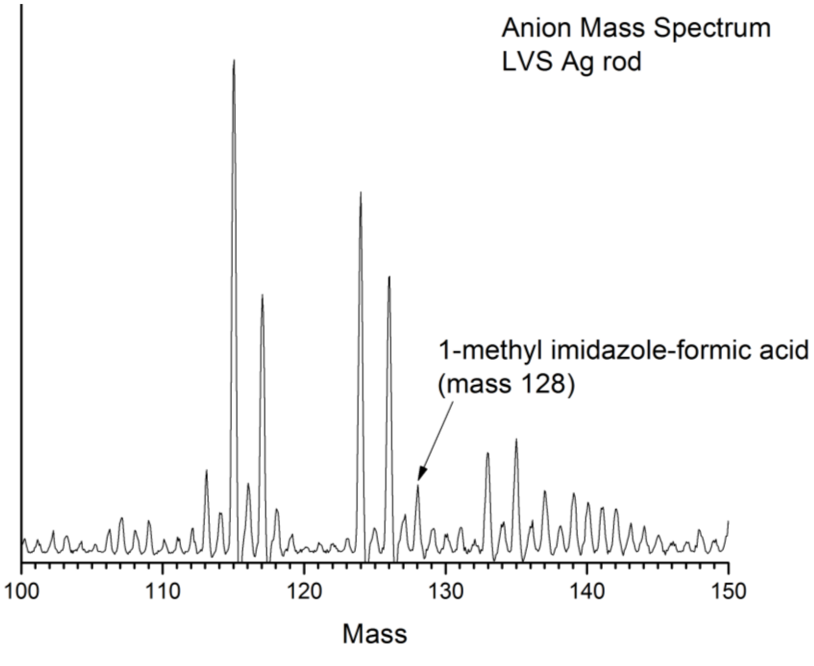

Figure VI.29: Mass spectrum from the methyl imidazolium fomate experiment.

The anion photoelectron spectrum (PES) of the mass at 128, presumably methyl imidaozlium formate anion, measured using 355 nm (3.49 eV) photons is shown in Figure VI.30. The onset of the spectrum begins at ~0.7 eV and the vertical detachment energy (VDE) appears to be 2.2 eV.

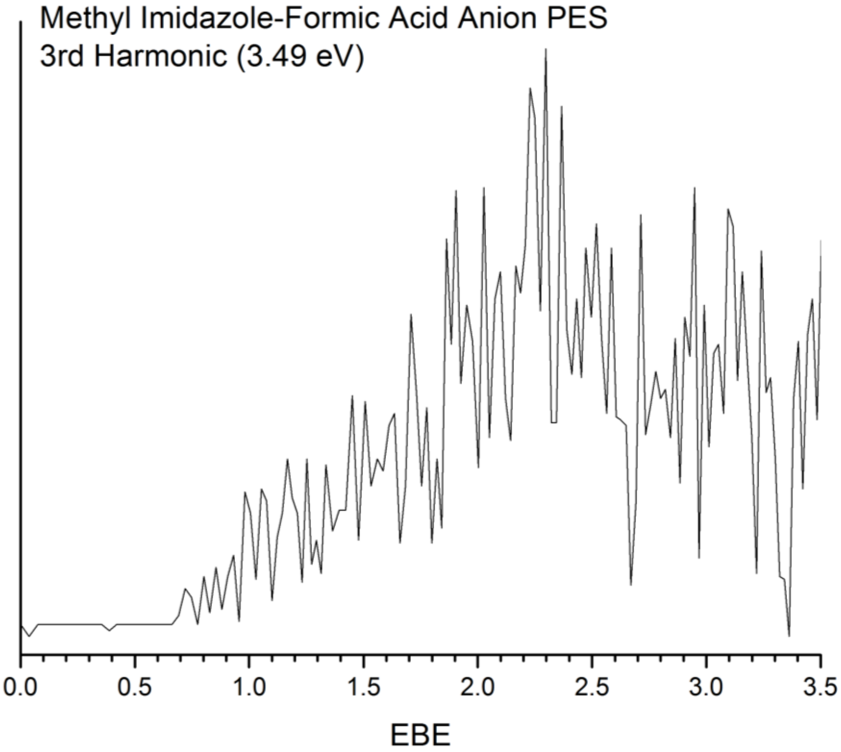

Figure VI.30: Photoelectron spectrum of mass 128, possibly methyl imidzaolium formate.

VI.5.3. DISCUSSION

Geometries and energies of the 1-methylimidazole-formic acid cluster were determined with the unrestricted B3LYP functional with a 6-311+G(d,p) basis set. Optimized neutral and anion structures are shown in Figure VI.31. The anion structure shows proton transfer, however, a zero-point corrected electron affinity was determined to be -0.11 eV.

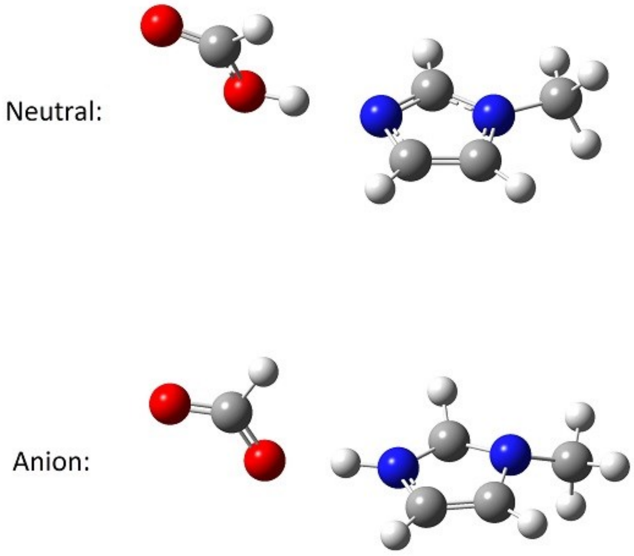

Figure VI.31: Neutral and anion geometries of the 1-methyl imidazole formic acid anion complex at the B3LYP/ 6-311+G(d,p) level of theory.

ALLYSON M. BUYTENDYK

abuytendyk@gmail.com • 330-347-6071
3811 Canterbury Rd. Apt 205, Baltimore, MD 21218

EXPERIMENTAL PHYSICAL CHEMIST

Scientist with experience in vacuum instrumentation design, TOF mass spectrometry and photoelectron spectroscopy. Interdisciplinary research background studying the structure as well as electronic, magnetic and optical properties of molecules & clusters in chemistry, biology, and condense matter physics.

Core competencies include: Gas phase ions • Instrument building • High vacuum systems

---

EDUCATION

Doctor of Philosophy Chemistry – Johns Hopkins University (Baltimore, MD) September 2015

- Thesis title: *Discovering the Electronic Properties of Metal Hydrides, Metal Oxides and Organic Molecular Anions Using Photoelectron Spectroscopy*

Master of Arts Chemistry – Johns Hopkins University (Baltimore, MD) April 2012

Bachelor of Arts Chemistry, Mathematics – The College of Wooster (Wooster, OH) May 2009

RESEARCH EXPERIENCE

Johns Hopkins University– Department of Chemistry, Baltimore, MD August 2009 – September 2015

Graduate Research Assistant (Adviser: Prof. Kit. H. Bowen)

- Developed fundamental knowledge of ion beams and high-vacuum systems in a team environment by designing & building a time-of-flight (TOF) mass spectrometer for an existing instrument
- Independently designed and fabricated an alkali metal oven source to perform Rydberg electron transfer experiments demonstrating complex analytical problem solving and research skills
- Conducted research on size-selected negative ion molecules in isolation by evaluating their electronic and vibrational properties using gas phase mass spectrometry and photoelectron spectroscopy
  - Studied the energetic properties of metal hydride and oxides, hydrogen bonding interactions between acid-base pairs, and electron-induced proton transfer between organic molecules

Chemical/Analytical Skills: Mass spectrometry (TOF, quadrupole, magnetic sector, Wien velocity filter), Photoelectron spectroscopy (magnetic bottle, velocity map imaging (VMI), hemispherical analyzer), Vacuum systems & instrumentation design (ion optics, ion and electron sources)

Other Specialized Skills: Pulsed lasers (Nd:YAG, Excimer, dye) & Continuous lasers (Ar-ion); Handling gases; Air sensitive & flammable material; Designing/building electronic circuits; Metal machining

The College of Wooster – Department of Chemistry, Mathematics Wooster, OH June 2006 – June 2009

Undergraduate Research Assistant (Advisers: Prof. Judith C. Amburgey-Peters, Prof. R. Drew Pasteur)

- Developed fundamental knowledge and understanding of organic synthesis& biomolecules
  - Synthesized cyclohexylphospho-l-serine, an analog of the phospholipid phosphatidylserine
- Independently designed an experiment to measure the binding affinity between the phospholipid analog & calcium and developed a mathematical model to determine the reaction rate

Chemical/Analytical Skills: Isothermal titration calorimetry (ITC), NMR (^{1}H, ^{31}P), high pressure reactions, HPLC, GC-MS, Atomic Absorbance (AA), IR, UV-Vis spectroscopy

SOFTWARE SKILLS

Microsoft Office ● ChemDraw ● LabVIEW ● Mathematica ● MATLAB ● SIMION ● Origin

MENTORING EXPERIENCE

Graduate Student Mentor–of high school senior, in Bowen laboratory August 2010 – May 2011

- Coached student to develop competencies in planning, organizing and executing a science fair project and challenged her to think critically and establish strong experimental research skills

TEACHING EXPERIENCE

Johns Hopkins University August 2009 - May 2011

Introductory Chemistry Teaching Assistant & *Physical Chemistry Laboratory Assistant*

- Explained core concepts to 50 undergraduate students and motivated them to practice good study habits
- Guided 25 students to develop their laboratory skills to their full potential while facilitating safe practices

The College of Wooster August 2005 - May 2008

First-Year Seminar in Critical Inquiry Teaching Assistant, *IntroductoryChemistry Laboratory Assistant*

- Created an inclusive environment for 15 undergraduates focusing on critical thinking discussions and career development ideas while embracing the values of diversity
- Supervised 30 students each semester in learning chemistry laboratory techniques and evaluated their pre-laboratory procedures & written reports

CONFERENCE POSTERS/PRESENTATIONS

Presentation

- XXIII International Materials Research Congress, Cancun, Mexico August 2014: "*Photoelectron Spectroscopy of Molecular Anions*"

Posters

- XVII Symposium on Atomic, Cluster & Surface Physics (SASP), University of Obergurgl, Austria January 2010: "*Electron-Induced Proton Transfer in Acid-Base Reactions: Anion Photoelectron Spectroscopic Studies*"
- 2009 National American Society of Biochemistry and Molecular Biology (ASBMB) Meeting, New Orleans, LA, April 2009: "*Determining the Binding Affinity Between Calcium and the Phospholipid Analog, CyclohexylPhospho-L-Serine*"
- 233rdNational American Chemical Society (ACS) Meeting, Chicago, IL March 2007: "*Synthesis of cyclohexylcarbobenzyloxy-L-serine benzyl ester phosphodiester: A Precursor to the Phospholipid Analog Cyclohexylphosphoserine*"

PUBLICATIONS

14. **Buytendyk, A.**; Chavez, T.; Graham, J.; Pederson, M.; Bowen, K.; Toscano, J.; “The Singlet-Triplet Splittings of Benzoylnitrene, Acetylnitrene, and Trifluoroacetylnitrene.” (in preparation).

13. **Buytendyk, A.**; Graham, J.; Bowen, K.; Wu, C.-H.; Wu, J. I. C. “Photoelectron Spectroscopic and Computational Investigation of the Intramolecular Hydrogen Bonding in Salicylate$^-$ Anion and the Intermolecular Hydrogen Bonding in the Salicylate–Salicylic Acid$^-$ Anionic Complex” (in preparation).

12. Graham, J.; **Buytendyk, A.**; Zhang, X; Kim, S.; Bowen, K. “Carbon Dioxide is Tightly Bound in the $[Co(Pyridine)(CO_2)]^-$ Anionic Complex” (submitted, *J. Chem. Phys.*).

11. **Buytendyk, A.**; Graham, J.; Collins, K.; Bowen, K.; Wu, C.-H.; Wu, J. I. C. “The Hydrogen Bond Strength of the Phenol-Phenolate Anionic Complex: A Computational and Photoelectron Spectroscopic Study” (in press, *Phys. Chem. Chem. Phys.*).

10. Graham, J.; **Buytendyk, A.**; Wang, Yi; Kim, S.; Bowen, K. CO_2 Binding in the $(Quinoline\text{-}CO_2)^-$ Anionic Complex” (in press, *J. Chem. Phys.*).

9. Buendia, F.; Beltran, M.; Zhang, X.; Liu, G.; **Buytendyk, A. M.**; Bowen, K.B. “Ab initio and Anion Photoelectron Study of Au_nRh_m (n=1−7,m=1−2) Clusters” (in press *Physical Chemistry Chemical Physics*).

8. **Buytendyk, A. M.**; Wang. Y.; Graham, J. D.; Kandalam, A. K.; Kiran, B.; Bowen, K. H. “Photoelectron Spectrum of a Polycylcic Aromatic Nitrogen Heterocyclic Anion: Quinoline$^-$” (in press, *Molecular Physics*).

7. **Buytendyk, A. M.**; Graham, J. D.; Gould, J.; Pederson, M. R.; Bowen, K. H. “Parent Anions of Iron, Manganese, and Nickel Tetraphenyl Porphyrins: Photoelectron Spectroscopy and Computations” *J. Phys. Chem. A*, **2015**, *119*, 8643–8646.

6. Graham, J.D.; **Buytendyk, A. M.** ; Zhang, X.; Collins, E. L.; Kiran, B.; Gantefoer, G.; Eichhorn, B. W.; Gutsev, G. L.; Behera, S.; Jena, P.; Bowen, K. H. “The Alanate Anion, AlH_4^-: Photoelectron Spectrum and Computations” *J. Phys. Chem. A*, **2014**, *118*, 8158–8162.

5. Buonaugurio, A.; Graham, J.; **Buytendyk, A.**; Bowen, K. H.; Ryder, M.; Keolopile, Z.; Haranczyk, M.; Gutowski, M. “Communication: Remarkable Electrophilicity of the Oxalic Acid Monomer: An Anion Photoelectron Spectroscopy and Theoretical Study” *J. Chem. Phys.*, **2014**, *140*, 221103-5.

4. **Buytendyk, A.**; Graham, J.; Wang, H.; Zhang, X.; Collins, E.; Ko, Y. J.; Gantefoer, G.; Eichhorn, B.; Regmi, A.; Kiran, B.; Bowen, K. H. “Photoelectron Spectra of the MgH^- and MgD^- Anions” *Int. J. of Mass Spectrom.*, **2014**, *140*, 365-366.

3. Graham, J.; **Buytendyk, A.**; Wang, D.; Bowen, K. H.; Collins, K. D. “Strong, Low Barrier Hydrogen Bonds may be Available to Enzymes” *Biochemistry*, **2014**, *53*, 344-349.

2. Li, X.; Zheng, W.; Buonaugurio, A.; **Buytendyk, A.**; Bowen, K.H.; Balasubramanian, K. “Photoelectron Spectroscopy of the Molecular Anions, ZrO^-, HfO^-, $HfHO^-$, and HfO_2H^-”, *J. Chem. Phys.*, **2012**, 136, 154306-5.

1. Wang, D.; Graham, J.D.; **Buytendyk, A.M.**; Bowen, K.H. “Photoelectron Spectroscopy of the Molecular Anions, Li_3O^- and Na_3O^-” *J. Chem. Phys.*, **2011**, *135*, 164308-4.